2015-04-30

Spin-Phonon Coupling and Magnetic Heat Transport in Low-Dimensional Quantum Antiferromagnets

Narayan Prasai
University of Miami, narayanprasai@gmail.com

UNIVERSITY OF MIAMI

SPIN-PHONON COUPLING AND MAGNETIC HEAT TRANSPORT IN LOW-DIMENSIONAL QUANTUM ANTIFERROMAGNETS

By

Narayan Prasai

A DISSERTATION

Submitted to the Faculty
of the University of Miami
in partial fulfillment of the requirements for
the degree of Doctor of Philosophy

Coral Gables, Florida

May 2015

UNIVERSITY OF MIAMI

A dissertation submitted in partial fulfillment of
the requirements for the degree of
Doctor of Philosophy

SPIN-PHONON COUPLING AND MAGNETIC HEAT TRANSPORT IN LOW-DIMENSIONAL QUANTUM ANTIFERROMAGNETS

Narayan Prasai

Approved:

_____ Joshua L. Cohn, Ph.D. Professor of Physics	_____ Fulin Zuo, Ph.D. Professor of Physics
_____ Sunxiang Huang, Ph.D. Asst. Professor of Physics	_____ M. Brian Blake, Ph.D. Dean of the Graduate School
_____ Francisco M. Raymo, Ph.D. Professor of Chemistry	

PRASAI, NARAYAN (Ph.D., Physics)
Spin-Phonon Coupling and Magnetic Heat Transport (May 2015)
in Low-Dimensional Quantum Antiferromagnets

Abstract of a dissertation at the University of Miami.
Dissertation supervised by Professor Joshua L. Cohn
No. of pages in text. (118)

Experimental measurements of heat conduction in the low-dimensional antiferromagnetic compounds $CuSb_2O_6$ and $BiCu_2PO_6$ are presented for the range $0.5K \leq T \leq 390K$. Both compounds have magnetic exchange (J) and Debye (θ_D) energies that are comparable. This distinguishes the present work from prior studies which have focused on the regime $J \gg \theta_D$. Individual crystals were characterized by x-ray diffraction to identify bicrystallinity, twinning and other defects. Thermal conductivity $\kappa(T)$ for both the spin-½ chain compound ($CuSb_2O_6$) and the spin-½ two-leg ladder compound ($BiCu_2PO_6$) imply strong spin-phonon resonant scattering. Model fitting to the lattice component of the heat conductivity was employed to extract a characteristic energy scale for the magnetic excitations. Anisotropy was evident in κ of both compounds, possibly associated with heat conduction by the spin system. The magnetic mean free path inferred from the data are also presented and compared with those of other low-D spin systems.

DEDICATION

To my Parents Phanindra Raj and Lila Devi

ACKNOWLEDGEMENT

At this moment, while achieving this highest degree of formal education, I would like to look back and say--THANK YOU --to all the supporting hands which helped me to arrive at this point.

I feel very fortunate to have Joshua L. Cohn as my advisor, and I thank him from the bottom of my heart. When I recall what I have learned from him, it is not only limited to scientific knowledge related to research projects I am involved, but more importantly, how a scientist does tackle a research problem. Various experimental skills, I have developed while working in his lab (whether it be dealing with less than mm sized crystal and 0.001" thermocouples or acquiring cryogenic techniques) were possible because of his broad experience and by his passionate teaching. He is a superb mentor with goal and effort both directed to prepare his mentee as an independent researcher.

I would like to thank my dissertation committee members, Fulin Zuo, Sunxiang Huang and Francisco M. Raymo for various comments and suggestions, which definitely helped to improve this dissertation.

I would like to thank all the professors from the department of physics, University of Miami who helped me either directly or indirectly during my graduate study. I would like to remember and thank, late Joseph Ashkenazi who invited me to this department as a graduate student.

It was great opportunity to collaborate with researchers from other universities, I thank them all for fruitful collaborations. Especially, I would like to thank John J. Neumeier and his research group from Montana State University for providing single crystals studied in this dissertation.

I acknowledge the help in various ways from Judy Mallery (Department manager), Anella Sebro (Secretary), Marco Monty (Network Administrator) and Manuel Collazo (Machine shop technician) during my graduate student life and would like to thank them all.

I thank the current and former members of the Cohn research group--Alwyn Rebello, Saeed Moshfeghyeganeh, Alexandra Cote, and Artem Akopyan--for their companionship and discussions.

I would like to thank my friend Youaraj Upreti for his help and companionship throughout my graduate student life at UM. Purushottam Bhandari and his family were a great help in my early years at Miami for providing a home away from home, and I want to thank them a lot. Similarly, the help and companionship of Rudra Aryal, Krishna Prasai, and the entire Miami-Nepalese community are sincerely acknowledged.

Finally, I thank my family members and relatives for their love and support, especially my parents for their unconditional love and continuous efforts to secure my education, and my uncle, Bal Krishna, (my school science teacher) for introducing me to science. My siblings, sisters Tika and Yamuna, brother Rajib, and sister-in-law Bismita are always amazing friends to share love and encouragement with--thank you for everything. Thanks a lot to my in-laws Bharati, Yogendra and Shraddha for their love and support. My wife Shreya has been a great source of love and support in these daunting last five years of my graduate life. Accomplishing this would have been very difficult without her and my daughter, Shreyanshi, who is my reason to smile even in difficult times. I cannot thank them enough.

PREFACE

The history of one-dimensional magnetism goes back to 1925 with the one dimensional Ising model by Ernst Ising. Another important step in this direction was by the development of "Bethe Anstaz" by Hans Bethe in 1931 to find the exact quantum mechanical ground state of the one-dimensional antiferromagnetic Heisenberg model [1]. Only after 1970, experimentalists got into this field with the realization of existence of restricted dimensional magnet in the real world. These magnets exist as a bulk crystal but magnetic exchange interaction is much stronger in one particular direction as compared to rest of the other directions. In one dimension, Fermi liquid breaks down and is represented by new state called Luttinger liquid where effects of interaction are at its maximum. In contrast to single particle excitation of fermions with spins in higher dimension, only separate collective excitations carrying charge and spin exist in one dimension resulting in separation of charge and spin [2]. Thus, unique opportunity provided by these materials to study ground and excited states of quantum models, probable new phases of matter and interplay of quantum fluctuations and thermal fluctuations helped to cultivate one-dimensional magnetism as a new field in solid state physics [1].

The revelation of *spinon* nature of excitation spectrum of spin-½ antiferromagnetic (AF) chain by Faddeev and Takhtajan in their seminal paper "What is the spin of a spin wave?"[3], and the conjecture of Haldane [4] about the gapped spectrum of integer AF spin chain in contrast to gapless excitation spectrum of half integer AF spin chain boosted the interest in this field. Another lift to this field came from the discovery of high-T_C superconductivity in cuprates, and its association to the strong magnetic fluctuation which

is quite probable in low dimensional materials [1]. Also, in the last couple of years, fabrication of various materials which are good realization of quasi-two or one-dimensional quantum magnets in the form of spin chain, spin ladder and planar spin structure have been successful. Therefore, one dimensional model systems are quite modest for theoretical predictions and available physically to validate these predictions experimentally, making them a playground for both theorist and experimentalist.

The Heisenberg model is extensively known for describing properties of low-dimensional quantum magnets, and its agreement with experimental results. The one-dimensional antiferromagnetic Heisenberg chain, a special case of the Heisenberg model, and coupling of such chains giving a spin ladder structure, which can be considered "in between" one and two dimensions, have been studied in this thesis (see Chapter 1 for background on these systems). In the last decades, various thermodynamic properties such as specific heat and magnetic susceptibility, and also ground state and excitation spectrum have been studied and good agreement has been found between theory and experiments. Much less is known about dynamics of magnetic excitations. Thermal conductivity as a function of temperature and magnetic field provides the information about microscopic understanding of how energy is transported in such systems and coupling to the lattice.

Experimental evidence of heat transport by magnetic excitations was known long before on ferromagnetic Yttrium-Iron-Garnet (YIG) [5] below ordering temperature and on one dimensional AFM compound $KCuF_3$ above ordering temperature [6]. Much of the interest in thermal conductivity came only after theoretical predictions of dissipationless heat transport by 1D-AFM Heisenberg chain [7], [8], and experimental findings of huge magnetic heat transport in spin ladder compound [9]–[11]. To date, most thermal

conductivity investigations have focused on quasi-one-dimensional (Q1D) spin-½ chain systems with exchange energies much greater than the Debye temperature ($J \gg \theta_D$) [5], [12], where spin heat conduction is often distinguishable from that of the lattice by their different temperature scales. The situation is potentially more complex when spin and phonon energy scales are comparable since interactions between the two subsystems become more significant and can lead to dimerization of magnetic ions (spin-Peierls transition). At least one system having $J \sim \theta_D$ for which a spin thermal conductivity has been inferred from κ measurements [13], has a spin mean free path (l_{mag}) comparable to that in large J systems, suggesting similar relaxation characteristics.

Therefore, this thesis presents thermal conductivity (κ) of two compounds both having similar or smaller magnetic exchange than Debye energy ($J \leq \theta_D$), $CuSb_2O_6$, a Heisenberg Antiferromagnetic (HAF) spin-½ chain compound, and $BiCu_2PO_6$, a HAF spin-½ two-leg ladder compound. Our results are interesting and provide further insight into this low J regime. First, strong spin-phonon coupling is imminent in this regime as evident by strong damping of thermal conductivity. Second, inferred magnetic contribution to heat transport primarily along the chain and ladder direction is significant given the low value of J. Third, inferred magnetic mean free path (l_{mag}) from magnetic thermal conductivity (κ_{mag}) is similar in temperature dependence and magnitude to other low-D spin-½ systems [13] and implies the universal spin-mediated energy transport in spin-½ systems when suitably scaled by J.

The outline of this thesis is as described below. Chapter 1 provides contextual information on low-dimensional magnetism for readers new to this field. Chapter 2 presents the background on thermal conductivity of insulating solids such that any reader

will gain insight into phenomenological description of thermal conductivity and various scattering mechanisms governing thermal conductivity in such solids. Chapter 3 is a detailed description of the experimental set up, techniques and calibration procedures extensively used in this work. Chapter 4 presents thermal conductivity of HAF spin-½ chain compound $CuSb_2O_6$ in all three principal directions and along spin chain direction [110], and compares with its non-magnetic analog $ZnSb_2O_6$ along [100] direction. Detailed characterization of crystals by x-ray diffraction, model fitting to lattice thermal conductivity to differentiate magnetic component of heat transport, and inferred magnetic mean free path have been discussed. Chapter 5 is dedicated to the spin-½ two-leg ladder compound $BiCu_2PO_6$. Thermal conductivity along all three crystallographic directions have been offered. Anisotropy in κ, its magnetic field dependence, model fitting to lattice thermal conductivity, and inferred magnetic component of thermal conductivity as well as magnetic mean free path have been presented.

TABLE OF CONTENTS

LIST OF FIGURES

LIST OF TABLES

CHAPTER I

BACKGROUND ON LOW-DIMENSIONAL MAGNETISM

This chapter will review the basic concepts required to understand the magnetism in low dimensional magnetic systems. The fundamental concepts of exchange and spin-orbit coupling are the most important concepts in modern physics. The core of research in magnetism is the interplay among the exchange, the spin-orbit and the Zeeman interaction [14]. The exchange interaction is the largest magnetic interaction, and it accounts for the alignments of the spin system (parallel or antiparallel) as well as spontaneous magnetization. The spin-orbit interaction is responsible for the coupling between electron's orbital angular momentum and spin angular momentum, thus the origin of magnetic anisotropy. The Zeeman interaction of magnetic moments with an external magnetic field is responsible for the alignment of moments along field direction. It is important to note that an external magnetic field acts on both spin and charge, whereas exchange interaction acts only on spin. I will start with spinor, describe magnetic exchange interaction applicable to systems under study and present various forms of Heisenberg Hamiltonian essential to describe the magnetic structure of compounds studied in this thesis.

1.1 SPIN AND SPINOR

We know that an electron possesses an intrinsic angular moment called spin. For a spin-½ particle there are just two eigenstates called spin up $|\frac{1}{2}, \frac{1}{2}\rangle$ or $|\uparrow\rangle$ and spin down $|\frac{1}{2}, \frac{-1}{2}\rangle$

or $|\downarrow\rangle$. And, using these as a basis, the quantum spin state of spin-½ particle can be described by a two-element column matrix called *spinor*, $\binom{1}{0}$ for up state and $\binom{0}{1}$ for down state. When we use these spinors to describe quantum states, the quantum mechanical operators become 2×2-matrices which can be expressed in terms of *Pauli spin matrices* [15], [16].

$$\sigma_x = \begin{pmatrix} 0 & 1 \\ 1 & 0 \end{pmatrix}, \qquad \sigma_y = \begin{pmatrix} 0 & -i \\ i & 0 \end{pmatrix}, \qquad \sigma_z = \begin{pmatrix} 1 & 0 \\ 0 & -1 \end{pmatrix} \tag{1.1}$$

The spin angular momentum operator is,

$$\boldsymbol{S}_\alpha = \frac{1}{2}\hbar\boldsymbol{\sigma}_\alpha, \tag{1.2}$$

where $\alpha = (x, y, z)$. From here on, we consider associated angular momentum in unit of $\hbar$. Among the three Pauli matrices, only σ_z is diagonal with eigenvalues $\pm\frac{1}{2}$ and the corresponding eigenstates are,

$$|\uparrow\rangle = \binom{1}{0}, \qquad |\downarrow\rangle = \binom{0}{1} \tag{1.3}$$

for the spin pointing parallel and antiparallel to *z*-axis respectively. Now we can state the rules for spin operators $\boldsymbol{S}_\alpha$ acting on spin states $|\uparrow\rangle$ and $|\downarrow\rangle$ as,

$$S_x|\uparrow\rangle = \frac{1}{2}\left|\downarrow\right\rangle,\ S_x|\downarrow\rangle = \frac{1}{2}\left|\uparrow\right\rangle, \tag{1.4}$$

$$S_y|\uparrow\rangle = \frac{i}{2}\left|\downarrow\right\rangle, S_y|\downarrow\rangle = \frac{-i}{2}\left|\uparrow\right\rangle, \tag{1.5}$$

and

$$S_z|\uparrow\rangle = \frac{1}{2}\left|\uparrow\right\rangle, S_z|\downarrow\rangle = \frac{-1}{2}\left|\downarrow\right\rangle. \tag{1.6}$$

Similarly, eigenstates of the spin pointing parallel and antiparallel to *x*- and *y*- axis are,

$$|\uparrow_x\rangle = \frac{1}{\sqrt{2}}\binom{1}{1}, \qquad |\downarrow_x\rangle = \frac{1}{\sqrt{2}}\begin{pmatrix} 1 \\ -1 \end{pmatrix} \tag{1.7}$$

$$|\uparrow_y\rangle = \frac{1}{\sqrt{2}}\begin{pmatrix}1\\ i\end{pmatrix}, \quad |\downarrow_y\rangle = \frac{1}{\sqrt{2}}\begin{pmatrix}1\\ -i\end{pmatrix}. \tag{1.8}$$

These spinors form a complete basis to describe spin-½ particles in a Hilbert space. Thus, a linear combination of these two states can represent all possible states of the spin.

1.2 MAGNETIC INTERACTION

1.2.1 DIPOLE-DIPOLE INTERACTION

Each spin at any position r can be considered as the dipole moment with the value $g\mu_B \boldsymbol{S}_r$, where g is gyromagnetic constant and μ_B is Bohr magnetron. Then, there exists a totally magnetic interaction between spins which is called magnetic dipole-dipole interaction. The value of magnetic dipole-dipole interaction for the nearest-neighbor (NN) spins in a magnetic crystal is of the order of $g^2\mu_B^2/a \approx 10^{-1}K$ for transition metal [17], where a is the lattice constant. Many systems order at much higher temperature and the dipole-dipole interaction is too weak to explain the ordering of most magnetic materials. However, magnetic dipole-dipole interaction is important for many characteristics of spin systems and also for ordering at mili-Kelvin temperature.

1.2.2 EXCHANGE INTERACTION

To account for magnetic ordering at much higher temperature we need to introduce another spin-spin interaction with higher energy scale than dipole-dipole interaction which is called *exchange interaction*.

1.2.2.1 DIRECT EXCHANGE INTERACTION

Direct exchange arises from the direct interaction of electrons within an atom or neighboring atoms. Such direct exchange is mainly because of direct overlap of wave

functions. In the subsequent paragraphs, we derive the Hamiltonian which deals with the direct exchange among electrons, and subsequently spins.

We consider a complete one-electron wave function which consists of both a spatial part and a spin part. The direction of spin is relative to z-axis of co-ordinate system of choice. We have,

$$\psi(\boldsymbol{a}) = \psi(\boldsymbol{r}, \boldsymbol{s}) = R_{n,l}\,(r) Y_{l,m}(\theta, \varphi)\chi(s_z) \tag{1.9}$$

where, n, l, m are principal, azimuthal and magnetic quantum numbers. First, two terms in the right hand side of Eq. (1.9) describe the spatial part of wave function while $\chi(s_z)$ describes the spin dependence, which is either $\alpha = |\uparrow\rangle$ or $\beta = |\downarrow\rangle$.

For a two-electron system the total wave function is the product of individual electron wave functions,

$$\Psi(\boldsymbol{a}, \boldsymbol{b}) = \Psi(\boldsymbol{r_1} s_1; \boldsymbol{r_2 s_2}) = \psi_1(\boldsymbol{a})\psi_2(\boldsymbol{b}). \tag{1.10}$$

Since, two electrons are indistinguishable,

$$\Psi(\boldsymbol{a}, \boldsymbol{b}) = \psi_2(\boldsymbol{a})\psi_1(\boldsymbol{b}). \tag{1.11}$$

Linear combination of two wave functions must give a solution of two-electron Hamiltonian,

$$\Psi(\boldsymbol{a}, \boldsymbol{b}) = \frac{1}{\sqrt{2}}[\psi_1(\boldsymbol{a})\psi_2(\boldsymbol{b}) \pm \psi_2(\boldsymbol{a})\psi_1(\boldsymbol{b})], \tag{1.12}$$

where the plus and minus sign represents a *symmetrical* and *antisymmetrical* total wave function corresponding to bosons (with integer spins) and fermions (half-integer spins) respectively. Since electrons are fermions, the total wave function must be antisymmetric. There are two possibilities, either the spatial part is symmetric and the spin part is antisymmetric or vice versa. The antisymmetric two-electron spin function represents a *singlet state* with total spin quantum numbers $S = 0,\ M_S = 0$ and symmetric two-electron

spin function represents a *triplet state* with total spin quantum numbers $S = 1$, $M_S = -1, 0, 1$ [14]. The total wave function for these two states can be written as,

$$\Psi_S(\boldsymbol{a}, \boldsymbol{b}) = \frac{1}{\sqrt{2}}[\psi_1(\boldsymbol{r_1})\psi_2(\boldsymbol{r_2}) + \psi_2(\boldsymbol{r_1})\psi_1(\boldsymbol{r_2})]\chi_S(\boldsymbol{s_1}, \boldsymbol{s_2}), \tag{1.13}$$

$$\Psi_T(\boldsymbol{a}, \boldsymbol{b}) = \frac{1}{\sqrt{2}}[\psi_1(\boldsymbol{r_1})\psi_2(\boldsymbol{r_2}) - \psi_2(\boldsymbol{r_1})\psi_1(\boldsymbol{r_2})]\chi_T(\boldsymbol{s_1}, \boldsymbol{s_2}), \tag{1.14}$$

where $$\chi_S(\boldsymbol{s_1}, \boldsymbol{s_2}) = \frac{1}{\sqrt{2}}(\alpha\beta - \beta\alpha) \tag{1.15}$$

and $$\chi_T(\boldsymbol{s_1}, \boldsymbol{s_2}) = \begin{cases} \alpha\alpha \\ \frac{1}{\sqrt{2}}(\alpha\beta - \beta\alpha). \\ \beta\beta \end{cases} \tag{1.16}$$

As we know,

$$(s_1 \cdot s_2) = \frac{1}{2}S(S+1) - \frac{1}{2}s_1(s_1+1) - \frac{1}{2}s_2(s_2+1). \tag{1.17}$$

Only considering the normalized spin part and for $s_1 = s_2 = \frac{1}{2}$,

$$(s_1 \cdot s_2) = \frac{1}{2}S(S+1) - \frac{3}{4} = \begin{cases} -\frac{3}{4}, for\ S = 0\ \ (singlet) \\ +\frac{1}{4}, for\ S = 1\ (triplet). \end{cases} \tag{1.18}$$

Therefore, the effective Hamiltonian in the spin subspace for two electrons with spin-½ can be written as,

$$H_{eff} = \frac{1}{4}(E_S + E_T) - (E_S - E_T)S_1 \cdot S_2, \tag{1.19}$$

where the first term in the right-hand side is spin independent, while the second term is spin dependent. Thus, the first term can be neglected while extending spin interactions to more than two spins.

Therefore, the exchange constant J_{12} can be defined as,

$$J_{12} = \frac{E_T - E_S}{2}. \tag{1.20}$$

We can see that for $J_{12} < 0$, singlet has higher energy than triplet, so triplet is ground state for ferromagnets where spins are aligned parallelly. For $J_{12} > 0$, triplet has higher energy than singlet, thus making singlet a ground state for antiferromagnets, where spins are aligned antiparallelly. Also, we can infer that exchange integral falls off rapidly as the distance between interacting spins increases. Therefore, magnetism of solids is mainly based on short–range interaction.

The Hamiltonian (1.19) is called exchange Hamiltonian for the two-electron system. Heisenberg and Dirac in 1926 showed independently (later developed by van Vleck) that similar effective Hamiltonians for any number of electrons in a subspace with fixed orbital components (spin independent) can be chosen in all possible ways. This is called *Heisenberg Hamiltonians* for interacting spins,

$$H = \sum_{i,j} J_{ij}\, \boldsymbol{s_i} \cdot \boldsymbol{s_j}, \tag{1.21}$$

where the factor 2 is included in summation.

1.2.2.2 INDIRECT EXCHANGE

Indirect exchange arises when a wave function of one magnetic atom overlaps with that of another magnetic atom via wave functions of intermediate atoms. Most prominent indirect exchanges are *superexchange*, *double exchange*, and *RKKY exchange*. We will only discuss the first kind, which is most relevant to this work.

The name *superexchange* comes from the fact that it extends the short-range magnetic interaction to a longer range. The idea of superexchange explains why some ionic solids (which are insulators) have antiferromagnetic ground states, eg. MnO, MnF_2 . The

idea that magnetic moments can communicate via intermediate non-magnetic atoms was first proposed by Kramers in 1934 [18] and developed by Anderson in 1950 [19].

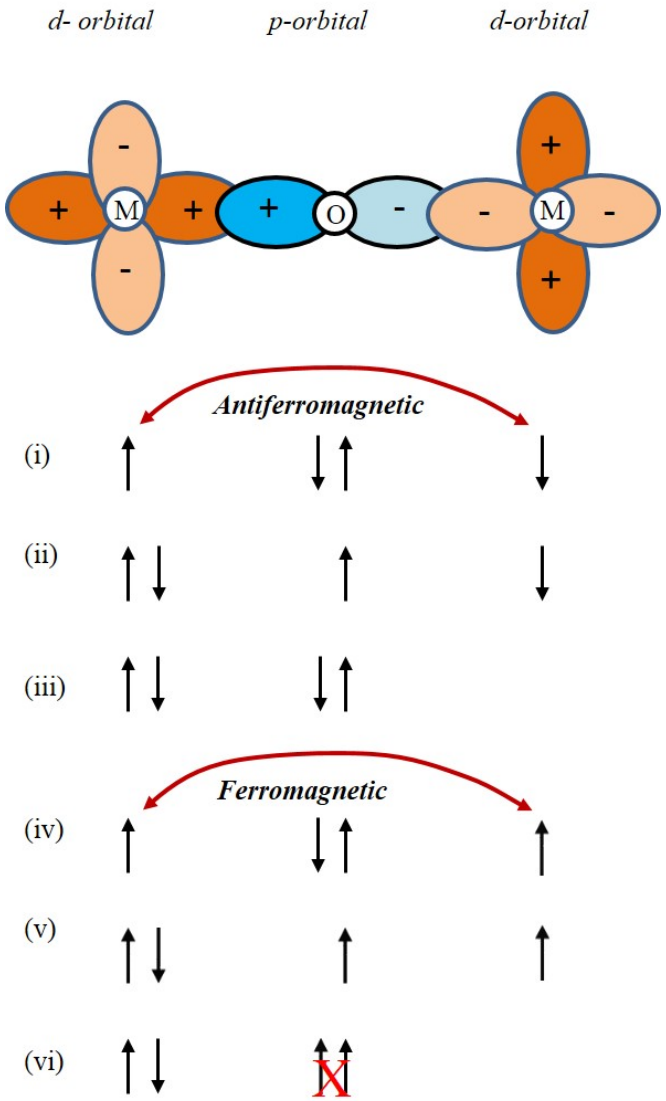

Figure 1.1 Schematic of superexchange interaction in magnetic oxides. The distribution of spins of four electrons in transition metals (M) and oxygen (O) is shown by up and down arrows [(i)-(vi)]. If moments in M interact antiferromagnetically, then (i) is a ground state whereas (ii) & (iii) are excited states with (iii) having the lowest energy between the two. If moments in M interact ferromagnetically, then ground state (iv) cannot have comparable low energy excited state (vi) because of Pauli exclusion principle. Thus antiferromagnetic configuration costs less energy and is more favorable by superexchange interaction. Figure from[14].

Figure 1.1 shows the schematic of superexchange between transition metal atoms via non-magnetic oxygen atom. To make it simple, we assume metal has at least one

unpaired electron, and oxygen has a tendency to attract two electrons to fulfill its valance shell. We can distribute and orient spins of four electrons in various ways within the whole molecule. In doing so, with antiparallel spin alignment of adjacent spins, spins will be delocalized and hence, the kinetic exchange energy will be minimized. Therefore, superexchange interaction leads to antiferromagnetic coupling of metal atoms with oxygen while keeping oxygen nonmagnetic.

In brief, coupling constant due to superexchange can be stated as $J \propto \frac{-t^2}{U}$ [17], where t, a probability amplitude for an electron to hop between neighboring ions, is called hopping integral, and U is a cost of creating excited state which comes from the repulsion between electrons of opposite spins (called Coulomb energy or Hubbard constant) when situated in the same atom. Among the two terms, the first one favors delocalized behaviors while the second term favors formation of localized moments. In competition between two, the first term is dominant, so the size of superexchange depends on the degree of overlap of the orbitals.

In some cases, superexchange interaction can be ferromagnetic as illustrated in the lower panel of Figure 1.1. This issue can be complex when geometry of orbital overlaps plays an important role which is addressed by Goodenough-Kanamori-Anderson and commonly known as GKA rules [20]. It can predict the types of magnetic interactions in most of the cases. In summary, GKA rules state that (a) when an angle between M-O-M is 180° and the exchange is due to an overlap between half-filled or empty orbitals, it is relatively strong and antiferromagnetic; (b) when 180° exchange is due to an overlap between an occupied and an empty orbital , it is relatively weak and ferromagnetic; (c)

when an angle between M-O-M is 90° and the exchange is due to overlap between half-filled orbitals, it is also relatively weak and ferromagnetic.

1.3 HEISENBERG HAMILTONIAN

The Heisenberg Hamiltonian (1.21) does not put any restrictions on the structure of the spin lattice. Thus, the Hamiltonian can be used to study spin lattice of D-dimensions, where D=1(chain lattice), D=2 (square lattice) and D=3(cubic lattice). Although real magnetic solids are three-dimensional, they can be treated as low-dimensional magnetic systems if couplings along one direction (along chain) are much stronger than perpendicular to that direction. For example, $CuSb_2O_6$ (studied in this work) has a much stronger intra-chain interaction than inter-chain, thus it can be considered as a quasi-one-dimensional magnetic system. On the other hand, $BiCu_2PO_6$ (also studied in this work) has a significant inter-chain interaction in comparison to intra-chain interaction thus, it is considered as bridge between quasi-one and quasi-two-dimensional magnetic system.

As mentioned earlier, the strength of exchange interaction J_{ij} in Eq. (1.21) falls off rapidly with increasing distance between spins. Therefore, it is sufficient to consider the interactions only between the nearest neighbor (NN) sites i and j. In many solids, J_{ij} has the same value for all NN sites thus, giving isotropic form of Heisenberg Hamiltonian (1.21) as,

$$H = J \sum_{i,j} \boldsymbol{s_i} \cdot \boldsymbol{s_j}. \tag{1.22}$$

However, we can find many magnetic systems where strength of exchange interactions between successive pairs of spins may not be same. When we include next-nearest neighbor (NNN) interactions in addition to NN, we get

$$H = J\sum_{i=1}^{N} \boldsymbol{s}_i \cdot \boldsymbol{s}_{i+1} + J'\sum_{i=1}^{N} \boldsymbol{s}_i \cdot \boldsymbol{s}_{i+2}. \quad (1.23)$$

When $J' = J/2$, it describes Majumdar-Ghosh chain[21].

Many real magnetic systems have various types of anisotropies and the fully anisotropic NN Heisenberg Hamiltonian in 1D is given by,

$$H_{XYZ} = \sum_{i=1}^{N} [J_x s_i^x \cdot s_{i+1}^x + J_y s_i^y \cdot s_{i+1}^y + J_z s_i^z \cdot s_{i+1}^z], \quad (1.24)$$

where N is the number of spins in the chain. As this Hamiltonian is symmetric for all three spin components, we can generalize it to arbitrary spin dimensions with *m*-spin components [22]. We can derive several special cases of this Hamiltonian depending on dimensions of spins (not to be confused with lattice dimension D). For *m*=1 and $J_x = J_y = 0, J_z \neq 0$, we get Ising model; for *m*=2 and $J_x \neq J_y \neq 0$, $J_z = 0$, we get XY model; and for *m*=3 and $J_x = J_y = J_z = J$, we get XXX or isotropic Heisenberg model. Also, for *m*=3 and $J_x = J_y = J_{xy} \neq 0, J_z \neq 0$, we get XXZ model as shown below,

$$H_{XXZ} = \sum_{i=1}^{N} [J_{xy}(s_i^x \cdot s_{i+1}^x + s_i^y \cdot s_{i+1}^y) + J_z\, s_i^z \cdot s_{i+1}^z], \quad (1.25)$$

where *xy*-plane has rotation symmetry but exchange interactions are different in *xy*-plane and along *z*-axis. We can use this to represent various regimes for a spin-½ chain as a function of J_z as shown in Figure 1.2 [23]. For $|J_z/J_{xy}| < -1$, the chain is in FM Ising phase with ground states of all spins aligned in either *z* or –*z* direction. In the limit $|J_z/J_{xy}| = -1$, we get isotropic Heisenberg ferromagnet. For $-1 < |J_z/J_{xy}| < 1$, XXZ

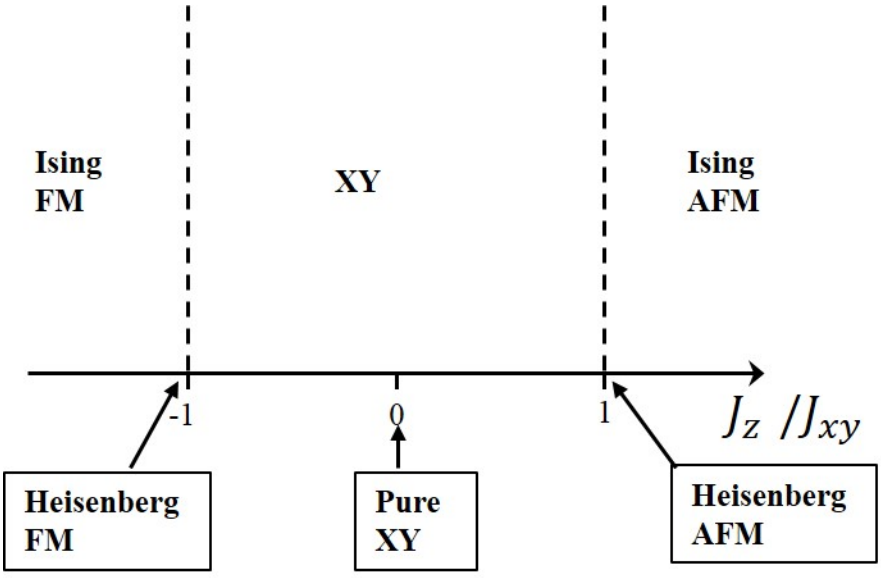

Figure 1.2 Different regimes for a spin-1/2 chains as a function of J_z/J_{xy}. Figure reproduced from Ref. [23].

chain is in XY phase and in the limit of zero it gets to pure XY phase. For $|J_z/J_{xy}| > 1$, the XXZ chain is in the AFM Ising or Neel phase and reaches the most interesting regime of isotropic Heisenberg AFM in the limit of $|J_z/J_{xy}| = 1$. There is an array of literature on these models and are summarized in ref. [24], [25]. Besides the basic exchange interaction terms, there may be other anisotropy terms which might need to be considered in full spin Hamiltonian.

1.4 QUANTUM SPIN CHAINS

Low-dimension, low-spin and frustration all enhance the quantum fluctuation, and novel ground state properties arise due to such fluctuations in low-dimension. Thus, this field of study is commonly referred as a quantum magnetism and effects of such fluctuations must be considered in addition to thermal fluctuations. Spin chain is a one dimensional array of spins. In such an array, individual spin can orient parallel or anti parallel to a particular direction giving an Ising chain, point anywhere in a fixed plane (XY

chain), or point in any direction (Heisenberg chain). Spin chain direction is fixed by the direction along which crystal structure allows the interaction of spins to be much stronger than the other two directions.

1.4.1 SPIN-½ CHAIN

The Bethe Anstaz (BA) gives a solution to the eigenvalue problem of spin-½ Heisenberg linear chain with NN interaction. In the case of FM system ($J < 0$) the exact ground state is a simple configuration because all *N* spins are oriented in a particular direction (either up or down) and the ground state energy is simply $E_g = JN/4$. One can create an excitation in the system by deviating a spin from its ground state orientation (from up to down or down to up). Exchange interaction makes such excitation to delocalize throughout the chain, i.e., excitation travels along the spin chain. Such excitation is called a spin wave or a magnon. The excited state energy w.r.t. the ground state energy is given by $\varepsilon(k) = J(1 - \cos ka)$.

We are more interested in AFM systems because the material studied in this work, ($CuSb_2O_6$), is a Heisenberg AFM spin-½ chain compound [26]–[28]. Bethe Anstaz can be applied in the case of AFM system ($J > 0$) as in the case of FM with the change in the sign of J. For the AFM ground state, N/2 spins are up and N/2 spins are down, and according to Lieb-Mattis theorem, the total spin of ground state is S=0 [29]. Also, the AFM ground state is spin disordered, i.e., it does not have long range order (LRO). The exact ground state energy is $E_g = \frac{JN}{4} - JN \ln 2$; which is lower than that of FM [24]. Low lying excitation spectrum has been calculated by des Cloizeaux and Pearson (dCP)[30]. The excitation spectrum for spin-1 state is given by,

$$\varepsilon(k) = \frac{\pi J}{2}|\sin ka|, \qquad \frac{-\pi}{a} \leq k \leq \frac{\pi}{a}, \tag{1.26}$$

where wave vector k is w.r.t. that of the ground state. More rigorous calculation which accounts for both spin-1 and spin-0 states is given in ref.[3]. Thus, low lying excited states can be written as $E(k_1, k_2) = \varepsilon(k_1) + \varepsilon(k_1)$ with $\varepsilon(k_i) = \frac{\pi J}{2}\sin k_i$ and total momentum as $k = k_1 + k_2$. At any total momentum k, spectrum is a continuum of scattering states with the lower boundary defined by dCP (see Eq. 1.26) with one of $k_i\,'s = 0$ and upper boundary is defined by,

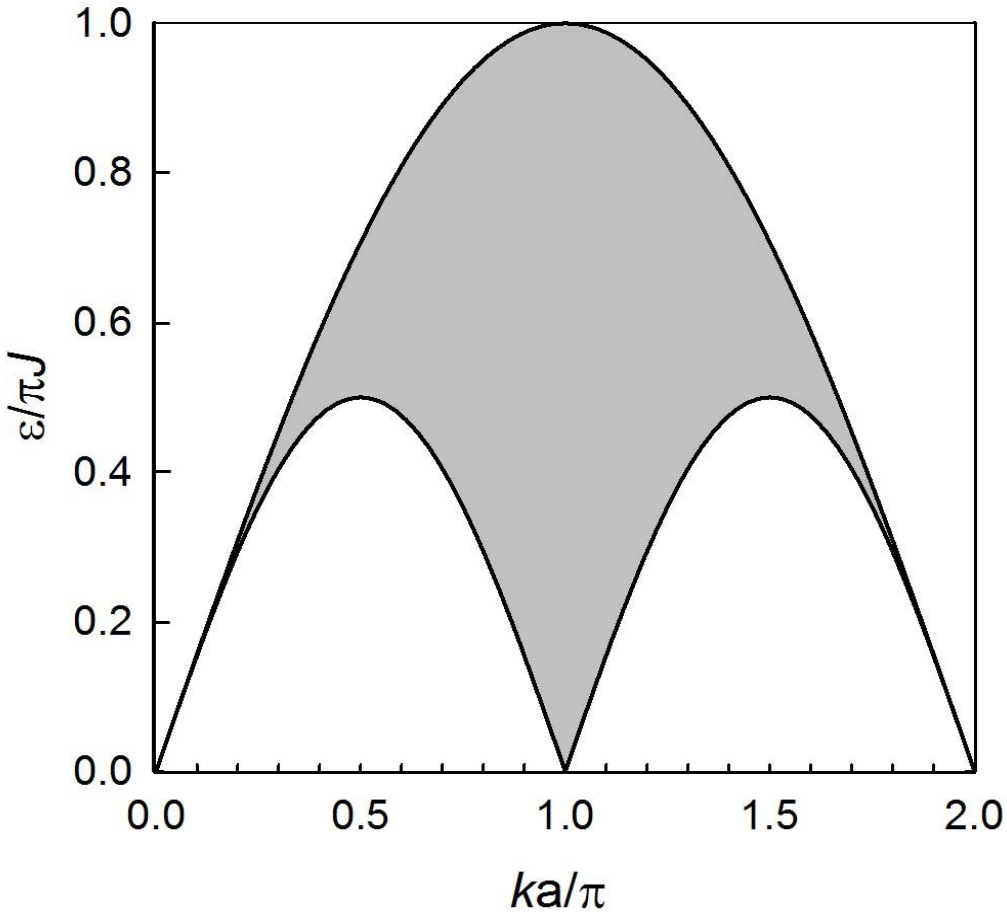

Figure 1.3 Two-spinon continuum of a spin chain. The lower and upper boundary are given by Eq. 1.26 and Eq.1.27 .

$$\varepsilon(k) = \pi J \left|\sin\frac{ka}{2}\right|, \qquad \& \; k_1 = k_2 = \frac{k}{2}. \tag{1.27}$$

These relations suggest that low lying spectrum is a combination of two elementary excitations called *spinons*. A spinon is a spin-½ object, and the energies and momenta of spinons simply add up such that both $S = 1$ and $S = 0$ states are possible. It is also clear that spinons are gapless. Also, for any even number of sites, the total spin will always be an integer, so that spins are always excited in pairs. Figure 1.3 shows the two-spinon continuum based on Eq. (1.26) and Eq. (1.27). The shaded region between the upper and lower boundaries can be populated by excited spinons. Spinons can be considered as fermions as they are spin-½. Also a fractional statistics[31], [32] has been proposed which describes spinons as *semions* with statistical properties intermediate between fermions and bosons. In a 1D system, it is possible to transform a fermionic basis to a bosonic basis by a method called bosonization [33], a useful technique for theoretical works.

1.4.2 SPIN-1 CHAIN (HALDANE CHAIN)

Prior to 1983, there was a general consensus that spin value had no significant effect on the magnetic properties of one-dimensional Heisenberg AFM (1D-HAFM) because of gapless excitation spectrum of spin-½ and its qualitative similarity with classical limit ($S \rightarrow \infty$). It was also based on the fact that in the cases of both spin-½ and classical limit, spin correlation length diverges as $T \rightarrow 0$, and when $T = 0$, quasi-Neel AF long-range magnetic order is established [34]. In 1983, Haldane[4], [35] conjectured that the 1D-HAFM chain with integer spin has a gapped excitation spectrum with an energy gap Δ, w.r.t. the ground state in contrast to the case of a gapless spectrum of half-integer spin. Such a one dimensional chain of integer spins is therefore known as a *Haldane chain* and the energy gap in the excitation spectrum is called a *Haldane gap*. The integer-spin systems also show

short-range order in their ground state with the spin correlation function decaying exponentially in contrast to power law decay of distance in half-integer spin system.

A general spin Hamiltonian for a Haldane spin chain can be written as [34],

$$H = J\sum_{i=1}^{N}[\boldsymbol{s}_i \cdot \boldsymbol{s}_{i+1} + \beta(\boldsymbol{s}_i \cdot \boldsymbol{s}_{i+1})^2 + \sum_{i=1}^{N}[D(s_i^z)^2 - g\mu_B s_i^{\alpha} H^{\alpha}], \qquad (1.28)$$

where the *z*-axis represents the chain direction and field is applied along $\alpha = x, y, z$. First and second isotropic terms represent NN HAFM exchange interaction ($J > 0$) and the biquadratic exchange term H_B. The third term represents the uniaxial single ion anisotropy which gives spin orientation, perpendicular to z-axis (easy-plane or XY-like anisotropy) for positive D and parallel to z-axis (easy-axis or Ising-like anisotropy) for negative D. The fourth term represents the Zeeman energy in an applied field. The Hamiltonian (Eq.1.28) is not exactly solvable. Even some attempts [36]–[38] to solve the above Hamiltonian with $D = H = 0$ did not give the gapped spectrum and hence could not explain the origin of spin gap.

A simple explanation for a spin gap (Haldane gap) in the spin-1 chain (Haldane chain) is given by Affleck, Kennedy, Lied and Tasaki (AKLT) [39] with $\beta = 1/3, D = H = 0$. They have shown that the ground state is a unique singlet state called a valence – bond solid (VBS) which is separated from the excited state with a gap, $\Delta = 0.75J$. Thus the Hamiltonian with VBS ground state for $S = 1$ with $\beta = 1/3$ can be written as,

$$H_{VBS} = J\sum_{i=1}^{N}[\boldsymbol{s}_i \cdot \boldsymbol{s}_{i+1} + \beta\,(\boldsymbol{s}_i \cdot \boldsymbol{s}_{i+1})^2. \qquad (1.29)$$

The ground state wave function of this Hamiltonian is constructed by considering each $S = 1$ spin as two S= ½ spins in a triplet state. Then, coupling of all NN spins-½ into a singlet gives a ground state and the pattern produced is the structure of the valence bond. Very rich phase diagram of the bilinear-biquadratic spin-1 chain given by Hamiltonian (1.29) with $J = \cos\theta$ and $J\beta = \sin\theta$ is shown in Figure 1.4. In this figure, the filled circles represent the exact solutions by various models [36]–[38], [40] and the open circle is for the Haldane point. The Haldane phase should occur within $\frac{-\pi}{4} < \theta < \frac{\pi}{4}$, and the points $\theta = \frac{-\pi}{4}$ & $\theta = \frac{\pi}{4}$, where the gap vanishes indicate the critical points separating it from other phases as shown in Figure 1.4.

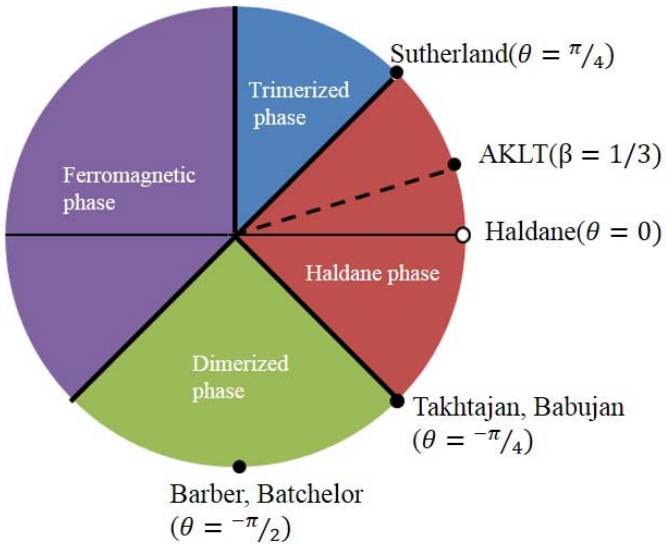

Figure 1.4 Phase diagram of the S=1 bilinear biquadratic Hamiltonian. From [34]

Another interesting approach is introduced by Gomez-Santos and developed by Meshkov, and Kohler and Schilling independently which gives a physical insight into the

Haldane phase[34]. In this method, disorder is introduced in the long range AFM state by means of spin–zero defects, which can be treated as fermions in Hartree-Fock approximation where the correlation length is simply the mean distance between two spin-zero defects. Many numerical calculations have been done (see ref.[34] for summarized work) for such systems to calculate ground state energy, Haldane gap, correlation length, dispersion law of excitation and some thermodynamic properties. Dispersion relation is given by,

$$\varepsilon(k) = \sqrt{\Delta^2 + c^2(\pi - ka)^2}; \text{ with } c = 2JS \tag{1.30}$$

where c is the quantum spin-wave velocity. For details on dispersion relation and several special cases see ref. [34].

1.4.3 ALTERNATING SPIN CHAIN WITH FRUSTRATION

We know that the uniform Heisenberg chain with NN-AFM interaction exhibits the Haldane gap for integer spin, and no gap for half-integer spin. This gap situation is quite different for a uniform chain with strong NNN-AFM interaction and for a non-uniform chain with alternating exchange interaction. An alternating AFM spin chain arises when a chain has two exchange constants $J_1 \geq J_2 > 0$, and alternate continuously from bond to bond along the chain. When a material has two major structurally inequivalent superexchange pathways that are linked together, an alternating chain with exchange interactions $J_1 - J_2 - J_1 - J_2$ is the result. The Hamiltonian for such system can be written as,

$$H = J_1 \sum_i [\boldsymbol{s}_i \cdot \boldsymbol{s}_{i+1} + \alpha(\boldsymbol{s}_i \cdot \boldsymbol{s}_{i+2})], \tag{1.31}$$

where $\alpha = J_2/J_1$ is called the alternating parameter. For $\alpha = 1$, we get uniform AFM Heisenberg chain, which is gapless. Spin-Peierls effect or transition is one important mechanism, which gives such an alternating chain in a spin-½ system.

1.4.3.1 SPIN-PEIERLS TRANSITION

Spin-Peierls transition is a magnetic analogue of Peierls transition which is a metal-insulator transition in a quasi-one-dimensional metal [41]. While Peierls transition opens up a gap in an electronic spectrum due to electron-phonon coupling, spin-Peierls transition opens up a gap in a magnetic excitation spectrum due to the coupling of the 1D-spin system with a 3D-lattice. A quasi-one-dimensional AFM Heisenberg chain of half-integer spin is one of the conditions required for spin-Peierls transition. Finite magneto-elastic coupling (i.e., dependence of exchange coupling on distance between spin sites) is another prerequisite for such transition. Above the spin-Peierls transition temperature (T_{sp}), the distance between NN spin is uniform, but below that transition temperature (T_{sp}), the distance between NN spin is no longer uniform, but alternate as shown in Figure 1.5(b). Now, because of finite magneto-elastic coupling, the AFM exchange also alternates along the chain, thus forming the spin singlet between the strongly coupled spin pair. Each coupled spin pair is known as a dimer and the process is called dimerization.

The process of dimerization originates because of the tendency to reduce the energy of the system. The magnetic energy gained by the system due to dimerization exceeds the loss of elastic energy due to lattice distortions along the chain and becomes maximum at $T = 0\ K$. The magnitude of the gap between a singlet ground state and the lowest lying band of triplet excited state, is proportional to the degree of dimerization, and hence to the degree of lattice distortion [42]. Thus, the gap is zero for uniform chain, which has no

lattice distortion and hence no dimerization. In this view, spin-Peierls transition can also be defined as the three-dimensional phase transition driven by quasi-one-dimensional magnetism.

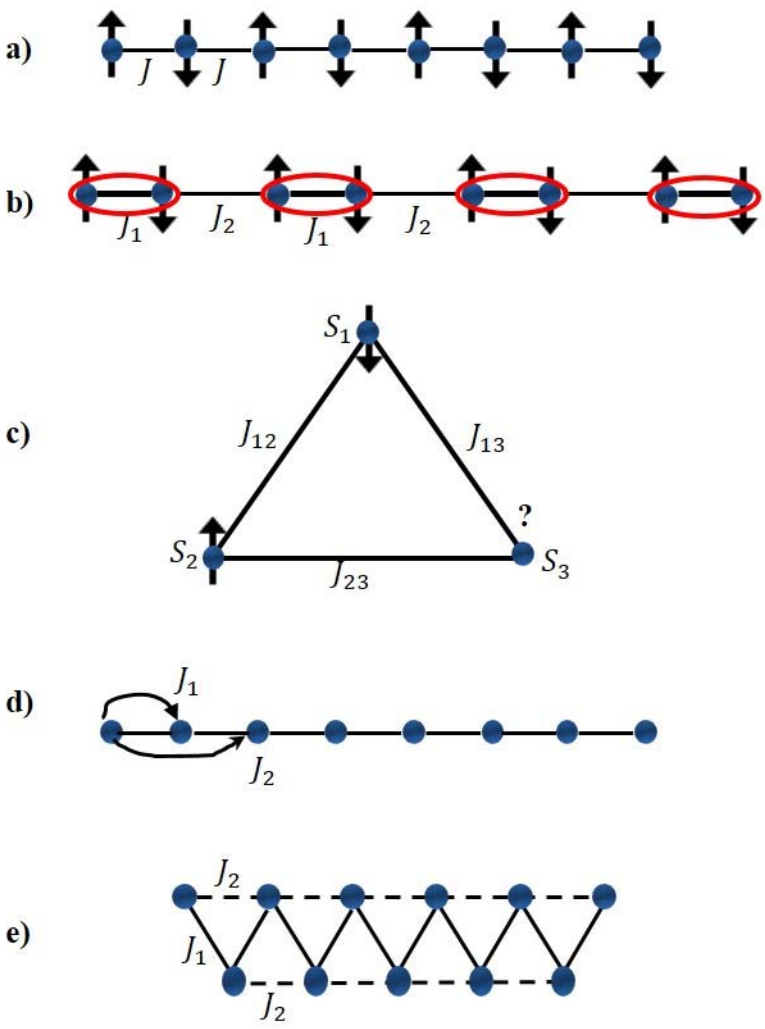

Figure 1.5 Schematic representation of a) uniform Heisenberg AFM chain, b) Singlet ground state of dimerized chain below spin-Peierls transition T_{sp} and hence giving alternating exchange interaction, c) frustration in a triangular lattice, d) competition between NN exchange J_1 and NNN exchange J_2 inducing frustration in a chain, and e) two-leg ladder with zigzag chain, another frustrated spin system.

Several characteristic features facilitate the experimental identification of spin-Peierls transition. A sharp drop of magnetic susceptibility below T_{sp} due to formation non-

magnetic spin singlet is one of the important characteristic features. In 1993, $CuGeO_3$ was recognized as the first inorganic material showing such transition based on magnetic susceptibility measurement [43]. Another such feature is the characteristic magnetic field dependence of transition temperature T_{sp}. After the discovery of first inorganic spin-Peierls material, a plethora of research work have been done on this material, and the possibility of impurity doping by large numbers of elements like Zn, Si, Ni, Ca etc. made this material a toy model to study different hypotheses. For review on spin-Peierls materials see Ref. [44].

1.4.3.2 FRUSTRATION

The alternating parameter, $\alpha = J_2/J_1$ with $\alpha > 0$ defined in section (1.4.3) is also used as a measure of frustration in the magnetic system. Thus, frustration comes into play when NNN-AFM exchange interaction is included in the system. Frustration is the inability of a system to satisfy all interactions in that system to find the ground state. Because of this, it is often possible to have no single unique ground state but verity of similar low energy states of the system in which non-minimum energy is shared around as much as possible [42]. It can be understood by considering a simple triangular lattice as shown in Figure 1.5(c). Among three spins in a triangle, if spin S_1 is down then the optimization of J_{12} tells the spin S_2 to be up. At the same time, J_{13} and J_{23} give conflicting information about orientation to spin S_3, thus S_3 cannot orient in any particular direction introducing frustration to the system. Also, a two-leg ladder with zigzag chain structure, as shown in Figure 1.5(e), and a linear chain as shown in Figure 1.5(d) are frustrated spin structures because of the competition between NN (J_1) and NNN (J_2) exchange interaction.

$BiCu_2PO_6$, studied in this thesis, is one of the examples of real materials which show a two-leg ladder with zigzag chain along the leg of the ladder.

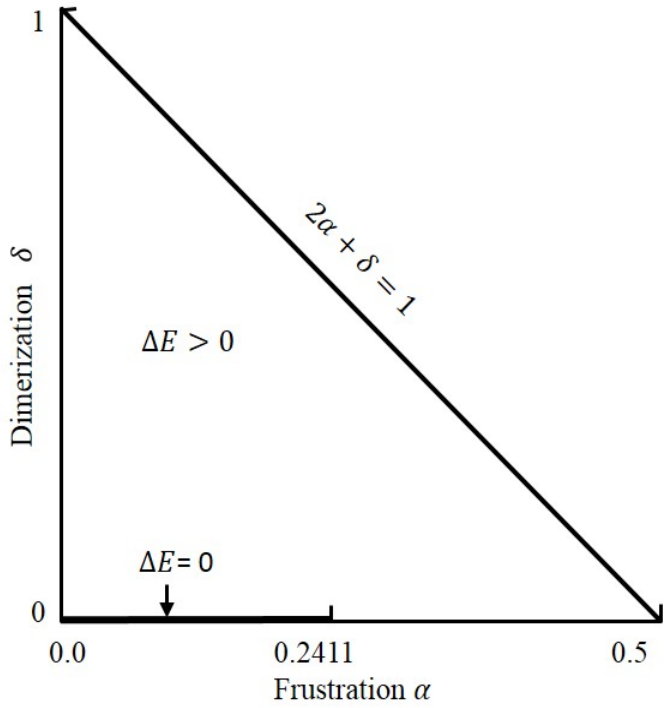

Figure 1.6 Schematic of phase diagram of Heisenberg spin-½ AFM chain as a function of frustration α and dimerization δ at $T = 0\ K$. From [46] .

Hamiltonian, describing both frustration and dimerization in a quasi-one-dimensional system, can be written by adding a dimerization operator in Hamiltonian (1.31) as [45],

$$H = J_1 \sum_i [(1 - (-1)^i \delta)\boldsymbol{s}_i \cdot \boldsymbol{s}_{i+1} + \alpha(\boldsymbol{s}_i \cdot \boldsymbol{s}_{i+2})], \tag{1.32}$$

where δ accounts for the dimerization and $J_1(1 \pm \delta)$ represents the alternating coupling between nearest neighbors. As defined previously, αJ_1 represents the alternating parameter for the next-nearest neighbor. It can be deduced (as shown in Figure 1.6) that for $\delta = 0$ and $\alpha = 0$, we get a uniform Heisenberg chain which exhibits a gapless excitation

spectrum. For $\delta = 0$, the ground state remains gapless, as long as the frustration parameter α does not exceed the critical value $\alpha_c = 0.2411$, which is resulted from various calculations [45][46]. For $\alpha > \alpha_c$ and $\delta = 0$, the ground state is dimerized due to formation of singlet pair (because of spontaneous symmetry breaking). We can obtain a Majumdar-Ghosh chain as described by Eq. (1.23) in the limiting case of $\alpha = 0.5$ and $\delta = 0$ (also known as Majumdar-Ghosh point). The Hamiltonian of MG chain can be solved exactly and the obtained ground state is made up of spin dimers with a finite energy gap. Exact results can also be found for the ground state on the line $2\alpha + \delta = 1$, which is a product of wave functions of singlet dimers[21], [47]. The gap opens up as soon as the dimerization turns on ($\delta > 0$). Any chain model with both NNN exchange (frustration) and alternation, is equivalent to a spin ladder model. It will be discussed in the following section.

1.4.4 SPIN LADDERS IN-BETWEEN 1D AND 2D

To this point, we have mainly focused on a strictly one-dimensional Heisenberg Hamiltonian, i.e., we have neglected inter-chain interactions in the system. In a real world, it is almost impossible to find a perfectly one-dimensional spin chain material. Therefore, spin chain material with weak inter-chain interaction,(i.e., $J_\perp/J_\parallel < 10^{-2}$) are considered a one dimensional system or a quasi-one-dimensional system. Thus, most of the real material considered as one-dimensional are actually quasi-one-dimensional systems. Now, if $J_\perp$ is significant and cannot be neglected, then we have n-coupled chains, where n is the number. of chains coupled in the system. These kind of coupled chains are called n-leg spin ladders (as they resemble ladders) where “leg” is given by $J_\parallel$ exchange coupling and “rung” is given by $J_\perp$ coupling. Thus, a crossover from a 1D chain to a 2D square lattice is represented by these n-leg spin ladders. A special case of n-leg ladder, two-leg ladder ($n =$

2) and three-leg ladder ($n = 3$) are shown in Figure 1.7. The Hamiltonian for n-leg ladder is given by [48],

$$H = J_{\parallel} \sum_{i} \sum_{n} \boldsymbol{s}_i(n) \cdot \boldsymbol{s}_{i+1}(n) + J_{\perp} \sum_{n} \boldsymbol{s}_1(n) \cdot \boldsymbol{s}_2(n+1). \tag{1.33}$$

And for $n = 2$ it reduces to,

$$H = J_{\parallel} \sum_{i} [\boldsymbol{s}_i(1) \cdot \boldsymbol{s}_{i+1}(1) + \boldsymbol{s}_i(2) \cdot \boldsymbol{s}_{i+1}(2)] + J_{\perp} [\boldsymbol{s}_1(1) \cdot \boldsymbol{s}_2(2)]. \tag{1.34}$$

Surprisingly, the transition from 1D to 2D is not smooth, and the properties of the system strongly depend on whether n is odd or even [49]. Even-leg ladder possesses a spin gap and has a spin liquid ground state because of a short range and exponentially decaying spin correlation. Therefore, even-leg ladders may be regarded as the realization of a resonating valence band model (RVB) state, as proposed by Anderson [50]. On the other hand, odd-leg ladders behave quite differently and show properties of single chain, i.e., gapless spin excitations and a power-law falloff of the spin-spin correlations. We will try to deduce these properties based on ratio $J_{\perp}/J_{\parallel}$.

For even-leg ladders, when the ratio $J_{\perp}/J_{\parallel} = 0$, (i.e., rung coupling is vanishing) one obtains two decoupled AFM spin ½ chain and the excitation spectrum is gapless. In the isotropic limit of $J_{\perp}/J_{\parallel} = 1$, the ladder spin system would always be in a spin liquid state with a short range spin correlation and a spin gap, whereas, a corresponding classical system possesses the Neel type ordered ground state. In the coupling limit, $J_{\perp}/J_{\parallel} > 0$, the rungs are only weakly coupled, and in the extreme limit $J_{\parallel} = 0$, decoupled from each other. In such a case, the ground state is the product state with the spins on each rung forming a singlet and the overall spin of the system is zero. This ground state is separated from an excited rung triplet by an energy $J_{\perp}$. When the leg coupling is turned on, (i.e., $J_{\perp} \gg J_{\parallel}$) the

triplet excitation delocalizes and S=1 magnons propagate with dispersion law $\omega(k) = J_\perp + J_\parallel \cos(k)$. The spin gap, minimum excitation energy in the zone boundary, is $\Delta_{spin} = \omega(\pi) \approx J_\perp - J_\parallel$. As mentioned before, such spin liquid state is described by the RVB state. In the weak coupling limit, i.e., with increasing $J_\parallel$, the triplon excitation form a band with bandwidth nearly equal to $J_\parallel$ and then the gap decreases. The spin gap of two-leg ladder opens up immediately with turning on rung coupling, and varies as a function of $J_\perp/J_\parallel$. For higher even-leg ladders, the gap size decreases with increasing *n,* but its magnitude remains non-zero for finite even-leg ladders[51].

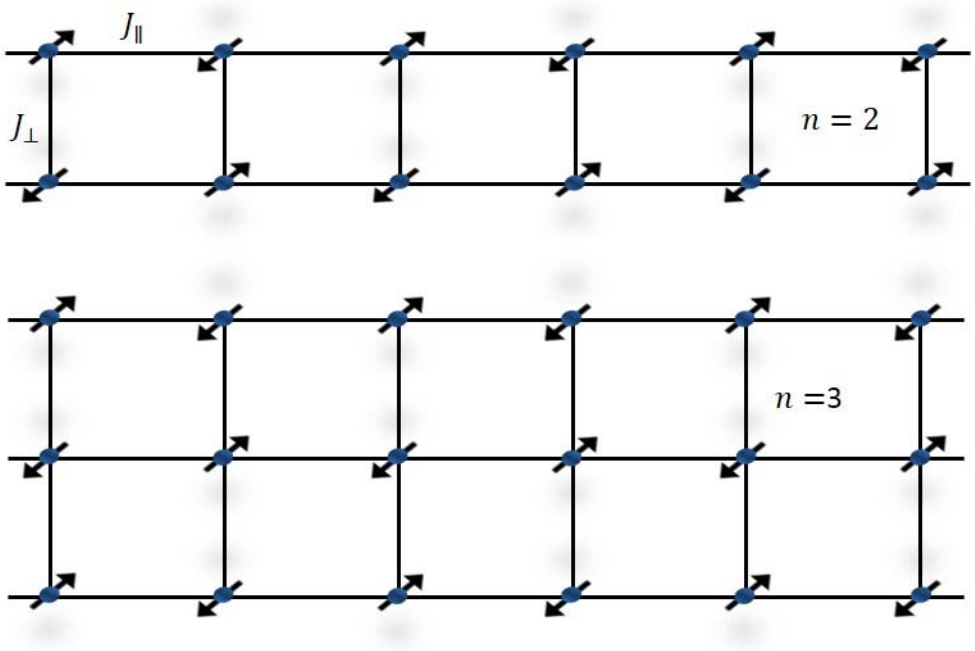

Figure 1.7 Schematics of 2-leg and 3-leg ladders with $J_\parallel$ and $J_\perp$ showing the coupling along the legs and rungs respectively.

The case of n-odd leg ladders can be understood by considering 3-leg ladders. Although spin singlet can be formed on each rung, as in 2-leg ladders, there remains one

unpaired spin on each rung. Thus, each rung can be treated as spin-½ and the whole ladder is equivalent to spin-½ 1D Heisenberg chain, with gapless spectrum. This argument can be generalized to all odd-leg ladders [49].

CHAPTER II

BACKGROUND ON THERMAL TRANSPORT IN SOLID

The aim of this chapter is to present a brief introduction to thermal transport in solids, and some background on the methods used to analyze thermal conductivity data in this work. Several text books [52]–[54] and specialized books [55]–[57] are available for various approaches to derive general expressions for thermal conductivity. Basic derivations presented here will be based on those references, unless cited otherwise. I will mainly focus on the different mechanisms and modes that govern thermal conduction in insulating solids because all the materials studied in this thesis are insulators.

2.1 KINETIC THEORY OF THERMAL TRANSPORT

For a small temperature gradient, the thermal current density $\boldsymbol{j}$ is given by,

$$\boldsymbol{j} = -\kappa \boldsymbol{\nabla} T, \tag{2.1}$$

where proportionality constant κ is thermal conductivity, and $\boldsymbol{\nabla} T$ is a temperature gradient. In a temperature gradient $\boldsymbol{\nabla} T$, a particle with heat capacity c, and a velocity $\boldsymbol{v}$, will gain energy of $-c\boldsymbol{\nabla} T \cdot \boldsymbol{v}t$. In order to keep thermal equilibrium with the surrounding, a particle moving with velocity $\boldsymbol{v}$ must change its energy by,

$$\frac{\partial E}{\partial t} = -c\boldsymbol{\nabla} T \cdot \boldsymbol{v}. \tag{2.2}$$

The average distance a particle travels before a collision (which is called mean free path, l) is $l = v\tau$, where τ is relaxation time. The thermal current per unit area then depends on

this distance, i.e., mean free path, l. For n particles in a given volume, the current density is given by,

$$\boldsymbol{j} = -nc\boldsymbol{\nabla}T\langle \boldsymbol{v}\cdot\boldsymbol{v}\rangle\tau. \tag{2.3}$$

Assuming the velocity to be isotropic, averaging it over all directions, and replacing nc with total specific heat,

$$\boldsymbol{j} = -\frac{1}{d}\mathrm{C}v^2\tau\,\boldsymbol{\nabla}T, \tag{2.4}$$

where d is the dimensionality of the system. Comparing Eq. (2.4) with Eq. (2.1), in three dimension, we can write,

$$\kappa = \frac{1}{3}\mathrm{C}v^2\tau = \frac{1}{3}Cvl. \tag{2.5}$$

Eq. (2.5) can be generalized for various excitations like phonons, electrons, magnons etc,

$$\kappa_i = \frac{1}{3}\sum_i C_i v_i l_i. \tag{2.6}$$

In general, Eq. (2.6) gives a very good phenomenological description of thermal conductivity, and is useful to estimate the order of magnitude. This universal description (independent of the nature of particles) of thermal conductivity (Eq.(2.6)) includes several assumptions which make it simple. The particle velocity is assumed to be energy independent which is true in the case of an electron, but for the case of a phonon, it is only valid at low temperature. In case of a magnon, its validity is strongly limited because of its energy independence. A more sophisticated version of Eq.(2.5) (with wave vector dependence of its constituents) can be derived using Boltzmann transport equation, and our focus will be on thermal conduction by phonons.

Lattice thermal conduction is the major thermal conduction mechanism in non-metals. Phonons are the quanta of crystal vibrations, and in the presence of temperature

gradient, thermal energy is considered as propagating by means of phonons. Each such phonon can be represented as a vibration of lattice with wave vector $\boldsymbol{k}$. A group of phonons centered around a wave vector $\boldsymbol{k}$ and differed by $\Delta\boldsymbol{k}$ can be considered as a packet of wave which propagates with group velocity $\boldsymbol{v_g} = \frac{\partial\omega(\boldsymbol{k})}{\partial\boldsymbol{k}}$.

2.2 THE BOLTZMANN EQUATION

The well-known Boltzmann equation for phonons has the form of [53]–[55], [58]

$$\left.\frac{\partial N(\boldsymbol{k})}{\partial t}\right|_{tot} = -\boldsymbol{v}_g \cdot \left.\frac{\partial N(\boldsymbol{k})}{\partial \boldsymbol{r}}\right|_{drift} + \left.\frac{\partial N(\boldsymbol{k})}{\partial t}\right|_{Scatt}, \tag{2.7}$$

where phonon distribution function $N(\boldsymbol{k})$ represents the average number of phonons with wave vector $\boldsymbol{k}$, and $\boldsymbol{v}_g$ represents the phonon group velocity. The left side of the Eq.(2.7) is the total change in the phonon distribution function, and it is equal to the sum of change caused by drift of phonons, (i.e., change in position with respect to surrounding) and by scattering of phonons with each other or with impurities or defects. When a steady state is established, the distribution function remains constant, and its time derivative vanishes, (i.e., phonon density at all points in a crystal becomes independent of time). Then, Eq. (2.7) becomes,

$$-\boldsymbol{v}_g \cdot \boldsymbol{\nabla} T \left.\frac{\partial N(\boldsymbol{k})}{\partial T}\right|_{drift} + \left.\frac{\partial N(\boldsymbol{k})}{\partial t}\right|_{Scatt} = 0. \tag{2.8}$$

In equilibrium, the phonon distribution function can be written as,

$$N^0(\boldsymbol{k}) = \frac{1}{\exp\left(\frac{\hbar\omega(\boldsymbol{k})}{k_B T}\right) - 1}. \tag{2.9}$$

The relaxation-time method assumes that scattering processes tend to restore a phonon distribution to thermal equilibrium distribution, at a rate proportional to departure of

distribution from equilibrium. It is also assumed that in the presence of temperature gradient, $\frac{\partial N(\boldsymbol{k})}{\partial T}$ at drift term can be replaced with$\frac{\partial N^0(\boldsymbol{k})}{\partial T}$. With Eq. (2.8), we can write,

$$\boldsymbol{v}_g \cdot \boldsymbol{\nabla} T \frac{\partial N^0(\boldsymbol{k})}{\partial T}\bigg|_{drift} = \frac{N^0(\boldsymbol{k}) - N(\boldsymbol{k})}{\tau(\boldsymbol{k})}, \tag{2.10}$$

where $\tau(\boldsymbol{k})$ is the phonon scattering relaxation time. This equation gives deviation from thermal equilibrium and thus a flow of heat. The thermal current due to a phonon mode $\boldsymbol{k}$ is the product of average phonon energy and the group velocity of propagation. The total heat current carried by all phonon modes is given by,

$$\boldsymbol{j} = \sum_{\boldsymbol{k}} N(\boldsymbol{k}) \hbar\omega(\boldsymbol{k}) \boldsymbol{v}_g. \tag{2.11}$$

Combining Eq. (2.11) and Eq. (2.10) and averaging velocity over all directions (see ref.[59] for details), we get

$$\boldsymbol{j} = -\frac{1}{3}\sum_{\boldsymbol{k}} \hbar\omega(\boldsymbol{k}) \boldsymbol{v}_{\boldsymbol{g}}^{\boldsymbol{2}} \tau(\boldsymbol{k}) \boldsymbol{\nabla} T \frac{\partial N^0(\boldsymbol{k})}{\partial T}. \tag{2.12}$$

From Eq. (2.1) and Eq. (2.12), we can write,

$$\kappa = -\frac{1}{3}\sum_{\boldsymbol{k}} \hbar\omega(\boldsymbol{k}) v_{\boldsymbol{g}}^{\boldsymbol{2}} \tau(\boldsymbol{k}) \frac{\partial N^0(\boldsymbol{k})}{\partial T}. \tag{2.13}$$

It is required to use some assumptions to get the meaningful results from Eq. (2.13). The Debye approximation assumes a simple linear dispersion relation of the form $\omega(\boldsymbol{k}) = v\boldsymbol{k}$ for each branch of phonon spectrum and this v (phonon velocity, approximately equal to the velocity of sounds in solids) is same for all three polarizations. The summation in Eq. (2.13) can be replaced with integral,

$$\kappa = -\frac{1}{3}\int \hbar\omega(\boldsymbol{k}) v_{\boldsymbol{g}}^{\boldsymbol{2}} \tau(\boldsymbol{k}) \frac{\partial N^0(\boldsymbol{k})}{\partial T} f(\boldsymbol{k}) d\boldsymbol{k}, \tag{2.14}$$

where, $f(\boldsymbol{k})d\boldsymbol{k} = \frac{3k^2\,d\boldsymbol{k}}{2\pi^2}$ (number of phonon modes between k and $k + dk$ per unit volume of crystal) which leads to $f(\omega)d\omega = \frac{\boldsymbol{3\omega^2\,d\omega}}{\boldsymbol{2\pi^2\,v^3}}$**.** Substituting Eq.(2.9) in Eq.(2.14) with Debye approximation, we get

$$\kappa = \frac{1}{2\pi^2\,v}\int_{\boldsymbol{0}}^{\boldsymbol{\omega_D}} \hbar\omega^3\tau(\omega)\frac{\left(\frac{\hbar\omega}{k_BT^2}\right)\exp\left(\frac{\hbar\omega}{k_BT}\right)}{[\exp\left(\frac{\hbar\omega}{k_BT}\right)-1]^2}\,d\omega, \tag{2.15}$$

where, Debye frequency($\boldsymbol{\omega_D}$) is defined in such a way that $3N(=\int_0^{\boldsymbol{\omega_D}} f(\omega)d\omega)$ are total number of phonon modes. Following standard substitution, $x = \frac{\hbar\omega}{k_BT}$ and defining Debye temperature $\theta_D = \frac{\hbar\omega_D}{k_B}$, we can write Eq. (2.15) as,

$$\kappa = \frac{k_B}{2\pi^2\,v}\left(\frac{k_B}{\hbar}\right)^{\boldsymbol{3}} T^3\int_{\boldsymbol{0}}^{\theta_D/T} \tau(x)\frac{x^4e^x}{[e^x-1]^2}\,dx. \tag{2.16}$$

Within Debye approximation, the differential contribution to heat capacity in terms of dimensionless parameter x is,

$$C(x)dx = \frac{3k_B}{2\pi^2\,v^3}\left(\frac{k_B}{\hbar}\right)^{\boldsymbol{3}} T^3\frac{x^4e^x}{[e^x-1]^2}\,dx. \tag{2.17}$$

Then, Eq. (2.17) with $l(x) = v\tau(x)$ can be written as

$$\kappa = \frac{1}{3}\int_0^{\theta_D/T} C(x)vl(x), \tag{2.18}$$

which is a more rigorous (because of wave vector dependence of *C* and *l*) form of Eq.(2.6) obtained from simple kinetic theory. The Eq. (2.16) is called Debye approximation for the lattice thermal conductivity, because of the approximation of k-independent phonon velocity for all acoustic branches. From Eq. (2.16) we can see that by calculating the relaxation times for various scattering processes in solids, and adding scattering rates as,

$$\tau^{-1}(x) = \sum_i \tau_i^{-1}(x), \tag{2.19}$$

we can calculate lattice thermal conductivity. Before that, we will discuss the important scattering mechanisms which contribute to lattice thermal conductivity.

2.3 SCATTERING MECHANISM

In case of a defect free or perfect crystal described by a system of coupled harmonic oscillators, thermal waves should propagate without interacting with one another. Then, there would be no mechanism to restore the equilibrium phonon distribution back from arbitrary distribution even in the absence of temperature gradient. This leads to an infinite thermal conductivity. In contrast, even in large defects free crystal, the thermal conductivity is found to be finite. Then, there should be a scattering mechanism which brings thermal conductivity to a finite value.

2.3.1 PHONON-PHONON SCATTERING

For the phonon scattering mechanism, it is necessary to extend harmonic potential of a lattice to non-harmonic terms, i.e., cubic, quadratic etc. This order of lattice potential corresponds to a number of phonons involved in the scattering process, i.e., three phonon interaction for lattice potential of the cubic order. The cubic term will be enough to account for thermal conductivity, and to illustrate the possible role of phonon-phonon scattering on thermal conductivity. In the three phonon process, a phonon in $(\boldsymbol{k}_1, \omega_1)$ mode may interact with a phonon in $(\boldsymbol{k}_2, \omega_2)$ mode and result in a phonon in $(\boldsymbol{k}_3, \omega_3)$ mode or vice versa. In such a process both momentum and energy are conserved, i.e.,

$$\boldsymbol{k}_1 + \boldsymbol{k}_2 = \boldsymbol{k}_3 + \boldsymbol{G} \tag{2.20}$$

and ,

$$\hbar\omega_1 + \hbar\omega_2 = \hbar\omega_3, \tag{2.21}$$

where $\boldsymbol{G}$ is a reciprocal lattice vector.

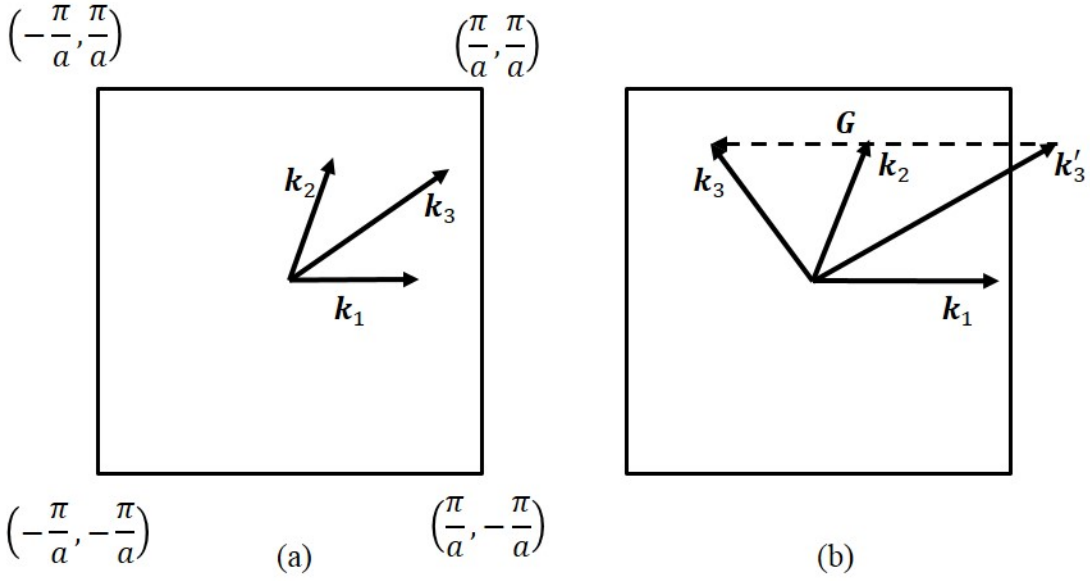

Figure 2.1 Phonon-phonon scattering a) normal process and b) Umklap process

We can divide the three phonon processes, based on whether the lattice momentum or wave vector are conserved or not, i.e value of $\boldsymbol{G}$ is zero or not. For $\boldsymbol{G} = 0$, Eq. (2.20) states the conservation of momentum and that process is called Normal process (N-process), whereas momentum does not conserve for $\boldsymbol{G} \neq 0$ and the process is called Umklapp process (U-process). For N-processes, two phonons with wave vectors $\boldsymbol{k_1}$ and $\boldsymbol{k_2}$ are scattered as shown in Figure 2.1(a); resulting into a phonon with wave vector $\boldsymbol{k_3}$, which still lies within the first Brillouin zone. Thus, effective direction of energy flow carried by $\boldsymbol{k_1}$ and $\boldsymbol{k_2}$remains unchanged for $\boldsymbol{k_3}$. For U-processes, the resulting phonon lies outside the first Brillouin zone as shown in Figure 2.1(b), which can be folded back (*umklappen* in German language) into the first Brillouin zone by means of reciprocal vector. Thus, effective direction of energy flow changes for the U-process, which tends to return any phonon distribution back to equilibrium. Therefore, in the absence of U-processes, N-processes cannot account for finite thermal conductivity. Although N-processes themselves

do not give rise to thermal resistance, they may have a strong impact on other frequency-dependent resistive scattering processes, because they may alter the distribution of possible phonon states [60]–[62].

2.3.2 BOUNDARY SCATTERING

Since nature does not provide crystals of infinite size, it is necessary to consider the effects of crystal size on the magnitude of thermal conductivity. It arises because most of the scattering mechanisms are ineffective for phonons of sufficiently long wavelengths, and at sufficiently low temperature, mean free path (l) is as large as the dimension of a crystal. It is evident from experiments that thermal conductivity decreases due to the scattering of phonons at the external boundaries of the crystal. This mechanism also prevents conductivity from increasing indefinitely at low temperature. In the case of solids consisting of compacted microcrystalline aggregates, boundary scattering severely reduces thermal conductivity and can be described by phonon mean free path of the order of magnitude of the crystallite size. Materials studied in this thesis are all single crystals and such a severe effect is not anticipated. Although it seems like boundary scattering is observed only at low temperature, its effect can be seen at temperatures much higher than thermal conductivity maximum[55].

2.3.3 SCATTERING BY DEFECTS

In the real world, defects are always present in a crystal, and from the experiment it is found that at low temperature, thermal conductivity decreases with increasing defects density. This effect is also observed in the temperature region of maximum conductivity, where phonon defect scattering is the predominant scattering mechanism. It is important to know how various types of defects scatter phonons, to explain the dependence of thermal

conductivity on defects. Such scattering of phonons by lattice defects has been studied by several [54], [60], [63] to account for its effects on thermal conductivity. Most common type of defects known for its influence in thermal conductivity include point defects, dislocation, larger defects, isotopes etc. Usually a defect with linear dimensions, much smaller than a phonon wavelength, is considered as a point defect. Examples of point defects are lattice vacancy, wrong atom in a lattice of correct atoms etc. It has been shown that scattering by point defect is analogous to Rayleigh scattering, and its relaxation rate is proportional to ω^4[57]. The physical picture behind this is the invisibility of point defects for large wavelength phonons at low temperature. Effects of scattering of phonons by dislocation, to the thermal conductivity, can be accounted by adding separately, the effect of the core ($1/\tau \propto \omega^3$) and of the surrounding strain field ($1/\tau \propto \omega^1$) in Eq.(2.19).

2.4 GENERAL *T*-DEPENDENCE OF THERMAL CONDUCTIVITY

Based on the above discussed scattering mechanism, we can qualitatively derive the temperature dependence of thermal conductivity in non-metal. It consists of several temperature regions of interest at which particular scattering processes are responsible for the evolution of thermal conductivity.

At very low temperature ($T \ll \theta_D$), only small number of phonon states are excited and their wave vectors are near Brillouin zone leading to non-resistive N-processes. The wavelength of such low energy phonons are very large and limited mainly by sample boundary resulting in a constant mean free path (l_b). According to Debye approximation, specific heat depends on temperature as, $C \propto T^3$. Therefore, with constant mean free path, the only temperature dependent term in Eq. (2.6) is specific heat, and it follows that thermal conductivity also increases as $\kappa \propto T^3$. In the region of peak or maximum thermal

conductivity ($T < \theta_D$), defect scattering is the dominant mechanism to limit mean free path, and hence to limit κ. This reduction is dependent on type and density of defects as discussed above.

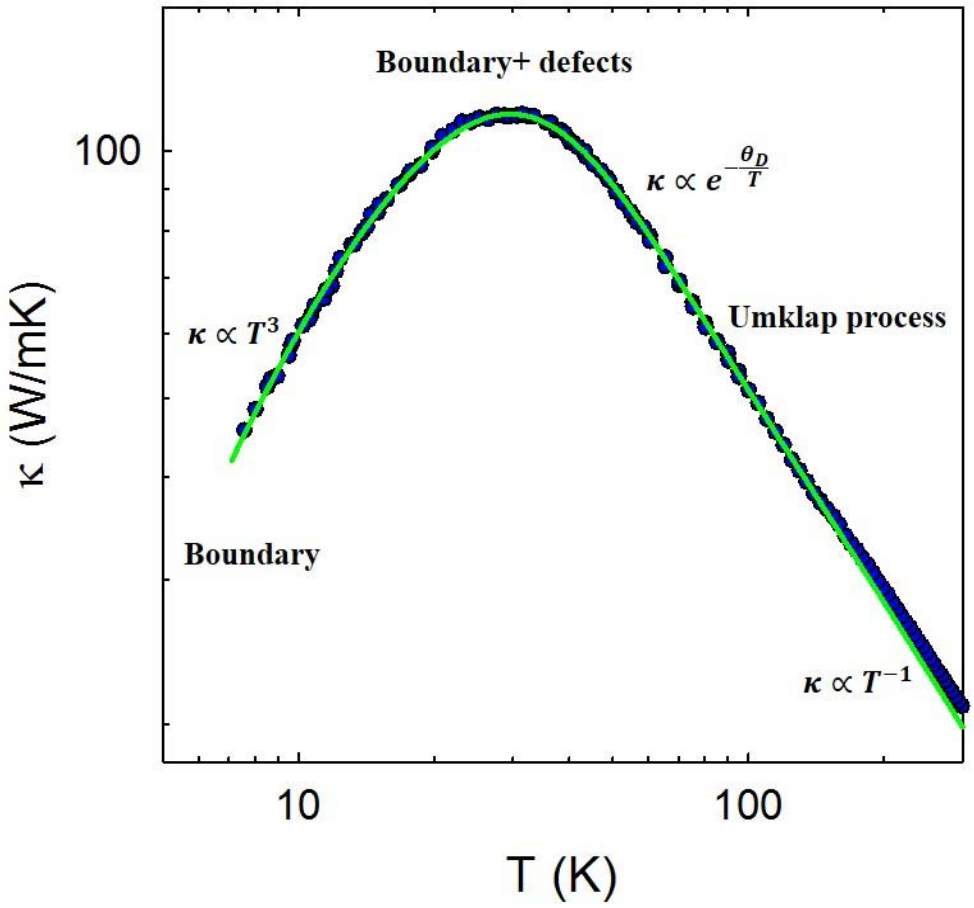

Figure 2.2 Typical temperature dependence of κ in insulators and dominant phonon scattering processes in the specific temperature range. Filled solid curve is thermal conductivity of $ZnSb_2O_6$ and solid line is fit to the data using Eq.(2.16) with relaxation rates of processes described in figure. From [76].

At intermediate temperature ($T \approx \theta_D$), large number of phonon states with sufficiently large wave vectors near the Brillouin zone are available, and the conduction is governed by U-processes. With increase in temperature, U-processes increase and finally saturates, leading to suppression in κ. The number of phonons involved in U-processes is

given by $[\exp\left(\frac{\hbar\omega}{k_B T}\right) - 1]^{-1} \approx \exp\left(-\frac{\hbar\omega}{k_B T}\right)$, where $\hbar\omega$ is the energy corresponding to phonon wave vector involved in U-process. With the use of parameter $b \equiv {\omega_D}/{\omega}$, where $\omega_D = \frac{k_B \theta_D}{\hbar}$ is Debye frequency as defined above in Eq. (2.16), the number of phonons involved in U-processes is given by, $e^{-\frac{\theta_D}{bT}}$. Since, $C \propto T^3$, and mean free path (l) is inversely proportional to number of phonons involved in U-process, $\kappa \propto T^{\alpha} e^{-\frac{\theta_D}{bT}}$ (as T^3law is only valid up to $\frac{\theta_D}{40}$, T^3can be replaced by T^{α} with α being an empirical constant to account for any deviation from the T^3 law). Therefore, in this region κ decreases sharply with increase in temperature.

In the temperature region ($T \gg \theta_D$), specific heat is constant, i.e., independent of temperature and dominated by Umklapp scattering. Then, inverse proportionality of mean free path with the number of phonons in U-processes leads to, $l \propto e^{\frac{\theta_D}{bT}} \propto \frac{\theta_D}{bT}$. Therefore, from the temperature dependence of κ, (i.e. in reference to Eq.(2.6)) it follows that $\kappa \propto \frac{1}{T}$. The typical temperature dependence of lattice thermal conductivity in non-metal is shown in Figure 2.2.

2.5 CALLAWAY MODEL

If several types of scattering processes act together, then the scattering rate of individual process can be added together to get the total relaxation rate as in Eq. (2.19) (Matthiessen's rule). Including the scattering processes discussed above, we can write Eq. (2.19) as,

$$\tau^{-1} = \tau_{pp}^{-1} + \tau_d^{-1} + \tau_b^{-1} + \cdots, \tag{2.22}$$

where τ_{pp}^{-1} is phonon-phonon, $\tau_d^{-1}$is phonon-defect, and τ_b^{-1} is phonon-boundary relaxation rate. The independence of different scattering mechanisms as assumed by Eq. (2.22) can be applied if one scattering mechanism predominates, and all other mechanisms become irrelevant. In case of phonon-phonon scattering, that assumption may not be true because it involves N-process and U-process with individual scattering rate. As discussed above, N-process is not a resistive process like other scattering mechanisms and hence does not contribute directly as a scattering process to thermal conductivity, but it cannot be ignored because it has a great effect of transferring energies between the different phonon modes and thus preventing large deviations from the equilibrium distribution.

In 1959 Callaway [64] gave a model to analyze the experimental thermal conductivity data with the inclusion of N-process on lattice thermal conductivity. In this model, he assumed that N-processes tend to restore an arbitrary phonon distribution to a drifted phonon distribution with some drift velocity. The relaxation time for such process is τ_N.Thus, Eq. (2.22) as a relaxation rate of combined process can be written as,

$$\tau_C^{-1} = \tau_N^{-1} + \tau_U^{-1} + \tau_d^{-1} + \tau_b^{-1} = \tau_N^{-1} + \tau_R^{-1}, \tag{2.23}$$

where, τ_R^{-1} represents the scattering rate of thermal resistive processes. Based on this combined scattering rate, Callaway expressed thermal conductivity as,

$$\kappa = \kappa_1 + \kappa_2 \tag{2.24}$$

with
$$\kappa_1 = \frac{k_B}{2\pi^2 v}\left(\frac{k_B}{\hbar}\right)^3 T^3 \int_0^{\theta_D/T} \tau_C \frac{x^4 e^x}{[e^x - 1]^2} dx, \tag{2.25}$$

and
$$\kappa_2 = \frac{k_B}{2\pi^2 v}\left(\frac{k_B}{\hbar}\right)^3 T^3 \frac{\left\{\int_0^{\theta_D/T} \left(\frac{\tau_C}{\tau_N}\right) \frac{x^4 e^x}{[e^x - 1]^2} dx\right\}^2}{\int_0^{\theta_D/T} \left(\frac{\tau_C}{\tau_N \tau_R}\right) \frac{x^4 e^x}{[e^x - 1]^2} dx}. \tag{2.26}$$

It is clearly seen that κ_1 has considered all scattering processes and on the same footing and thus underestimates the thermal conductivity, which is restored by the addition of κ_2.

In the case of *dominant resistive process*, i.e., when the impurity level is significant in a crystal and all phonon modes are scattered by the resistive processes then, $\tau_N \gg \tau_R$, which leads to $\tau_C \approx \tau_R$. In such a case, $\kappa_2 \ll \kappa_1$, and lattice thermal conductivity given by Eq. (2.25) is same as given by Eq. (2.16) as though N-processes did not exist. In the opposite extreme of *dominant N-processes*, only scattering mechanism are N-processes and hence $\tau_R \gg \tau_N$ leads to $\tau_C \approx \tau_N$. The denominator of κ_2 in Eq. (2.26) approaches zero leading to infinite thermal conductivity as expected by dominant N-processes because they do not give rise to thermal resistance.

Once the expression for the lattice thermal conductivity is obtained, the problem is to figure out the appropriate relaxation time for different phonon scattering mechanisms. Numerous authors have studied and estimated the relaxation rates which will be summarized below.

For phonon-phonon N-process, the relaxation rate given by,

$$\tau_N^{-1} = A' T^{a'} \omega^a. \tag{2.27}$$

It is a general form obtained form best fit of the experimental thermal conductivity data, where $A'$is a constant, and $a' = 3$ and $a = 1$ was suggested for LiF [65]. In general practice, Eq.(2.27) is not included in the analysis of experimental data.

For phonon-phonon U-process, the relaxation rate as suggested by Peierls [66] can be written as,

$$\tau_U^{-1} \propto T^{\alpha} e^{-\frac{\theta_D}{bT}}, \tag{2.28}$$

with the value of α and b in the order of unity. Typical expression for phonon-phonon U-process is [64],

$$\tau_U^{-1} = BT^3\omega^2 e^{-\frac{\theta_D}{bT}}, \tag{2.29}$$

For the case of phonon- defects scattering, frequency dependence of the relaxation time depends on the size of defects. For scattering by point defects,

$$\tau_d^{-1} = A\omega^4. \tag{2.30}$$

For the case of sheet like (planar) defects, which are mostly relevant in layered structures like in cuprates,

$$\tau_d^{-1} = C\omega^2. \tag{2.31}$$

Relaxation time for the scattering by crystal boundaries at low temperature is directly related to the minimum dimension of the sample,

$$\tau_b^{-1} = \frac{v}{L_b}, \tag{2.32}$$

where v is the average phonon velocity and L_b is the minimum dimension of the crystal.

Therefore, combination of above discussed relaxation rates of different scattering processes with the expressions of thermal conductivity in Eq. (2.16) or Eq. (2.25) will be sufficient to explain the experimental thermal conductivity of most insulators. Depending on the specific necessity regarding particular specimen, relaxation rates of additional scattering processes can be added.

2.6 OTHER CONTRIBUTIONS TO κ

2.6.1 RESONANT PHONON SCATTERING

Various quasiparticles can scatter phonons or be scattered by phonons, thus affecting the thermal conduction in solids. When quasiparticles magnons or spinons

interact with phonons, they can give rise to various spin-lattice relaxation processes, thus suppressing the heat conduction. On the other hand, it is possible to conduct heat by such quasiparticles in an ordered system, especially in low dimensions. The conduction of heat by such magnetic excitations will be discussed later in details. In addition to above mentioned relaxation rates, it is often required to add relaxation rate with resonance like character to explain a dip in the thermal conductivity of solids as suggested by Pohl in 1962 [67]. The generic relaxation rate to account for such resonant scattering of phonons is of the form,

$$\tau_{res}^{-1} = R\frac{\omega^2}{(\omega_0^2 - \omega^2)^2}, \tag{2.33}$$

where ω_0 is resonance frequency and R is the strength of resonant scattering proportional to concentration of resonant defects. Such resonant defects can be non-magnetic defects (for eg. KCl crystal containing small amounts of KNO_2 in Pohl's classic experiment) as well as magnetic defects (eg. Fe^{2+} in $ZnSO_4$ [68]) as in the case of paramagnetic crystals. In case of paramagnetic crystals, the magnetic ions can act as resonant scatters of phonons. For a resonant process, a two or multi-level system is necessary. From a spin point of view, a spin may excite by absorbing a phonon of energy equal to level split $\Delta = \hbar\omega_0$, and later it may relax by emitting a phonon of same energy but uncorrelated in its direction to the previous, in a direct process. In an indirect process, phonons of different energies are being absorbed and emitted. All of these processes give rise to thermal resistance to the heat flow. Resonant phonon scattering corresponding to different crystals studied in this thesis will be discussed in the respective chapters.

2.7 MAGNETIC HEAT TRANSPORT

Although heat transport by magnetic excitations was predicted long time ago in 1936, experimental evidence of such magnetic heat transport appeared only few decades later on ferromagnetic Yttrium-Iron-Garnet (YIG) [5]. Most of those early experiments were restricted to only on ordered phase of the magnets at a very low temperature, thus did not provide the valuable information about magnetic excitations, and scattering on various defects and quasi-particles, similar to that obtained from lattice thermal conductivity. Evidence of magnetic heat conduction above ordering temperature was obtained on one-dimensional AFM compound $KCuF_3$ in 1975 [6]. Theoretical prediction of dissipationless heat transport by 1D-AFM Heisenberg chain [7], [8], and experimental findings of huge magnetic heat transport in spin ladder compound [9]–[11] boosted the research interest in this field. Recently, many such systems are in light, and cuprates are on the forefront in providing a clear evidence of magnetic heat conduction.

In analogy to lattice thermal conductivity, we can derive the magnetic thermal conductivity of one-dimensional spin chain systems in the framework of kinetic theory. Since, systems under study are quasi-one-dimensional only in its magnetic structure (phonon contribution is three-dimensional), no modification in expression of lattice only thermal conductivity is required. Treating spinons as fermions with energy $\varepsilon(k)$, velocity $v(k)$, and mean free path $l(k)$ such that magnetic specific heat, $C_{mag} = \frac{d}{dT}N(k)\varepsilon(k)$ and velocity, $v(k) = \frac{1}{\hbar}\frac{d}{dk}\varepsilon(k)$, we can write expression of magnetic thermal conductivity as,

$$\kappa_{mag} = \frac{N_s}{\pi\hbar}\int \frac{d}{dT}\frac{1}{\left(e^{\frac{\varepsilon(k)}{k_BT}}+1\right)}\varepsilon(k)\frac{d}{dk}\varepsilon(k)l(k)dk, \tag{2.34}$$

where N_s is the number of spin chain per unit area. In the limit of $k_BT \gg J$, heat carrying excitations exist only near band minima so that we can write $l(k) \equiv l_{mag}$. Substituting $x = \frac{\varepsilon(k)}{k_BT}$ in Eq. (2.34) for spin ½ Heisenberg chain, we get [5],

$$\kappa_{mag} = \frac{2N_s k_B^2}{\pi\hbar} l_{mag} T \int_{\mathbf{0}}^{J\pi/2k_BT} \frac{x^2 e^x}{[e^x+1]^2} dx. \tag{2.35}$$

At low temperature limit, this integral is only weakly temperature dependent and at $T \to 0$, it gives $\frac{\pi^2}{6}$. Thus, low temperature estimate of magnetic thermal conductivity is,

$$\kappa_{mag}(T) = \frac{\pi N_s k_B^2 T}{3\hbar} l_{mag}(T), \tag{2.36}$$

which can be used to estimate the mean free path of magnetic excitation if κ_{mag} is known. Similarly, κ_{mag} expression for gapped two leg ladders can be derived [5],

$$\kappa_{mag} = \frac{3N_s k_B^2}{\pi\hbar} l_{mag} T \int_{\Delta/k_BT}^{\infty} \frac{x^2 e^x}{[e^x+3]^2} dx, \tag{2.37}$$

where N_s is the number of spin ladders per unit area. At low-T limit of $k_BT \ll \Delta < J$, integral can be approximated as $\exp\left(-\Delta/k_BT\right)$. In this case, the distribution function is not a Bose distribution function and such form of distribution function is used to account for local triplet excitation exactly. More details on the use of such distribution function can be found on ref.[11]. Alternately, Bose distribution function has also been used to describe magnetic thermal conductivity of two leg ladder system as [10],

$$\kappa_{mag} = \frac{N_s {k_B}^2}{\pi\hbar} l_{mag} T \int_{\frac{\Delta}{k_BT}}^{\frac{\varepsilon_{max}}{k_BT}} \frac{x^2 e^x}{[e^x-1]^2} dx\,, \tag{2.38}$$

where $\frac{\Delta}{k_BT} = x_0$ & Δ is a spin gap, and $\frac{\varepsilon_{max}}{k_BT} = x_{max}$ & ε_{max} is the maximum band energy of magnetic dispersion.

CHAPTER III

EXPERIMENTAL DETAILS

In this chapter, I will describe the experimental procedures and techniques involved in the preparation of samples and various measurements. We used X'pert x-ray diffractometer for the orientation of single crystals, determination of lattice parameters and study of twinning behavior. Steady state-method was employed for thermal conductivity measurements. Sample preparations, measurement techniques, calibrations, radiation loss corrections will also be discussed in some details.

3.1 LATTICE PARAMETER AND ORIENTATION BY XRD

3.1.1 BASICS OF X-RAY AND GONIOMETER DESCRIPTION

X-rays are reflected, refracted, scattered, absorbed, and transmitted when they interact with the matter. At specific angle of incidence, incident x-ray radiation is scattered coherently by atoms in a crystal thus forming constructive interference. At most of the other angle of incidences, scattered radiation forms a destructive interference as they are out of phase with each other. The strong peak of intensity that is produced by the coherent scattering of the atomic arrangement in a crystal is called the Bragg diffraction peak. Thus, by knowing the angle at which Bragg diffraction peak occurs, we can possibly get information about the arrangements of atoms in a crystal. Bragg equation (Eq. 3.1) gives a simple relationship which states the condition to obtain such diffraction peaks.

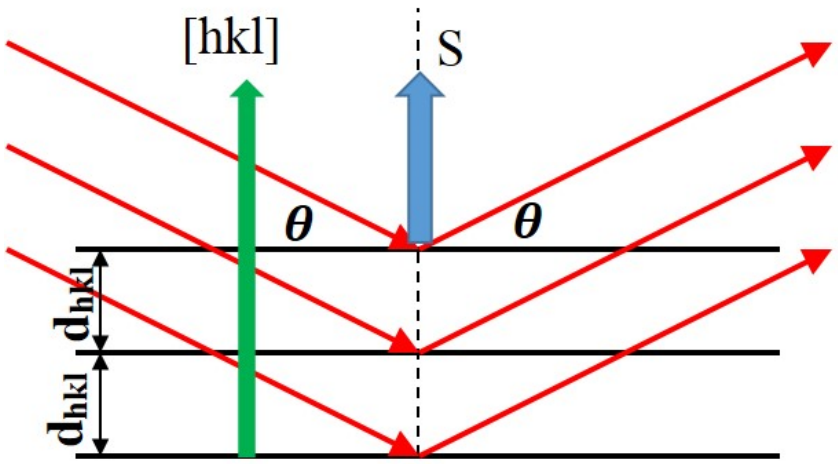

Figure 3.1 Schematics of Bragg diffraction condition. $[hkl]$ is a plane normal and S is a diffraction vector.

$$2d_{hkl}\, sin\theta_n = n\lambda \tag{3.1}$$

Where, λ is a wavelength of incident radiation, θ is an angle of incidence, and n is an order of diffraction. Thus, for a set of parallel planes of atoms separated by distance d_{hkl} , the constructive interference is possible only when the Bragg's condition is satisfied. In addition, the plane normal $[hkl]$ must be parallel to diffraction vector (S) as shown in Figure 3.1.

Figure 3.2 shows the Bragg-Brentano parafocousing geometry used by our instrument (Phillips *X'*pert Diffractometer) during XRD (x-ray diffraction) measurements. In this geometry, crystal will be at the center of the detector circle, as well as at the circumference of focusing circle at the same time, and x-ray source and detector move in such a way that they are always at the intersection of circumference of focusing circle and detector circle (or goniometer circle). This geometry helps to increase the intensity and the angular resolution. Goniometer consists of three main components as shown in Figure 3.2 , *X-ray source*, *Sample stage* and *Detector*. More detailed description of these three components can be found in [69]. Our x-ray source is Cu $K_{\alpha 1}$ line with $\lambda = 1.540456$ Å

but it also contains $K_{\alpha 2}$ because our instrument is not equipped with monochromator, however, β filter (Ni-filter) removes K_{β} on the speectrum. Point focus optics was used for XRD of single crystals in this study. Sample stage is a flat disc which can move in three ways giving three angular rotations ϕ, ω and ψ as shown in Figure 3.2. Detector is a Xe-filled proportional counter capable of rotating about 140° in such a way that it always makes an angle 2θ with respect to plane of incident x-ray direction, where θ is the angle made by incident x-ray and reflecting planes of a crystal. Figure 3.3 shows the Phillips *X*'pert diffractometer used in this study.

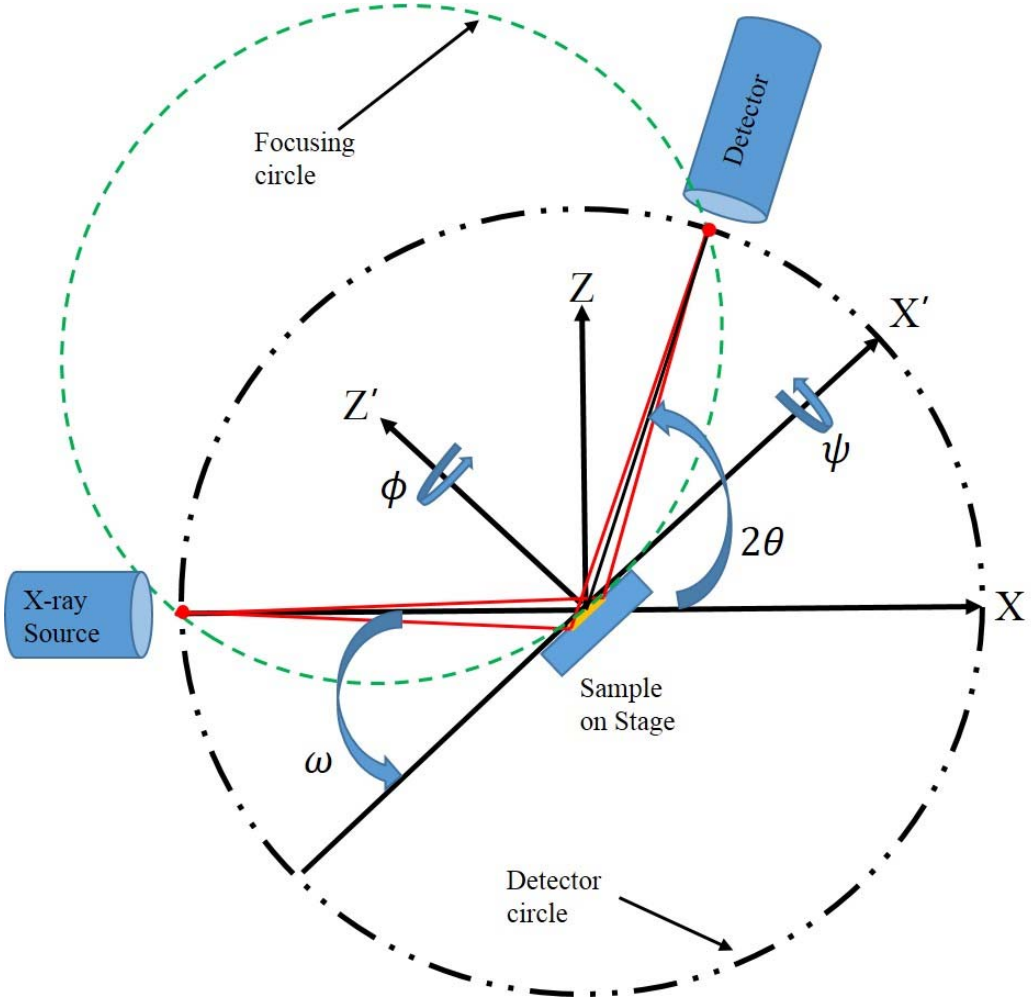

Figure 3.2 Schematics of Bragg-Brentano Parafocusing geometry. X-ray emergent point and focusing point (two red dots) are always on the intersection of both focusing circle and detector circle (also called goniometer circle).

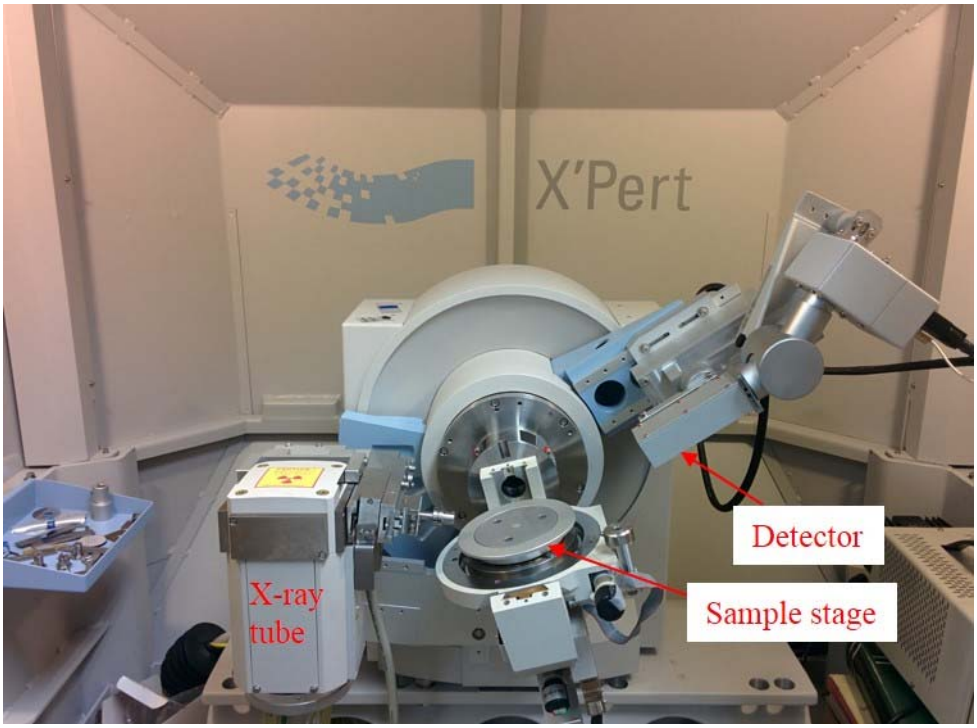

Figure 3.3 Phillips *X'*pert diffractometer used in this study.

3.1.2 TYPES OF SCAN

Among the various possible scans using x-ray diffractometer, we will discuss in brief the types of scans that we have used more commonly.

Rocking curve or ω-scan gives the plot of x-ray intensity vs omega. During the scan, detector is fixed at specific Bragg angle corresponding to reflecting plane and sample is tilted such that ω varies. Rocking curve provides the information about the spread of orientation of crystallites. Ideally, a perfect crystal should produce a very sharp rocking curve because all the plane normal are exactly parallel to diffraction vector, but various defects contribute to broadening of curve. Therefore, rocking curve is an important tool to check the quality of a single crystal.

Coupled scan or 2θ*- ω scan* gives the plot of x-ray intensity vs 2θ, with change in ω in such a way that $\omega = \frac{1}{2} \times 2\theta$ +offset, where offset can be both positive and negative.

During this scan, as sample is rotated about ω, detector moves twice the rate keeping the offset constant (if any). This scan provides the all possible reflections from the planes that are parallel to the intended (hkl) plane. Thus, Bragg diffraction angle can be measured and used to determine the lattice parameters of the crystal. Several factors, like imperfection of crystal and imperfect monochromaticity of the x-ray etc, are responsible for the finite width of 2θ- ω peaks.

Phi (ϕ) *scan* gives the plot of x-ray intensity vs ϕ which enables us to determine the relative orientations of crystallographic planes and hence, the orientation of a single crystal. During this scan, ω and 2θ angles are fixed for the intended (hkl) plane, and the sample stage (i.e., crystal) is rotated by 360° about *z*-axis as shown in Figure 3.2.

Psi (ψ) $scan$ gives the plot of x-ray intensity vs ψ, which enables us to set the desired plane for diffraction and then to optimize the intensity from that plane. During this scan, sample stage can be moved from -4.5° to 89.5° about *x*-axis as shown in Figure 3.2.

Pole figure scan is a two dimensional scan and gives 3D plot of x-ray intensity vs ϕ and ψ, at fixed 2θ and ω. It can be plotted in various forms like contour plot, mesh plot, pole figure plot etc to get the desired information. We have plotted the data from pole figure scan in 3D-mesh plot, to see the relative intensity of twins or other domains in a single crystal at once. During pole figure scan, ϕ varies from 0° to 360° for each ψ varying from -4.5° to 89.5° in certain step size such that 2θ and ω remain fixed for the particular set of plane.

3.1.3 DETERMINATION OF LATTICE PARAMETER

For all the single crystals we have studied, lattice parameter and crystal structure were already available in the literature, however, we have calculated the lattice constants

of the single crystals we have measured to assure the consistency. First of all, using literature values of lattice parameters and crystal symmetry in Crystallographica[1], we obtained expected values of 2θ for various possible miller planes (hkl). Then, various set of planes (hkl) corresponding to 2θ are optimized using XRD and new values of 2θ are recorded. We have then used the Bragg law to determine d and calculated the lattice parameter a from the plane spacing relations [70] corresponding to crystal structure of specific crystal. Because of use of $sine$ in Bragg law, accuracy of lattice parameter a depends on $sine$ function instead of θ, which eventually leads to a high angle extrapolation technique [70] where lattice parameter a is in linear relation with a function of θ as,

$$a = a_0 + a_0 K \left(\frac{\cos^2 \theta}{\sin \theta} + \frac{\cos^2 \theta}{\theta} \right), \tag{3.2}$$

where a_0 is the true value of the lattice parameter a which can be obtained by extrapolating this line to $\left(\frac{\cos^2 \theta}{\sin \theta} + \frac{\cos^2 \theta}{\theta} \right) = 0$ (see Figure 4.2), and K is a constant. It is important to note that closer the value of 2θ to 180°, more precise will be the lattice parameter, thus giving the name high angle extrapolation.

3.2 CRYSTAL ORIENTATION

Single crystals which are not oriented in a particular direction or possessing unfavorable surface orientation can be oriented or realigned to virtually any crystallographic directions [hkl]. Orienting a single crystal in a particular direction is essential to determine the physical properties of these crystals in the selected crystallographic directions. While many of the crystals we have used for measurements

[1] A software toolkit for Crystallography from Oxford Cryosystems.

were already oriented by our collaborators with the LAUE film camera, some of the crystals were unoriented and thus required the orientation. Even the oriented ones were cut or polished into smaller and regular shaped ones for the measurements. We used X'pert x-ray diffraction in association with the home designed polishing tool (see Figure 3.4) and the wire saw[2] to produce reoriented surface or crystal direction.

Initially, an unoriented crystal is mounted on one of the flat facet, and x-rayed to identify that flat facet and its relation to one of the crystallographic directions. We used calculated 2theta values and corresponding miller planes from Crystallographica to identify the crystal planes. Crystal is then either polished or cut by the wire saw to get a surface parallel to one of the crystallographic directions as identified by XRD, in reference to the originally mounted flat facet of the crystal. The resulted crystal specimen is then re-x-rayed to confirm the identification of one of the crystallographic directions, and the process is repeated if the crystal is not oriented properly. Same procedure is repeated for other crystallographic directions (if required) in reference to newly identified orientation. At the end, most of the time, regular shaped crystal is obtained as shown in Figure 3.4(e), which is further x-rayed to verify the lattice parameter, crystalline quality, and to check for various defects. Finally, a regular shaped, defects free crystal is mounted for measurements.

[2] South Bay Technology model 750 with Boron Carbide solution instead of acid

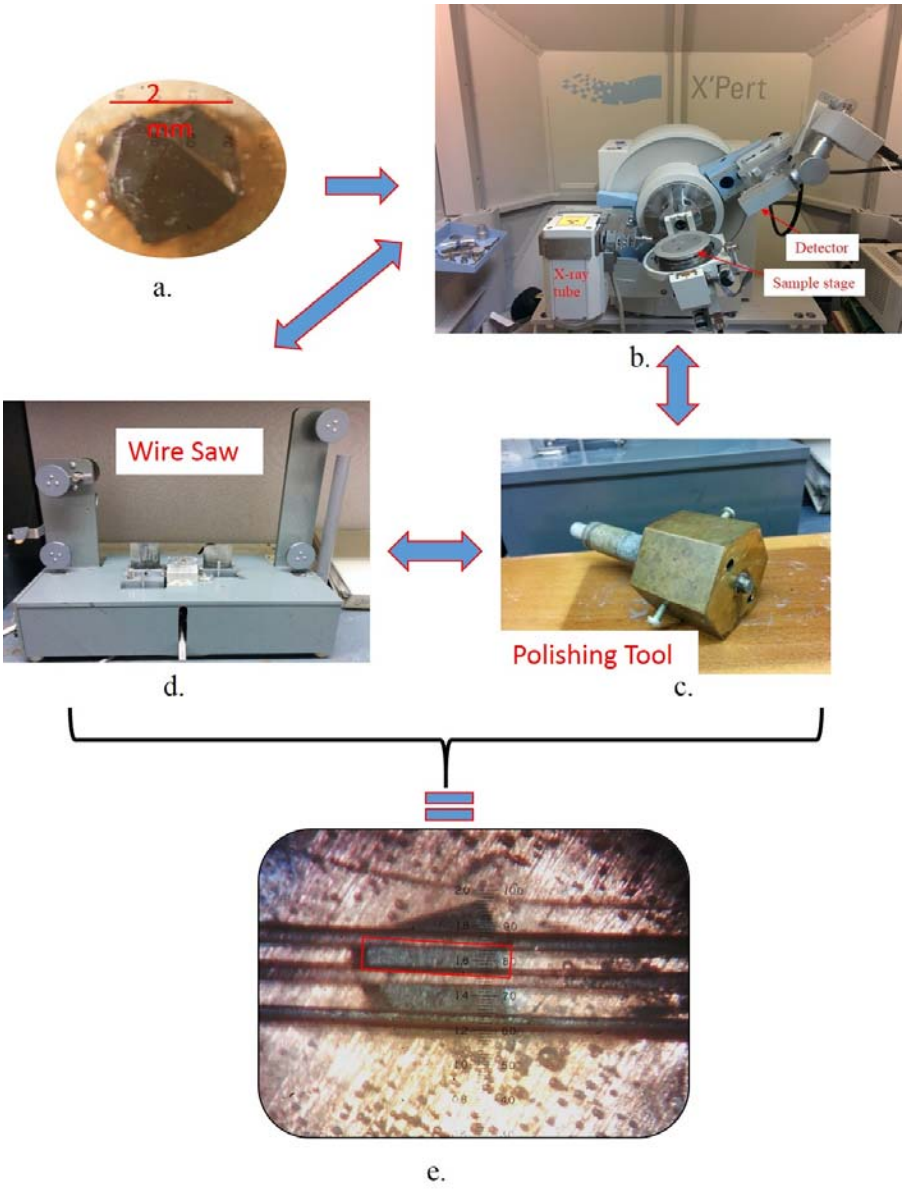

Figure 3.4 Procedure involved on orienting single crystals; a) an unoriented single crystal b) XRD used c) polishing tool used to polish crystal faces d) wire saw used to cut crystal e) resulted rectangular shaped crystal oriented in selected crystallographic direction.

3.3 THERMAL CONDUCTIVITY $\kappa(T)$ MEASUREMENTS

3.3.1 MEASUREMENT PRINCIPLE

Thermal conductivity measurement is based on one dimensional form of Eq. (2.1),

$$j = -\kappa(\nabla T)_x, \tag{3.3}$$

where j describes the thermal current density along a temperature gradient, $(\nabla T)_x$, in x-direction in a steady state situation. Steady state situation is obtained when a uniform temperature gradient throughout the measured specimen is achieved. This leads to an experimental setup as shown in Figure 3.5. One end of a crystal specimen to be measured is attached to the copper tab (heat sink) by a glue (Stycast 2850[3]) and a small chip heater[4] is attached to the other end. Temperature gradient across a sample is achieved by passing a current I to an attached heater and monitored by a Chromel-Constantan (Type-E) differential thermocouple[5] of diameter $0.001"$ positioned across the length L of the sample. Thermocouple gives a voltage[6] corresponding to a temperature difference which is finally

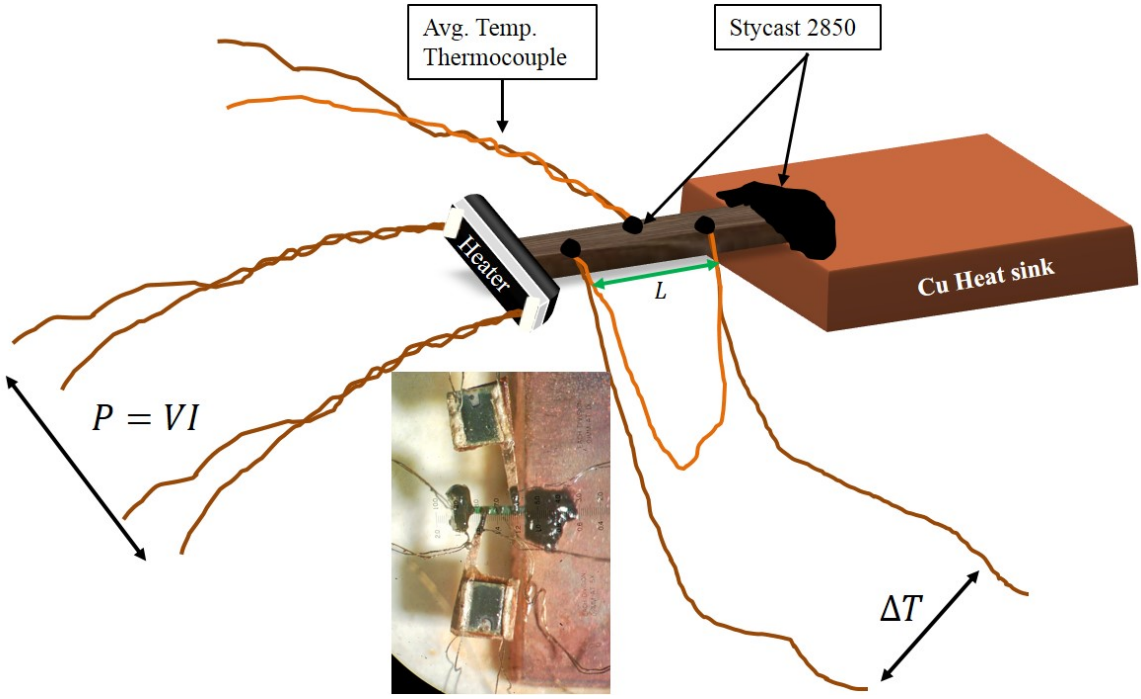

Figure 3.5 Experimental setup for steady state method of thermal conductivity measurement. Small inset in the bottom left shows the real experimental setup with Ruthenium oxide thermometers glued to crystal in addition to thermocouples.

[3] STYCAST 2850FT black by Emerson & Cuming. Often GE-Varnish also used for mounting.
[4] Thick film 1KOhm resistor from Newark.com
[5] California fine Wire Company, Grover Beach, CA.
[6] Voltage measured by KEITHLEY 182 sensitive digital nano-voltmeter.

converted to a temperature using the calibration data of that thermocouple. To eliminate the effect of background temperature gradient, ΔT is measured in both heater OFF and ON position and the effective temperature difference ΔT_{ON-OFF} is obtained by subtraction as shown in Figure 3.6. At the steady state condition, all the energy provided by a heater is assumed to flow through the sample, and the thermal current density is,

$$j = \frac{P}{A} = \frac{VI}{A}, \tag{3.4}$$

where V is voltage measured across the heater and A is the cross section area of the sample. Also, thermal gradient across the sample is uniform and given by $(\nabla T)_x = \frac{\Delta T_{ON-OFF}}{L}$. Combining Eq. (3.3) and Eq. (3.4), we can write,

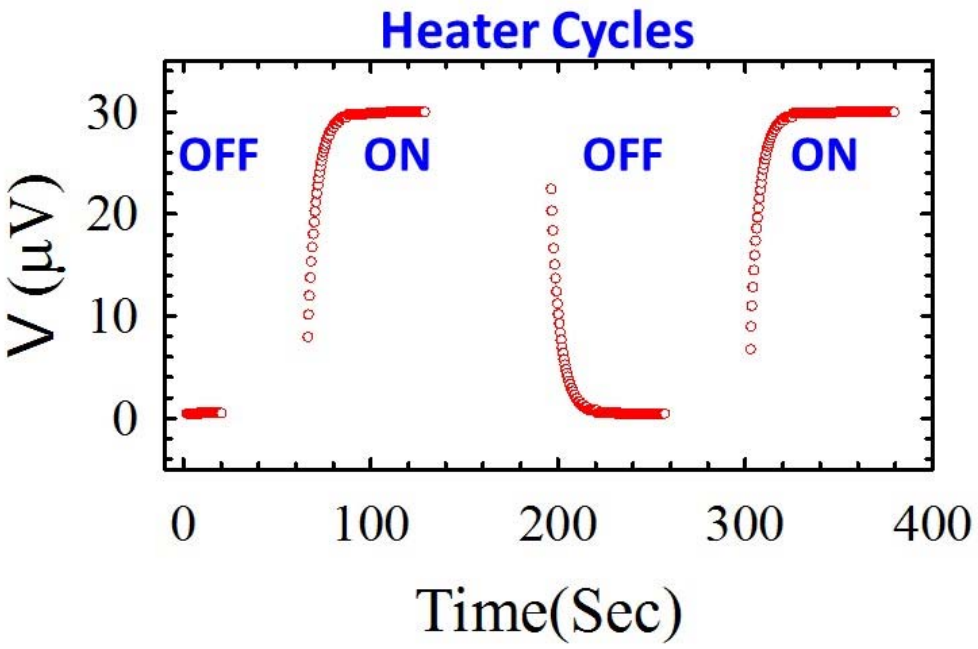

Figure 3.6 Heater cycle during κ measurement. Temperature gradient ΔT is measured during both heater OFF and ON condition to get effective temperature gradient, ΔT_{ON-OFF}. Each data point is taken twice by repeating such heater cycle for accuracy.

$$\kappa = \frac{VI}{A}\frac{L}{\Delta T_{ON-OFF}}. \tag{3.5}$$

Therefore, by measuring the heater power and the corresponding effective temperature gradient across the length L, we can calculate thermal conductivity (κ) as shown by Eq.(3.5). The average thermocouple is used to measure the temperature of sample with respect to stage temperature, thus average temperature of the sample is given by $T_{Avg}(i) = T_{stage} + \frac{\mathrm{V}_{avg}}{S_{Avg}(i-1)}$, where S_{Avg} is thermopower of average thermocouple and i is number of iteration.

3.3.2 EXPERIMENTAL DETAILS

3.3.2.1 INSTRUMENTS

Different types of probes are used for κ measurements depending on the range of temperature. ^{3}He probe[7] for temperature range of $0.5K \leq T \leq 20K$, Low-T ^{4}He probe for $5K \leq T \leq 300K$, and High-T probe for $300 \leq T \leq 500K$ are used during the experiment. Main purpose of the probe during κ measurement is to provide persistent vacuum space for sample as well as to maintain balanced thermal link between the sample space and thermal bath outside the probe (cryogen or cold air) so that temperature of the sample space can be tuned throughout the range. Sample space is maintained at vacuum of $P \approx 5 \times 10^{-5} Torr$ by continuously pumping in that space with the combination of a mechanical pump and a diffusion pump[8]. Basics of sample stage of each probe will be described below.

For the temperature range of $0.5K \leq T \leq 20K$, ^{3}He probe with optimized sample stage was used. Working principle of ^{3}He system can be found elsewhere[71]–[74].

[7] Cryo Industries of America
[8] Edward's two stage mechanical pump and high vacuum oil diffusion pump

Temperature of the sample stage was monitored[9] by industry calibrated Ruthenium oxide[10] (RuO) thermometer with calibration range of $0.05\ K$ to $20\ K$. We have used self-calibrated (w.r.t. industry calibrated RuO) bare chip ruthenium oxide thermometer (RX-BR)[11] in addition of thermocouples as shown in the inset of Figure 3.5. It is done by gluing RX-BR thermometer in one end of thin foil of copper or gold wire and other end is attached to the crystal together with a thermocouple. It allows us to monitor temperature gradient throughout the temperature range of interest. Resistances of RX-BR thermometers are obtained by passing $(0.5-1)\mu A$ current from programmable current source[12] and measuring corresponding voltage simultaneously. Resistances thus obtained are converted to corresponding temperatures using calibration table by a computer program. Scanners[13] are used to control the switching between the channels allowing the continuous measurements without manual interruption. Although this probe can be used for κ measurement all the way up to room temperature, we have used this probe only in the required condition of getting below $4\ K$ because of complexity in its setup and cryogenic consumption.

For the temperature range of $4.2K \leq T \leq 300K$, ^{4}He probe was used most of the time, which can be inserted directly into a cryogen storage Dewar. Schematic of sample stage of this probe is shown in Figure 3.7(a). Stage temperature was monitored by platinum (above $30\ K$) and germanium (below $30\ K$) thermometers[14]. Resistive wire is wrapped around the copper base which functions as a heater to control the temperature of stage in

[9] Using Lakeshore temperature controller model 335, 331 and DRC-91CA.
[10] Scientific Instruments model no. RO600A.
[11] Lakeshore Cryotronics.
[12] KEITHLEY 224 programmable current source.
[13] KEITHLEY 705 and 7001 scanners
[14] Lakeshore Cryotronics PT and GR

combination with a small current output provided by temperature controller, and the current is adjusted based on feedback provided by the PID parameters. Small soldering pads at the top of the copper block serve as the connecting pads for various wire connections. Radiation shield covers the sample space to minimize the heat loss. Finally, the whole sample stage is screwed into the main probe and the wires from various connections (thermometers, heater, thermocouples etc.) are connected to the main probe wires using several of those ten pin connector. These wires are ultimately taken out of the probe via 19 pin connectors (not shown) to connect to various electronic devices.

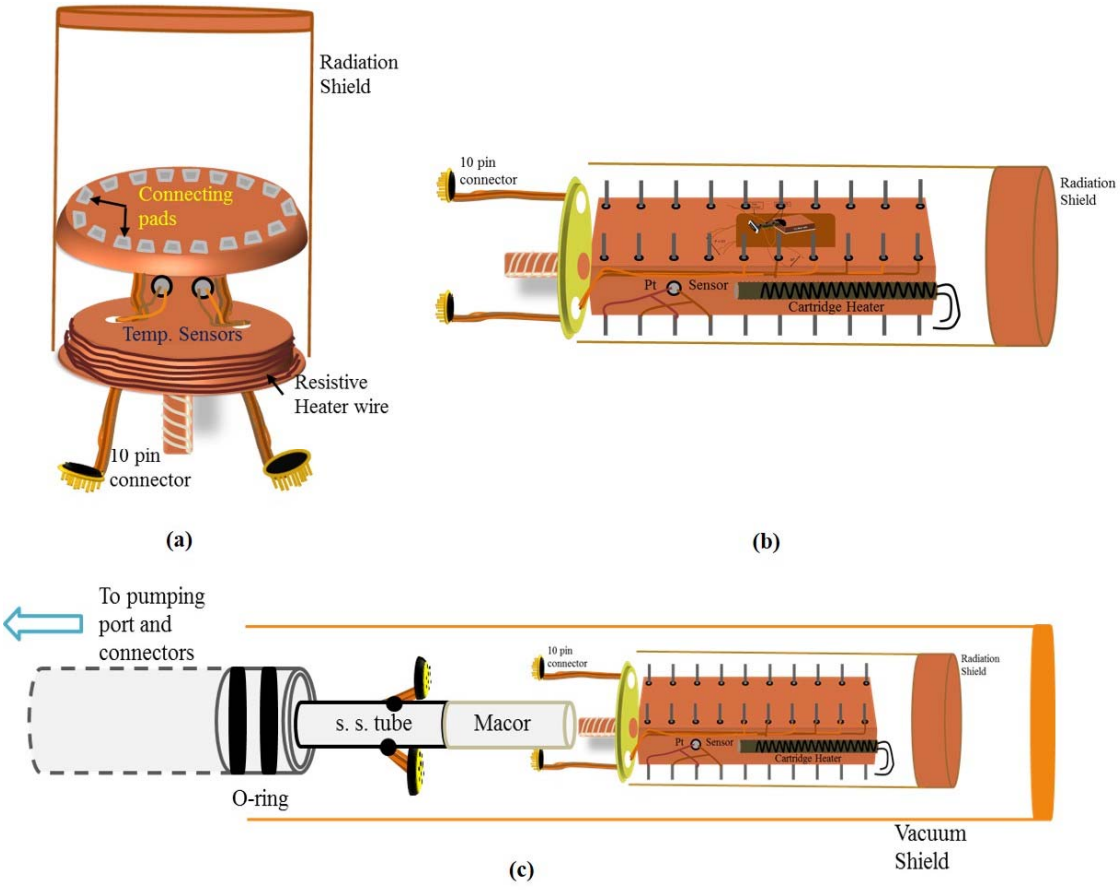

Figure 3.7 Different sample stages used in κ measurements (a) ^{4}He probe stage (b) High-T probe stage, and (c) Assembly of High-T stage to the main probe using MACOR as a bridge.

For the temperature range of $300K \leq T \leq 500K$, probe with home built detachable stage was used. Main requirement for this probe was to minimize the thermal link between the sample stage and probe wires because of temperature ratings of the connectors and insulations. Several materials (thin walled stainless steel tube with baffles, machinable ceramics clay etc.) were tested but temperature was above the ratings. Finally, a machinable glass ceramics MACOR[15] served the purpose. Temperature of the probe near the other end of MACOR remains around $373\ K$ while temperature of the stage is above $500\ K$. Schematics of detachable stage with radiation shield is shown in Figure 3.7(b & c). It was not possible to solder wires on stage because of higher temperature on stage, thus the stainless steel posts are anchored in the copper block holes with an adhesive[16] in such a way that they remain insulated from but in thermal contact to, the copper block. All the wires are spark welded into those stainless steel posts. A cartridge heater[17] is inserted into a hole at the center of copper block and potted with sensor and heater cement[18], and its temperature is monitored by platinum sensor put next to the heater end as shown in Figure 3.7(b). All the wires are taken out of the stage through the holes in the baffle and connected to ten pin male connectors which connect with female connectors coming out from other end of the probe. Radiation shield (inner cylinder) minimizes heat loss and outer cylinder encompasses the vacuum space in combination with O-rings.

3.3.2.2 MEASUREMENTS IN A MAGNETIC FIELD

Magnetic field dependence of κ is measured in a magnetic field of up to $9\ T$. ^{3}He probe has an attached superconducting magnet of $5\ T$ enclosing the sample space. It is

[15] Designed and sold by Corning Inc.
[16] RESBOND 907,Cotronics Corporation
[17] Cryo-con
[18] Oxford Instruments

operated using Lakeshore model 625 superconducting magnet power supply. It has bipolar power supply functionality which makes easier to reverse the field during the measurement. Self-calibrated RX-BR chip resistors are used to measure the temperature gradient in a field because of their low mag.field dependence ($\sim 6\%$). In the need of higher magnetic field, separate superconducting magnet[19] with variable temperature sample insert is used to get the field of up to $9\ T$. A ^{4}He probe is inserted into the variable temperature sample insert for the thermal conductivity measurements.

3.3.2.3 DATA ACQUISITON

The data acquisition program is designed in LabVIEW[20] and measurements are fully automated. Computer controls and communicates with various instruments through GPIB (General Purpose Interface Bus) cards. We employ standard procedure for data taking as described below. All the subVIs (subroutines) corresponding to each instrument contain initialization routine that ensure the proper communication with the instrument, put up optimal parameters for that particular experiment and create output files for data storage. Temperature stabilization subroutine sets up the temperature, reads it continuously and plots as a function of time. The slope of that plot along with temperature setpoint is used to compare with the given slope constraint (input parameter) to determine the stability of the temperature. Once the stability is achieved, the sequence is repeated after 2 min delay to check the drift in temperature if any. If the drift in temperature is more than allowed limit, it repeats the sequence again otherwise proceeds to data acquisition subroutine. During data acquisition, uniform temperature gradient on the sample is

[19] JANIS Research Company Inc.
[20] Graphical programing language from National Instruments

achieved by monitoring thermocouple voltage as a function of time and using slope constraint to determine the uniformity of gradient (similar to temperature stabilization). Each voltage is read multiple times by nanovoltmeter and averaged out for accuracy. Data are taken during both heater OFF and ON condition to get the absolute values. This data acquisition process is repeated twice by executing heater cycle twice to assure the reproducibility of the data. At the end, calculated final quantity is recorded in file and plotted in the graph and the whole sequence is repeated for next setpoint.

3.3.3 CALIBRATION OF THERMOCOUPLES AND SENSORS

All the thermocouples and sensors used in the measurement are either factory calibrated or calibrated in the lab against a standard one. Most common thermocouple we use is type-E (Chromel-Constantan) thermocouple. High voltage output of type-E thermocouple makes it more common in the labs. These are made in the lab by spark welding 0.001" Chromel and Constantan wires. It can be differential (two junction) and average (single junction) thermocouple. Differential one measures the temperature difference between two points (on sample) while average thermocouple measures the drift in the temperature of sample with respect to stage (which is later used to calculate the average temperature of the sample). Thermopower of each of the wire is measured in the working temperature range of thermocouple and fitted with higher order polynomials as a function of temperature. Coefficients from the fit are used in the computer program to calculate the temperature corresponding to measured thermocouple voltage.

Bare chip ruthenium oxide thermometers are used in $0.3\ K$ to $20\ K$ range with and without magnetic field instead of thermocouples. These thermometers are calibrated in our lab against the factory calibrated $RO600A$ ruthenium oxide thermometer with and without

magnetic field. Several of these thermometers connected in series are kept in the stage, and voltage corresponding to each is measured simultaneously in both forward and reverse current. Temperature dependence of resistance thus obtained is later used to calculate temperature. Similarly, magnetic field dependence of these thermometer is calculated, which is below 6% at 5 T. Therefore, RuO thermometer are recommended in magnetic field.

3.3.4 ERROR IN THERMAL CONDUCTIVITY

Several factors should be taken into considerations for the correction of errors in thermal conductivity measurement. Geometry of the sample, heat loss and systematic errors in the instruments are the major sources of error in measurements. Instruments used in the measurements are standard instruments and error introduced by them are less than 1%. Voltages are measured by nanovoltmeter, data are averaged for multiple readings, temperature is precisely controlled by temperature controller and a program assures no drift in temperature. Switching between the channels is performed by a millisecond switch system, and current to the heater is controlled by programmable precision current source. Therefore, overall error from the instruments is negligible compared from geometrical factor and heat loss, and can be safely ignored.

Cross-sectional area of the sample and length between two junctions of differential thermocouple on the sample constitutes the geometrical factor. Because of uncertainty in the measurement of length, width and thickness of the sample, error in magnitude of thermal conductivity by geometrical factor is about 15% for regular shaped crystals and up to 30% for irregular shaped crystal. We use StereoZoom® 7 microscope (with zoom up to 7x) with scale on eye piece such that least count of the instrument is 29μm. The typical

size of spot of adhesive to attach a junction of thermocouple to a sample is $\sim 90\ \mu m$. Thus, uncertainty related to distance between thermocouple junctions on the sample can be significant for smaller samples. Thus, depending on the size and shape of the crystals uncertainty can range between 5% and 30%. This uncertainty is temperature independent and does not influence the temperature dependence of $\kappa(T)$, but shifts its magnitude by certain factor.

Ideally, all the heat provided by the heater should pass through the crystal, but in real world some portion of that heat is lost to the surrounding by radiation, by conduction through the wires, and by convection. Although unavoidable, preventive measures are taken to minimize the heat loss such as: a radiation shield to minimize radiation loss, use of long resistive wires to minimize conductive loss, and continuous pumping to maintain vacuum ($10^{-5}\ Torr$) to the sample space (to minimize convection loss). Depending on the probe configurations and dimensions of the sample, uncertainty by heat loss can be 15% to 30% at room temperature. Because of temperature dependence of this error, it is essential to get estimate of this error for the correct description of the temperature dependence of $\kappa(T)$. It can be done by using Stefan-Boltzmann law such that radiation loss between the sample and surrounding is given by,

$$P_{radloss} = \varepsilon \sigma_{SB} A (T_1^4 - T_2^4), \tag{3.6}$$

where ε is the emissivity of the surface ($0 < \varepsilon < 1$), $\sigma_{SB} = 5.67 \times 10^{-8} \mathrm{W/m^2K^4}$ is the Stefan-Boltzmann constant, A is the cross sectional area, and T_1 and T_2 are temperature of sample and surroundings respectively. With $\Delta T = T_1 - T_2$ being small, above relation can be expressed as

$$P_{radloss} = \varepsilon \sigma_{SB} A T^3 \Delta T. \quad (3.7)$$

Because of T^3 dependence of radiation loss, it is much higher at room temperature and above, and becomes negligible at low temperature.

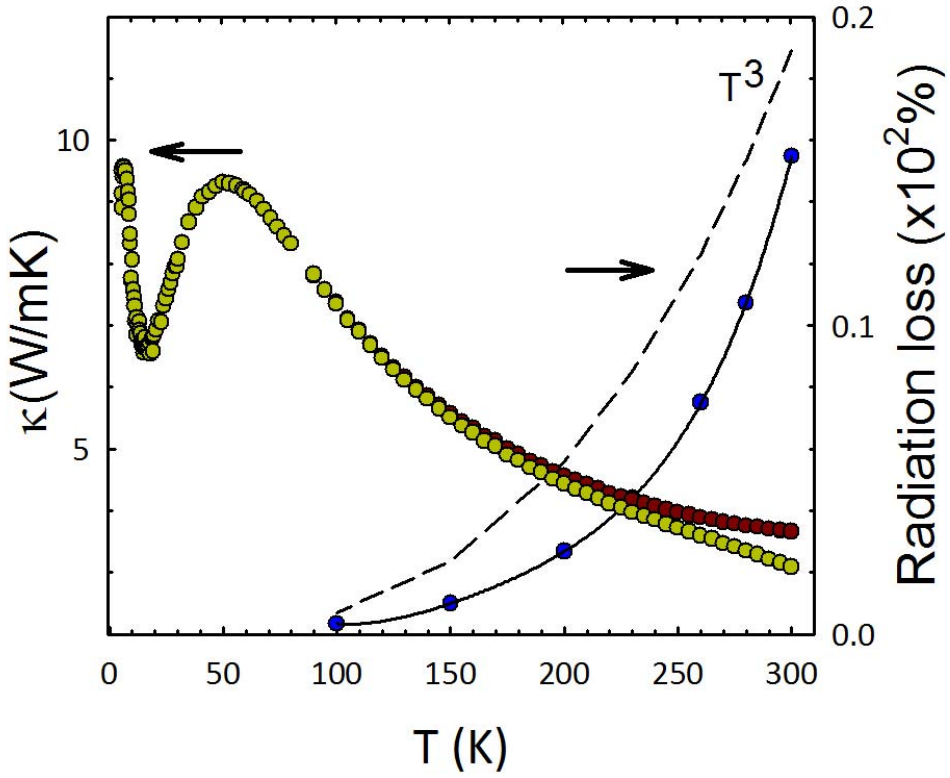

Figure 3.8 Right ordinate shows the radiation loss in percentage (data points are actual measured value and solid line is polynomial fit to data, coefficients from fit are later used to correct thermal conductivity data). Dashed line is T^3 line for comparison. Left ordinate shows the uncorrected (higher magnitude) and corrected (lower magnitude) thermal conductivity of $BiCu_2PO_6$ crystal.

Heat loss can actually be measured and be used to correct thermal conductivity data for heat loss. This was done by disconnecting the sample from the heat sink and set the measurement as during $\kappa(T)$ measurement. For the fixed temperatures (T_{stage}) at which $\kappa(T)$ has already been measured, heater power is adjusted by trial and error until the average temperature of the sample w.r.t. T_{stage} is raised by the same magnitude as during the $\kappa(T)$

measurement. The heater power required to do this is the total heat lost (through convection, conduction and radiation).

Therefore, after heat loss correction, overall error in the thermal conductivity data is about 10%-20% scaling factor, mostly because of geometry of the sample.

CHAPTER IV

SPIN-½ CHAIN COMPOUND $CuSb_2O_6$

In this chapter I will first discuss the motivation regarding the study of thermal conductivity $\kappa(T)$ of $CuSb_2O_6$. Next, its crystal structure and magnetism will be discussed to elucidate the possible role of a lattice and a magnetic structure in heat transport. Effect of bicrystallinity and twinning associated to the structural change of this compound in $\kappa(T)$ will also be described. Then, I will present thermal conductivity $\kappa(T)$ measurements on the single crystals of $CuSb_2O_6$ in three principle crystallographic directions as well as along spin chain [110] directions. Thermal conductivity $\kappa(T)$ of its non-magnetic analog $ZnSb_2O_6$ along [100] will be compared. At the end, analysis of result, i.e., phonon-spin scattering and possible magnetic contribution to heat transport will be discussed.

4.1 MOTIVATION

Low-dimensional quantum spin systems have attracted considerable interest in recent years for their role in the development of many-body theory [75] and for experimental observations of substantial heat conduction associated with spin excitations [5], [12]. As stated in the preface, most thermal conductivity investigations have focused on quasi-one-dimensional (Q1D) spin-½ chain system with exchange energies much greater than the Debye temperature ($J \gg \theta_D$) [5], [12], and not such studies are found on the quasi-one-dimensional (Q1D) spin-½ chain system with exchange energies comparable or smaller than the Debye temperature ($J \leq \theta_D$). Potentially more complex spin-phonon

coupling and lack of thermal conductivity study in this low-J regime motivates for the study of Q1D spin-½ chain compound $CuSb_2O_6$.

Thermal conductivity of $CuSb_2O_6$ which has exchange energy, $J \approx 90 - 100\ K$, is presented and compared it with its non-magmatic analog $ZnSb_2O_6$. Most of the contents of this chapter are from the already published work [76]. The study shows that $CuSb_2O_6$ exhibits strong phonon-spin scattering at one hand, and an additional contribution to κ along the spin chains at $T \leq 150\ K$ attributable to spin heat conduction on the other hand.

4.2 GROWTH, STRUCTURE AND MAGNETISM

Single-crystals $CuSb_2O_6$ and $ZnSb_2O_6$ used in this work are grown by our collaborator at Montana State University. I will describe the growth process briefly to give a picture of procedure involved [77]. Powder for the growth of $CuSb_2O_6$ single crystals was prepared by solid-state reaction of CuO (99.995%) and Sb_2O_3 (99.999%). Stoichiometric amounts of each were mixed and ground with a mortar and pestle. The mixed powder was placed in an alumina crucible and fired in air at 950℃ for 12 hours. The fired powder was reground, pressed into pellets, and fired in air at 1000℃ for 45 hours, reground, pressed into pellets and then annealed at 1000℃ for 24 hours followed by slow-cooling to room temperature. X-ray powder diffraction of a crushed pellet showed only the monoclinic unit cell of $CuSb_2O_6$.

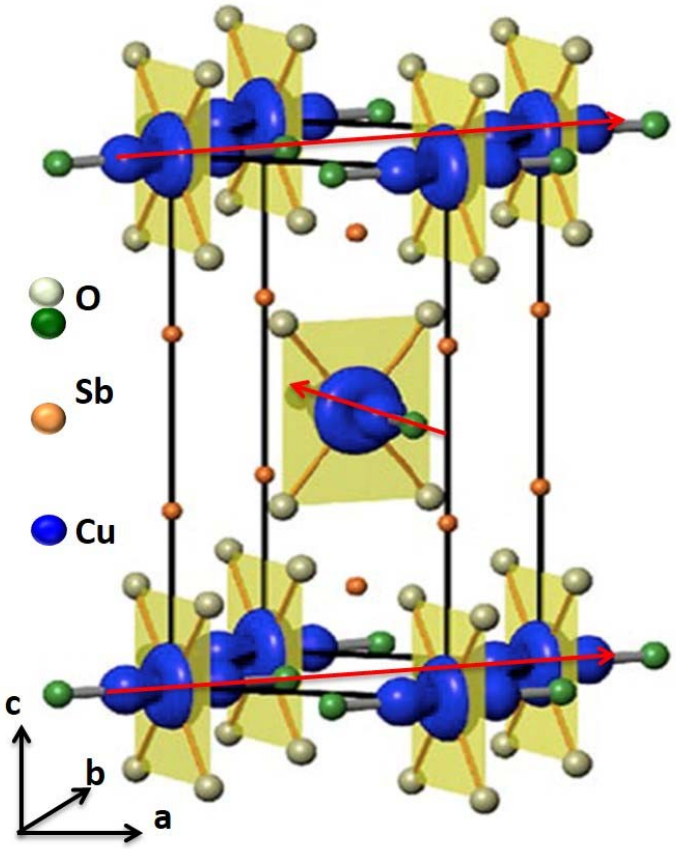

Figure 4.1 Monoclinically distorted trirutile structure of $CuSb_2O_6$. Copper atoms are separated by two antimony atoms along *c*-axis, thus tripling c-axis and forming trirutile structure. Alternating arrows show the Cu-O-O-Cu superexchange pathways corresponding to that plane.From [86].

Single crystals of $CuSb_2O_6$ were grown by vapor transport using $TeCl_4$ as a transport agent in a similar manner as described elsewhere [28]. Approximately 2.0033 g of powdered $CuSb_2O_6$ and 0.0995g of $TeCl_4$ were placed in a quartz ampoule of approximately 0.8 cm internal radius and 18 cm in length. These amounts and dimensions would give an internal pressure of approximately 1 atmosphere at 920℃. The ampoule was evacuated and flushed three times with Ar before sealing, then reacted in a tube furnace in a gradient of 3.3℃/cm (920 and 980℃ at the tube ends) for 100 hours followed by cooling at 1℃/min to room temperature. Well-faceted crystals grew at the cold end of the ampoule

and were mechanically removed after soaking the end of the ampoule overnight in dilute HCl. The crystals have typical dimensions of 3.0 x 1.0 x 1.0 mm.

$CuSb_2O_6$ has a monoclinically distorted trirutile structure [78] below 380 K with nearly undistorted CuO_6 octahedra and transition into tetragonal structure above that temperature. Figure 4.1 shows the crystal structure of $CuSb_2O_6$. Trirutile structure of $CuSb_2O_6$ can be generated from rutile structure by tripling the c-axis such that magnetic Cu^{2+} ions are separated from each other by two layers of diamagnetic Sb^{5+} ions. It also possesses a network of edge and corner sharing CuO_6 and SbO_6 octahedra.

Single crystal growth of tetragonal $ZnSb_2O_6$ using a chemical vapor transport method is described in detail elsewhere [78]. We have used x-ray diffraction to determine the orientation and crystallographic structure of the crystals as described in section 3.1.3. Lattice parameters determined from high-angle extrapolation [70] of reflections from various lattice planes were $a = 4.637(9)$Å, $b = 4.638(6)$Å, $c = 9.304(2)$ Å and $\beta = 91.1(2)^{\circ}$ for $CuSb_2O_6$, and $a = 4.653(3)$ Å, $c = 9.280(2)$ Å, for $ZnSb_2O_6$, in good agreement with prior reports for these compounds [28], [80].

In spite of two-dimensional layered structure of CuO plaquettes at $z = 0$ and $z = 1/2$ along *c*-axis, its magnetism is quasi-one-dimensional, with magnetic susceptibility well described by a nearest-neighbor-only spin-½ Heisenberg antiferromagnetic (AF) chain model and exchange coupling strength $J \approx 90-100\,K$. It has long range AF order below Neel temperature, $T_N \approx 8.7K$ [27], [28], [79], [81]–[85]. Electronic structure calculations by Kasinathan *et al.* [86] have revealed that the unusual quasi-1D magnetic ground state is driven by orbital ordering, attributed to the presence of competing in- and out-of plaquette orbitals and strong electronic correlations. The strongest 1D

superexchange interaction (Cu-O-O-Cu) is along the [110] (at $z = 0$) and [$\bar{1}$ 10] (at $z = 1/2$) directions, via the apical oxygen ions, rather than the in-plaquette oxygens. The angles of the Cu–O–O–Cu bonds of adjacent CuO_6 octahedra are close to 180°. Interchain exchange is much weaker due to a larger Cu–O bond length and 160° Cu–O–Cu bond angle.

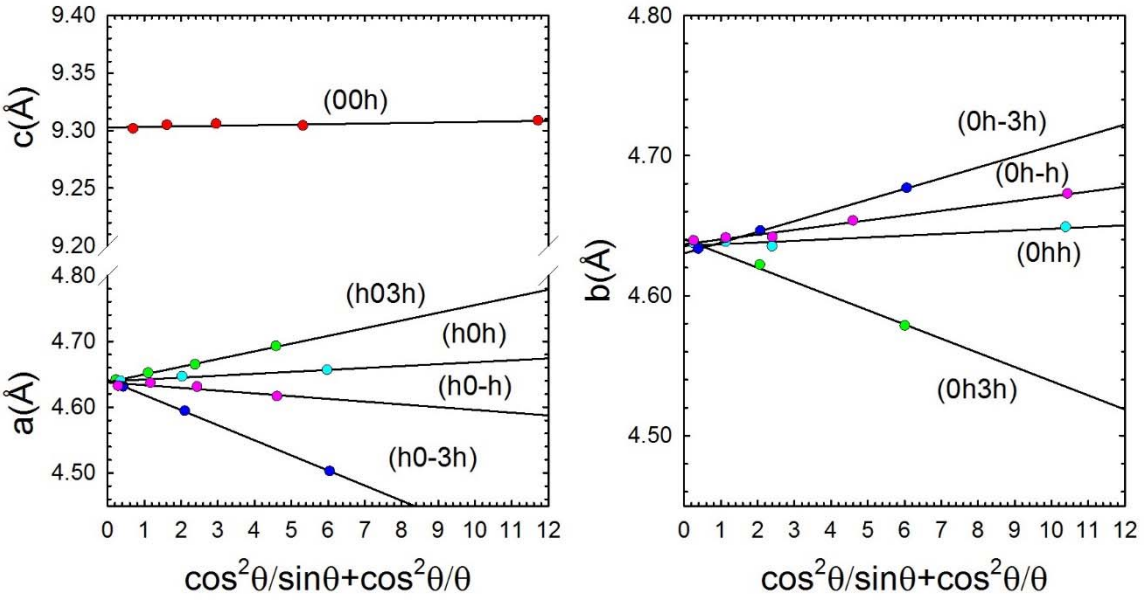

Figure 4.2 Lattice parameter calculation of $CuSb_2O_6$ from high angle extrapolation of reflections from various lattice planes as shown in plot.

Several discrepancies have been found in the literature [85], [87] regarding the appropriate magnetic structure in the ordered state. Study by Kato *et al.* [87] have proposed the collinear spins on the magnetic unit cell of $CuSb_2O_6$, whereas another study by Gibson *et al.* [85] have proposed the canting of the spins in *ab*-plane with the magnetic moment of $0.51\mu_B$. Recent single-crystal neutron scattering [88], magnetic susceptibility, and specific heat studies of the related compounds [89] $CoSb_2O_6$ and $NiTa_2O_6$, indicate magnetic moments aligned nearly parallel to [010], in ferromagnetic lines along [010] and alternating antiparallel lines along [100] (magnetic wave vector $(\pi/a, 0, \pi/c)$).

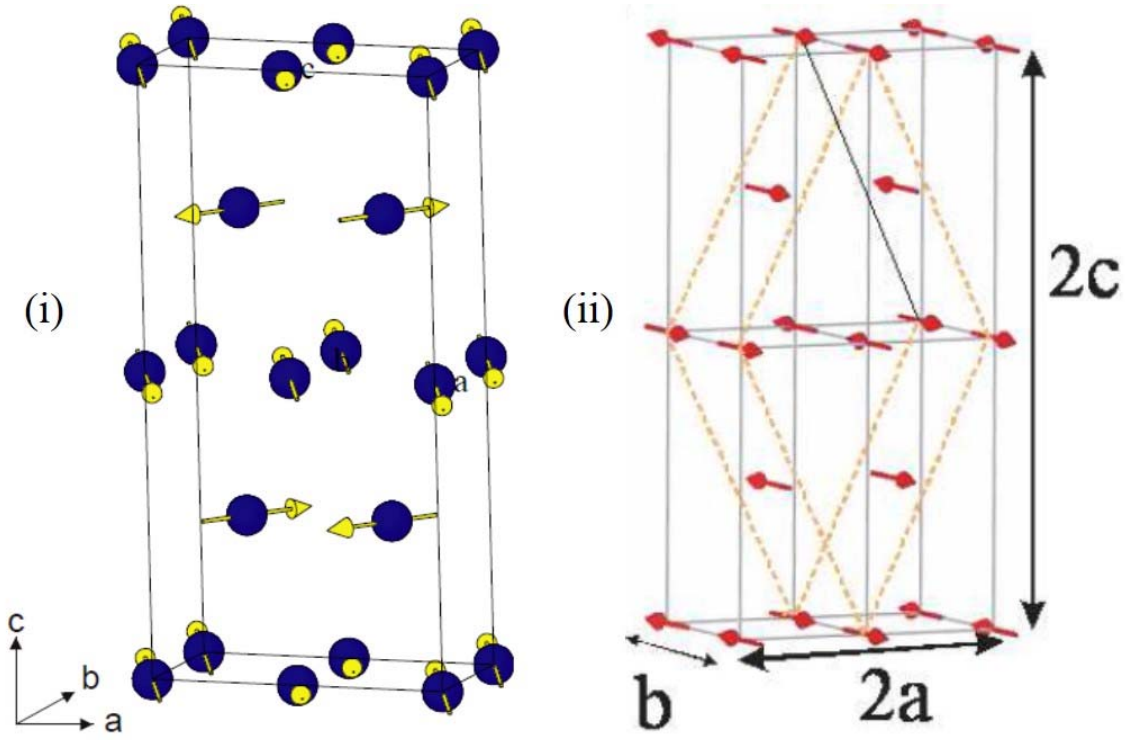

Figure 4.3 Schematics of low-*T* magnetic structure at zero field (i) with canting of spins in *ab*-plane from [85] and collinear spin structure from [88] where magnetic unit cell is indicated by the dotted lines.

4.3 BICRYSTALLINITY AND TWINNING

4.3.1 BICRYSTALLINITY

Although most of the single crystals we received were already oriented and checked for bicrystallinity, characterizing individual crystals with x-ray diffraction (XRD) proved essential to determining intrinsic thermal conductivities of these compounds because of the potential for bicrystallinity. The presence of two crystalline domains was not readily apparent upon visual inspection and in some cases was not detected in Laue images. However, bicrystalline specimens had dramatically suppressed thermal conductivities as shown in Figure 4.4

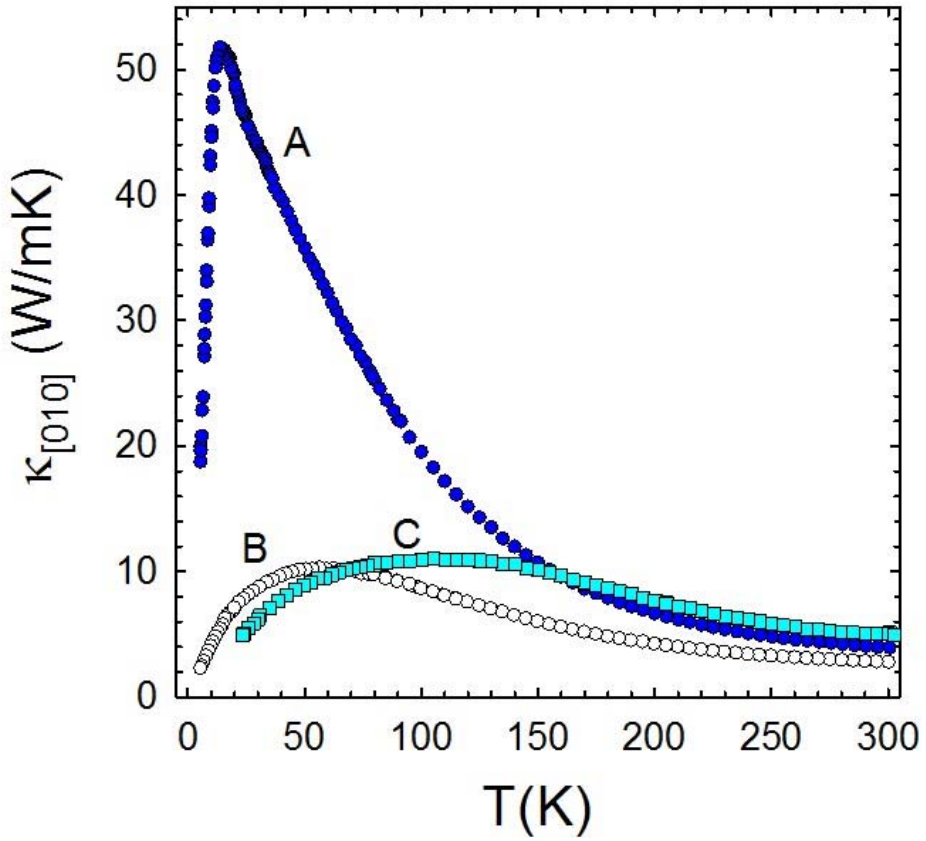

Figure 4.4 Thermal conductivity vs temperature along the [010] direction for three $CuSb_2O_6$ crystals. Substantially reduced low-T magnitudes are observed for bicrystals (B and C) as compared to the monodomain crystal (A).

After the fact, we looked carefully on previously done scans and did more scans whenever necessary. For the monodomain crystal (A) (Figure 4.4), we observed single peak in 360° phi scan of 2θ fixed for (006), whereas multiple peaks at uncorrelated angles were observed for bicrystals (B and C) as shown in lower panel of Figure 4.5. After optimizing one of these multiple peaks and doing $5 - 10^{\circ}$ phi scan around that optimized phi angle (2θ fixed for (039) plane) shows two or three peaks within $2 - 4^{\circ}$ as shown in upper panel of Figure 4.5. These multiple peaks are because of slightly disoriented multiple domains in a crystal such that each domain normal becomes parallel to diffraction vector at different phi angle, thus producing multiple phi peaks on 360°phi scan as shown in

Figure 4.6. We have compared also the rocking curve of three crystals for which κ[010] was measured. We observed single narrow peak for (006) of the crystal A with higher κ but two peaks for crystals B &C as shown in Figure 4.7. From the observed omega scans, it can be inferred that crystals B and C contain at least two domains with low angle boundary between them. We think that substantially reduced low-T κ is due to much stronger phonon scattering at domain boundaries. Such crystals were excluded from subsequent study.

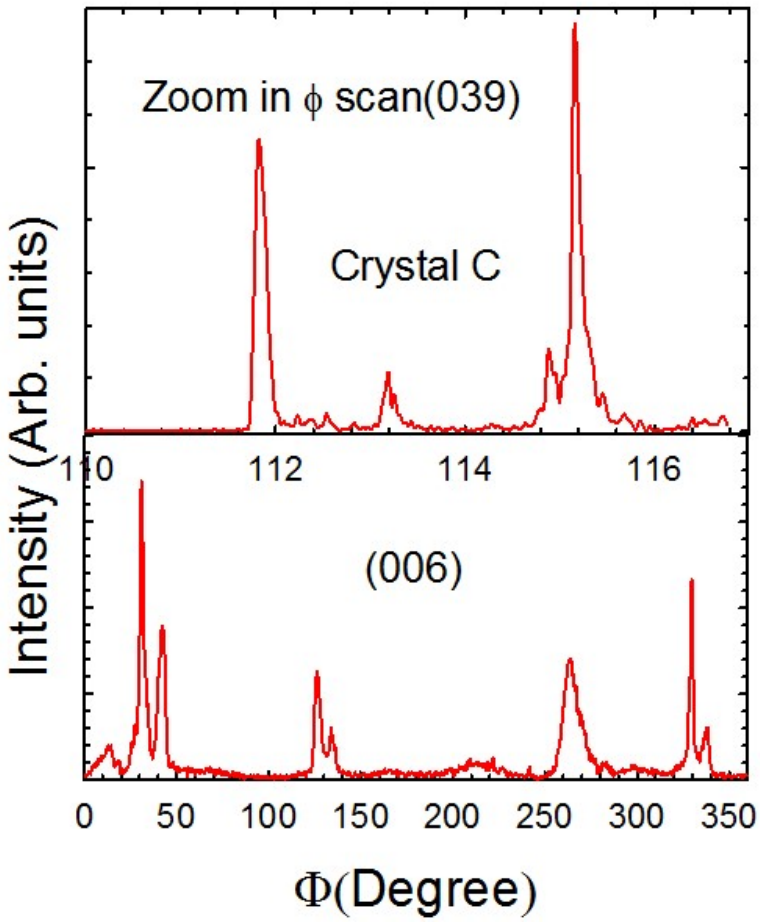

Figure 4.5 Phi scans for crystal C. (Lower panel) 360° phi scan with 2θ fixed for (006) shows multiple peaks at uncorrelated angles. (Upper panel) 10° phi scan with 2θ fixed for (039) shows three peaks within 4°.

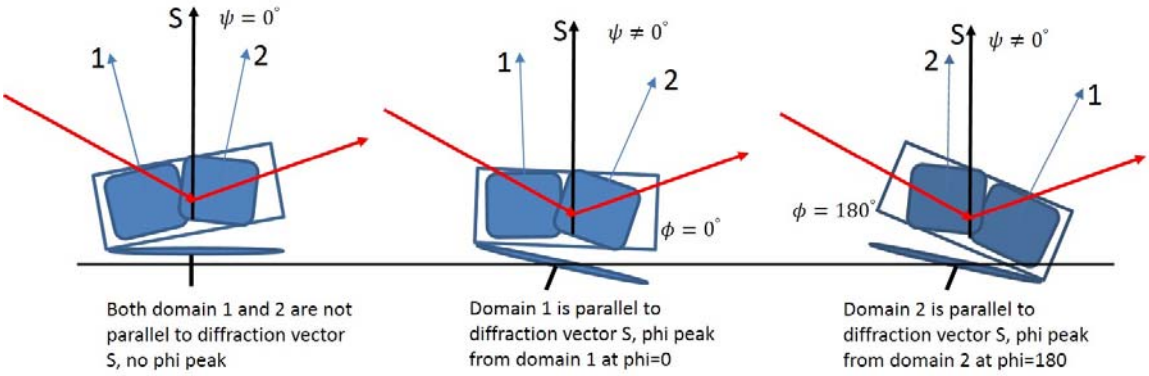

Figure 4.6 Schematics of multiple peaks from 360° phi scan of multi-domain crystal.

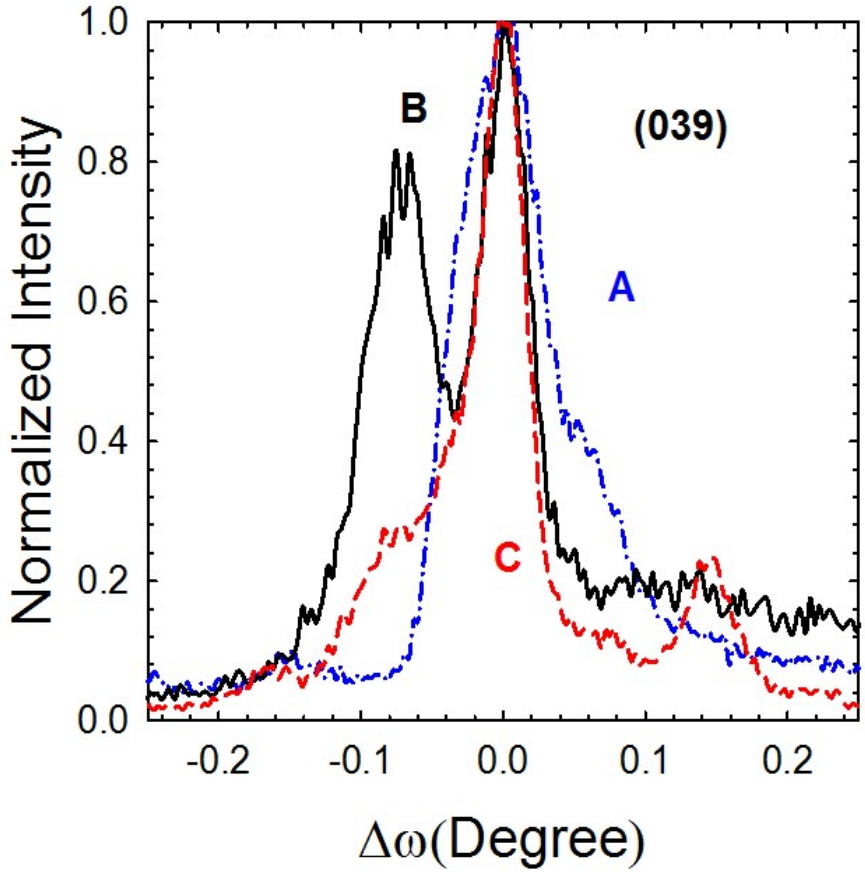

Figure 4.7 Rocking curve of three crystals for which κ was measured along [010]. Crystal A (higher κ) shows single domain and crystal B &C (lower κ) show two domains.

4.3.2 TWINNING IN THE CRYSTAL

Single crystals of $CuSb_2O_6$ are reported to have twinning associated with the tetragonal to monoclinic transition around 383 K [28], [78]. It was evident in the triple splitting of $(0h3h)$ plane reflection in 2θ scan as shown in Figure 4.8, in similar fashion as suggested in ref.[28]. These triple split peaks observed in the scan correspond to $(\bar{h}03h)$, $(0h3h)$ and $(h03h)$ respectively. Observed splitting of each peak into two is because of $K_{\alpha 2}$ radiation from x-ray.

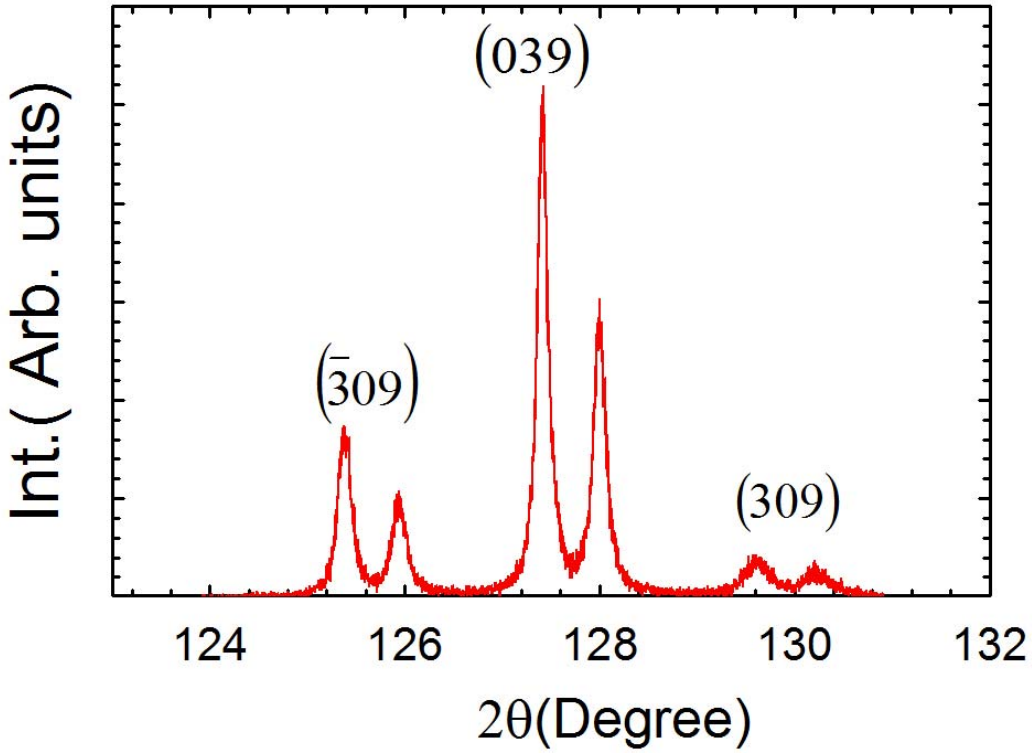

Figure 4.8 Triple splitting of $(0h3h)$ reflection observed during 2θ scan. Splitting of each peak into two is because of $K_{\alpha 2}$ radiation from x-ray.

Extensive pole figure scan was required to identify the monodomain crystal as well as to quantify the twin variant present in the crystal. Study implied two principal twin variants: (1) 180° rotations of the *b*-*c* plane about the *a* axis as shown in Figure 4.9(a) and (2) 90° rotations of the *a*-*b* plane about the *c* axis (i.e., a swapping of *a* and *b* orientations).

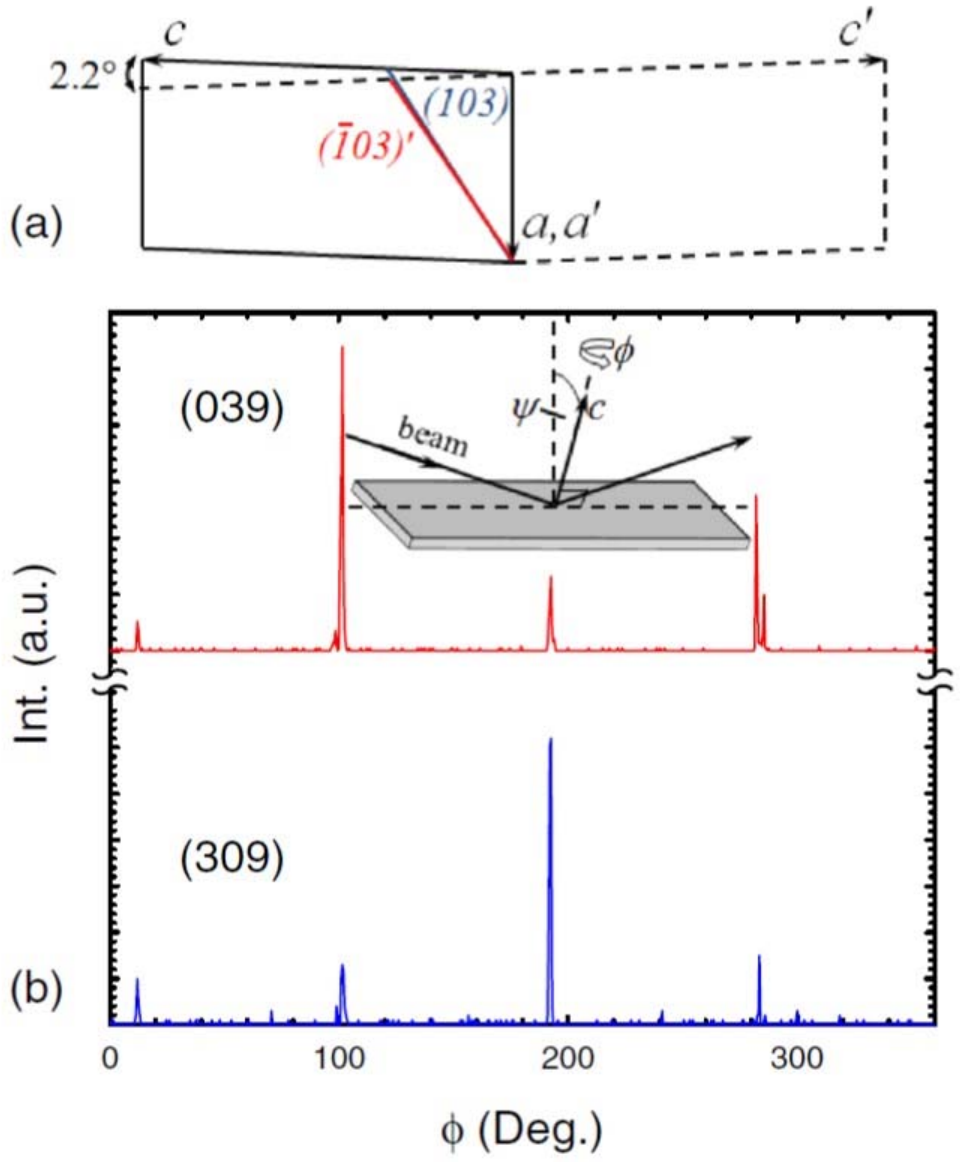

Figure 4.9 (a) Schematics of twin variant one inferred from XRD for $CuSb_2O_6$ crystals. (b) Phi scans for the (039) and (309) reflections such that values of 2θ and ψ correspond to those reflections. Inset shows the geometry of the XRD scans for crystals oriented with their c axes along the thinnest direction.

Because of swapping of *a* & *b* orientations, orienting crystals can be confusing sometimes. But azimuthal (ϕ) scans of the (039) and (309) reflections as shown in Figure 4.9(b) demonstrate that the [100] and [010] directions remain distinguishable. Therefore, careful study makes it possible to orient a crystal either along *a* or *b* axis and thus twins of variant (2) are in the minority.

To investigate the possible role of these twins on the heat transport, κ for two specimens was measured in a separate high-T vacuum probe up to T = 390 K, i.e., above the structural transition where the structural twins are known to disappear [28]. These data show no abrupt increase in κ at the phase transition temperature as would be expected if twin boundaries were strong phonon scatters (Figure 4.10). We thus conclude that such growth twins have little influence on the heat transport of the Cu compound near room temperature and above.

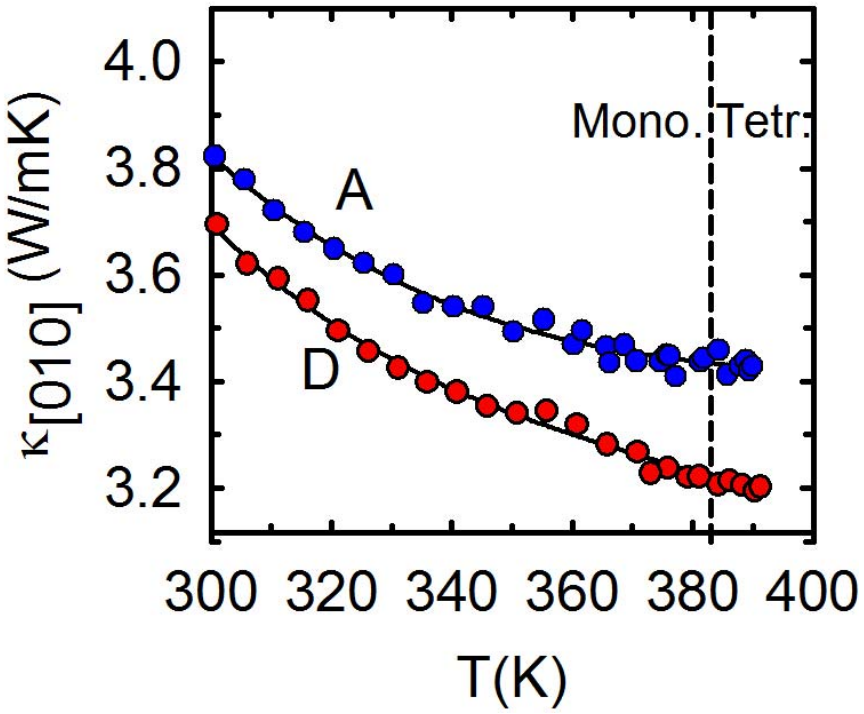

Figure 4.10 High-T data through the tetragonal-monoclinic structural transition at 383 K (dashed line) for two crystals A (monodomain) and D (bicrystal).

4.4 QUALITY OF SINGLE CRYSTALS

After excluding obvious bicrystals from further study, we compared the rocking curve of single crystals of $CuSb_2O_6$ and $ZnSb_2O_6$ to check their quality. As rocking curve

is obtained by tilting the crystal and allowing to obtain reflection from disoriented crystal planes, broad and multiple peaks are indicator of low quality of single crystals. Quality of the $CuSb_2O_6$ and $ZnSb_2O_6$ crystals was evident in rocking curve width (FWHM), $\Delta\omega \leq 0.06^{\circ}$ corresponding to (006) reflections as shown in Figure 4.11. Little bit higher

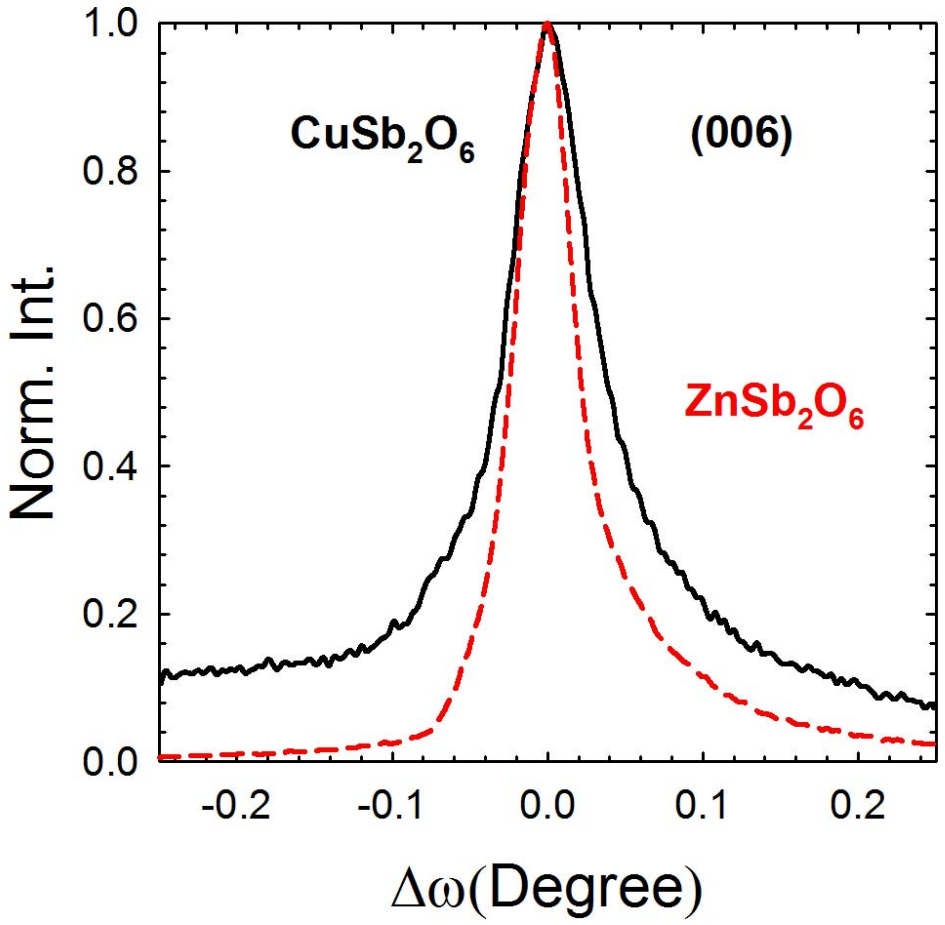

Figure 4.11 Rocking curve of $CuSb_2O_6$ and $ZnSb_2O_6$ crystals with their (006) reflections. Rocking curve width (FWHM), $\Delta\omega \leq 0.06^{\circ}$ indicates the quality of single crystals.

background of Cu compound in Figure 4.11, is because of higher relative intensity of Zn compound than that of Cu compound. This difference in relative intensity arises from the different size of the specimens as other factors were kept similar during the scans.

4.5 RESULTS FROM $\kappa(T)$ MEASUREMENTS

4.5.1 THERMAL CONDUCTIVITY OF $CuSb_2O_6$

For $CuSb_2O_6$ thermal conductivity (κ) was measured with heat flow along the principal crystallographic directions as well as along the direction of spin chains [110]. Figure 4.12 shows the thermal conductivity of $CuSb_2O_6$ for various crystallographic directions. Thermal conductivity (κ) is isotropic for $T \geq 150\,K$, however it becomes

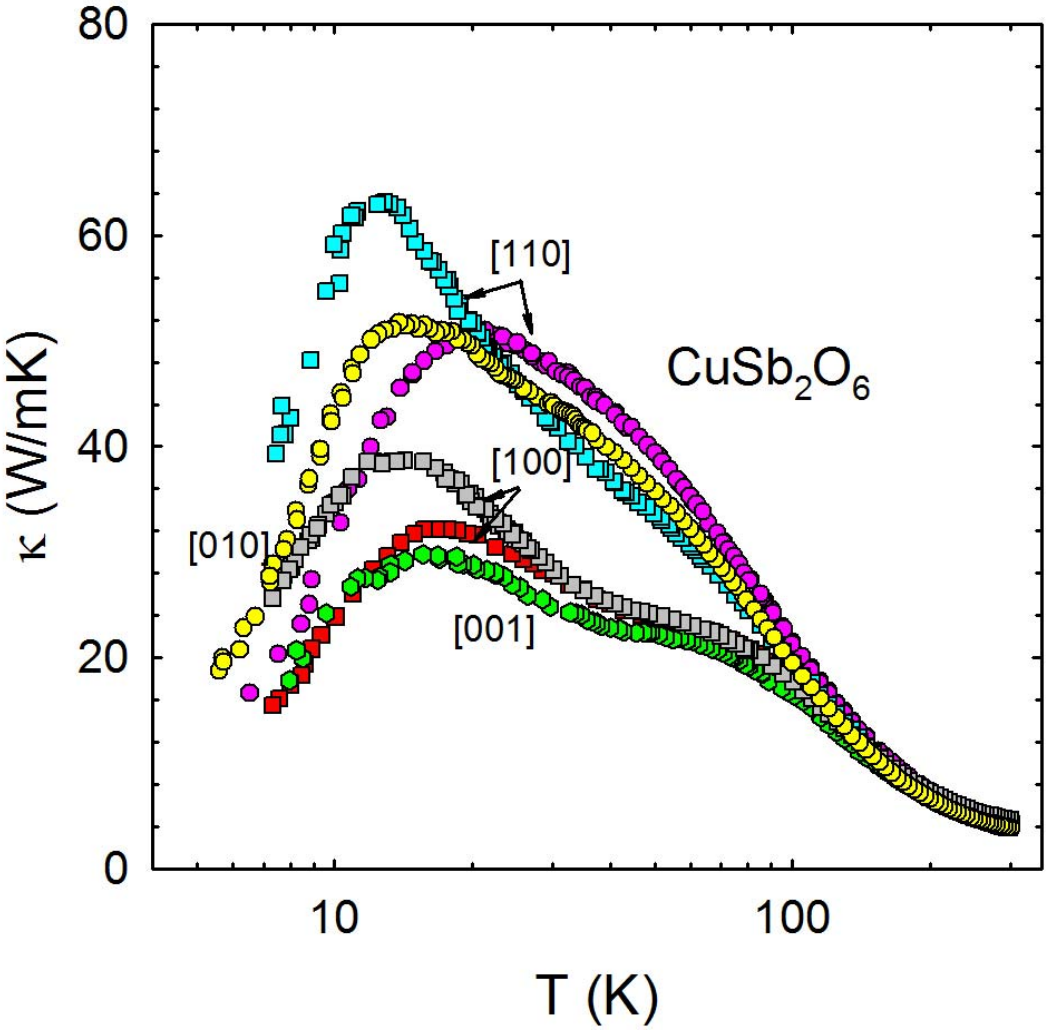

Figure 4.12 Thermal conductivity of $CuSb_2O_6$ single crystals with heat flow along the directions indicated in figure.

anisotropic at $T \leq 150\,K$. Along [100] and [001] $\kappa(T)$ exhibits a diplike feature at $40-50\,K$. Hints of this feature are also evident along [010] and [110], but the magnitude of κ along these directions is significantly higher. The sensitivity of κ within the *a*-*b* plane to misalignment of the crystallographic axes is demonstrated by the pairs of data sets (designated by arrows in Figure 4.12), for nominally [110] and [100] orientations. For these orientations, the curves with lower magnitude below $20\,K$ correspond to crystals that were misaligned out of the *a*-*b* plane by 5° or more, and thus had a component of the heat flow oriented along [001]. All other crystals were oriented to within 1°.

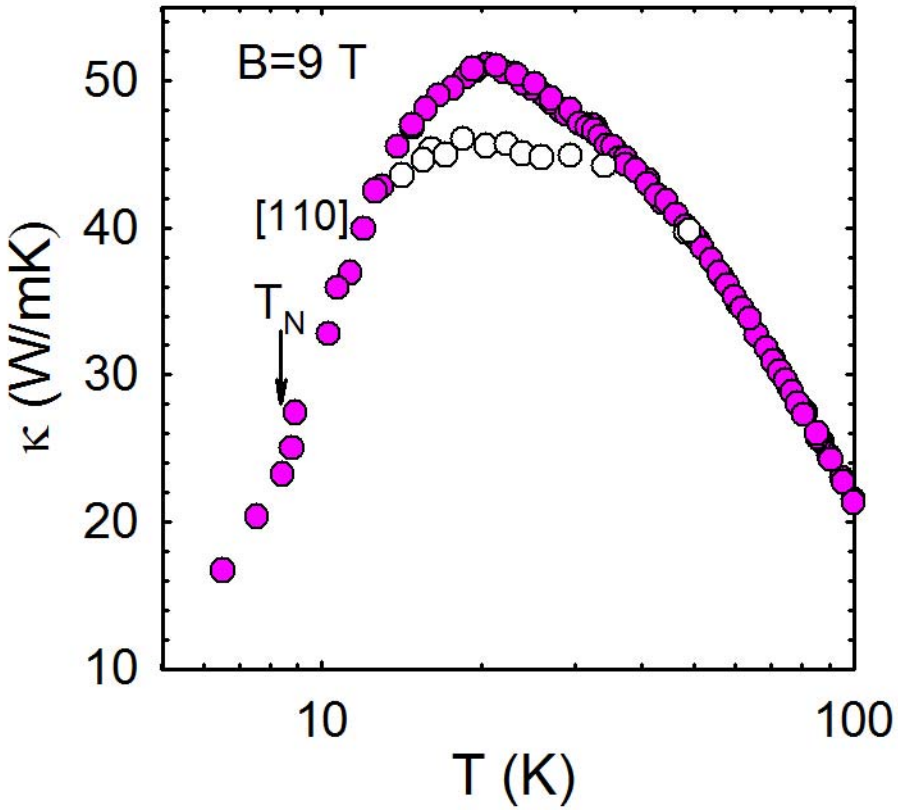

Figure 4.13 Magnetic field dependence of $\kappa(T)$ at a field of $9\,T$ with both field and heat flow direction along [110]. Filled circle represents $\kappa(T)$ at zero field and unfilled circle at $9\,T$.

4.5.2 MAGNETIC FIELD DEPENDENCE OF $\kappa(T)$

We have measured κ in a 9 T magnetic field with field orientation and direction of heat flow both along the spin chain direction [110]. The magnetic field dependence of κ was modest in magnitude as shown in Figure 4.13. A suppression of κ by $\sim 10\%$ was observed near the zero-field maximum. Also evident in this figure is a slight downturn in κ below T_N for this specimen and also for that measured along [100] which is not shown here. Magnetic field can both enhance and suppress magnitude of thermal conductivity which makes the analysis more complicated. First, we know that spin chain can contribute to heat transport, there is a positive contribution to κ from heat transported by the spin chains. Second, heat conduction by phonons can be reduced when phonons are scattered off the spin fluctuations. Also, there is potentially a third contribution from spin-phonon drag which is mostly positive[90]. The suppression of $\kappa(T)$ shows that second mechanism might be dominant in this system. However, we did not pursue this further because field dependence was very modest only near the peak of $\kappa(T)$.

4.5.3 COMPARISION WITH NON-MAGNETIC ANALOG $ZnSb_2O_6$

We have also measured $\kappa(T)$ for single crystal of $ZnSb_2O_6$ which is a non-magnetic analog of $CuSb_2O_6$ to gain insight into the role of spins in the heat transport on Cu compound by comparing $\kappa(T)$ of both compounds. Figure 4.14 shows the combined plot of κ(T) for $CuSb_2O_6$ and $ZnSb_2O_6$ crystals with heat flow along various crystallographic directions. The short dimension of $ZnSb_2O_6$ crystal along [001] precluded the measurement of κ(T) along that direction. Most striking is the substantially larger κ for nonmagnetic $ZnSb_2O_6$ throughout most of the temperature range, which, as established in the preceding sections (see section 4.3 and 4.4), cannot be attributed to twinning or poor

crystallinity of the Cu compound. The maximum at T = 30 K is typical of crystalline insulators [55] near $\frac{\theta_D}{20}$ (θ_D is the Debye temperature), occurring as the dominant phonon scattering changes from anharmonic phonon-phonon at high temperatures to defect and boundary scattering at low temperatures. Both compounds have similar Debye temperatures $(467(5)\ K$ and $539(30)\ K$ for Cu and Zn compound respectively) [79] and

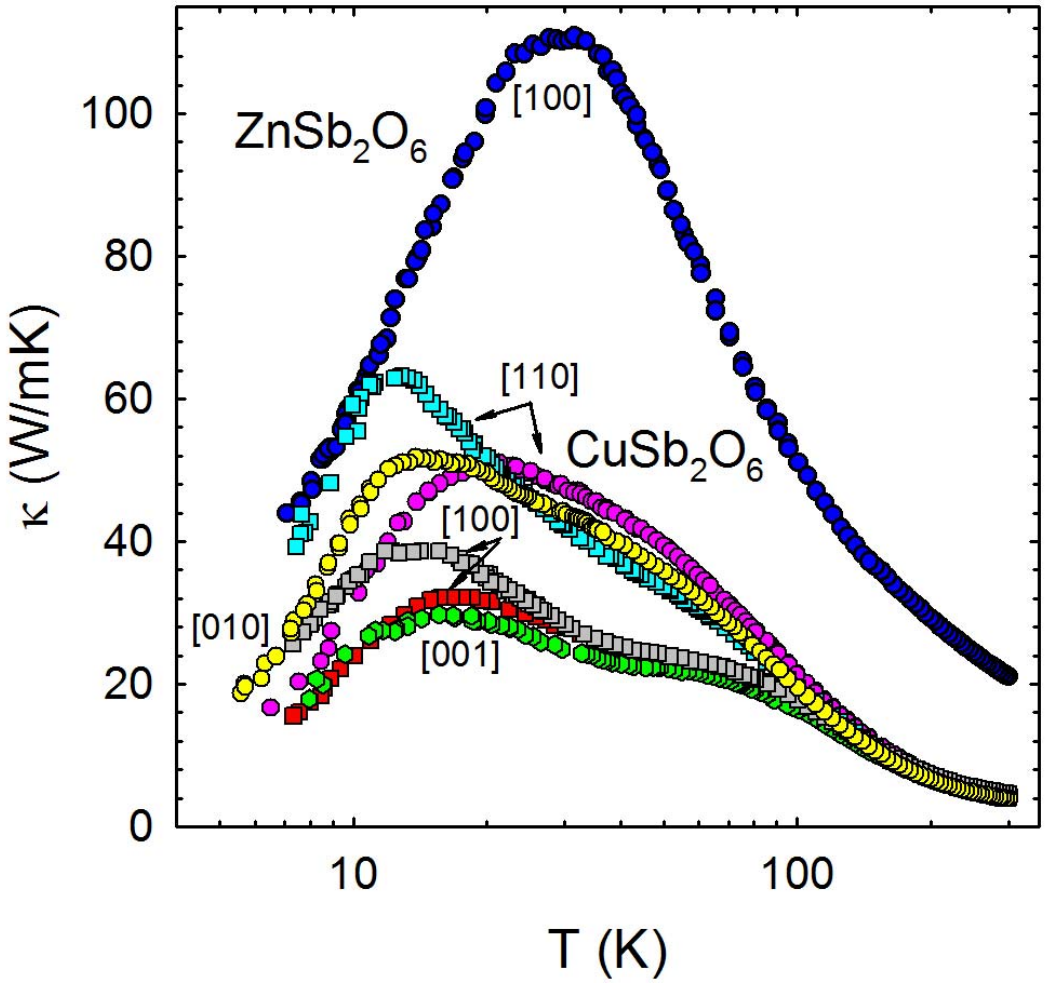

Figure 4.14 Combined plot of thermal conductivity of single crystals of $CuSb_2O_6$ and $ZnSb_2O_6$ with heat flow along the indicated directions in figure.

thus we should expect this maximum at a similar temperature for the Cu compound. The implication is that substantial additional scattering of phonons is operative in $CuSb_2O_6$.

4.6 ANALYSIS OF RESULTS FROM $\kappa(T)$

In this section, analysis of results from thermal conductivity measurements will be presented. Possible role of spin-phonon scattering as well as other scattering mechanism will be discussed. Modelling of $\kappa(T)$ based on Callaway model [64] and justification of relaxation time approximation used will be discussed. Finally, possible magnetic contribution to heat transport and thus resulting magnetic mean free path will be presented.

4.6.1 PHONON-SPIN RESONANT SCATTERING

First we consider the source of additional phonon scattering that underlies the much smaller $\kappa(T)$ found for $CuSb_2O_6$ relative to that of $ZnSb_2O_6$ over most of the temperature range. This scattering is responsible for the dip in $\kappa(T)$ curves noted above. Such features are the signature of resonant scattering in which heat-carrying phonons are strongly damped over a restricted frequency range. The dominant phonons responsible for κ have energies $\sim 3.8k_BT$, thus we anticipate a resonant interaction for phonons with energies $\sim 13-16\ meV$. Any suppression of κ attributed to resonant phonon–spin scattering must be relatively isotropic given that it is evident for heat flow both within and perpendicular to the plane of the spin chains. This suggests an interaction between phonons and localized spin states rather than dispersive states with momenta confined to the *a*-*b* planes. A mechanism like this was introduced [91] to describe resonant phonon–spin scattering in the two-dimensional spin-dimer system $SrCu_2(BO_3)_2$: a phonon excites the spin system and

under de-excitation a phonon emitted with the same energy is uncorrelated in its direction with the first (the initial and final spin states are the same).

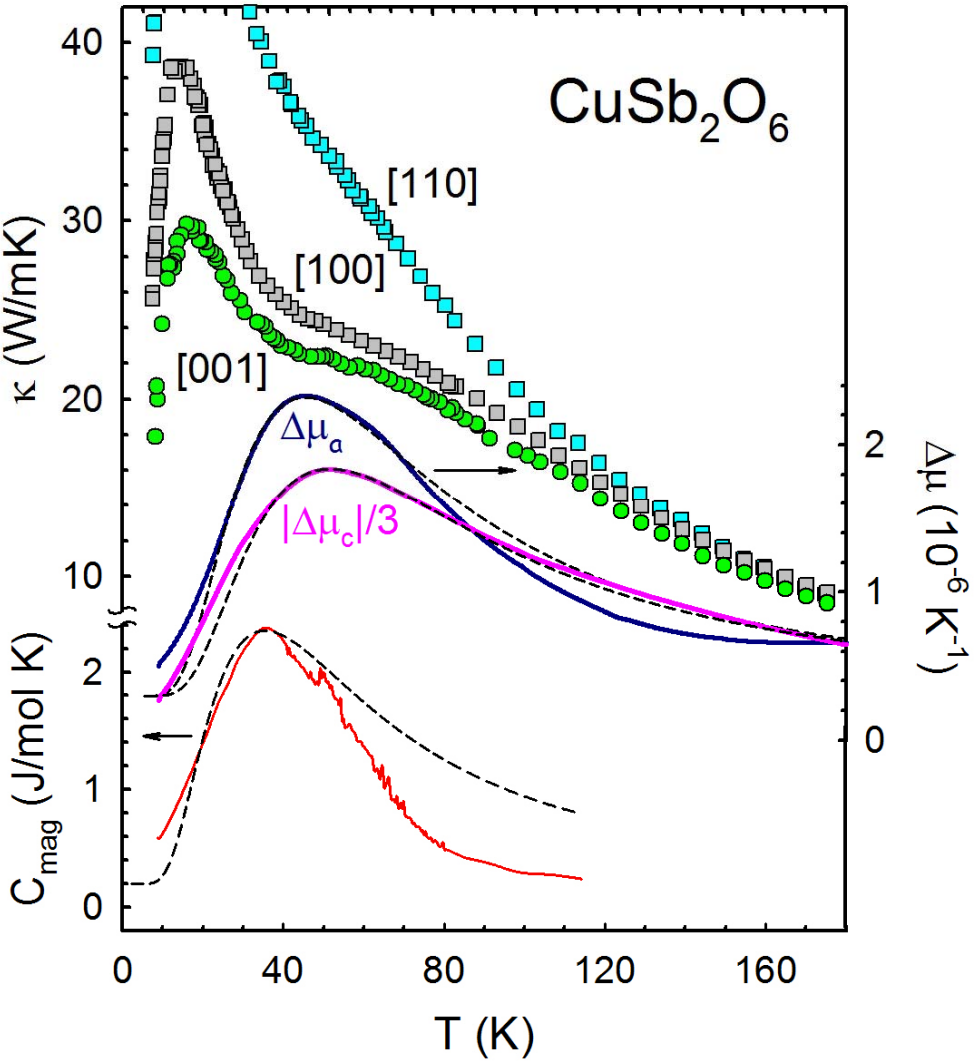

Figure 4.15 (Top left ordinate) thermal conductivity for $CuSb_2O_6$ along [001], [100], and [110] directions, (right ordinate) difference in linear thermal expansion coefficients of $ZnSb_2O_6$ and $CuSb_2O_6$ and (lower left ordinate) magnetic specific heat from Ref. [79]. Dashed curves are fits to the Schottky expression as shown in the text below.

Further insight into the resonant scattering mechanism is found in specific heat and thermal expansion studies [79] of $ZnSb_2O_6$ and $CuSb_2O_6$. Figure 4.15 shows $\kappa(T)$ data along the [100], [001], and [110] directions for $CuSb_2O_6$ on an expanded linear scale for

$T \leq 175\,K$ along with the magnetic specific heat, $C_{mag} = C_p(Cu) - C_p(Zn)$, and the difference in the *a*- and *c*-axis linear thermal expansion coefficients for Cu and Zn compounds, $\Delta\mu_i = \mu_i(Cu) - \mu_i(Zn)$ $(i = a, c)$. Note that $\mu_a \approx \mu_b$ throughout this temperature regime, and since $\mu_c(Cu)$ is negative, we plot $|\Delta\mu_c|$. Two features are noteworthy. The rise in C_{mag} and the $\Delta\mu_i$ below $T \cong 150\,K$, which signal the onset of spin correlations and associated anharmonicity, respectively, in the Cu compound [79], coincide with the onset of anisotropy in $\kappa(T)$. The maxima in the magnitudes of C_{mag} and the $\Delta\mu_i$ at $T \cong 40\text{–}50\,K$ coincide with the "dip" in $\kappa(T)$ noted above for both the [100] and [001] directions.

Unlike the case in strongly coupled spin-Peierls systems (e.g., [92] $CuGeO_3$) where the N*é*el transition involves dimerization of spins and substantial lattice distortions, the specific heat and thermal expansion for $CuSb_2O_6$ indicate a gradual loss of spin entropy [79] associated with *local* 1D spin ordering and lattice modifications beginning well above $T_N = 8.7K$. By implication, the resonance like phonon scattering evidenced in $\kappa(T)$ involves phonon-induced excitations of the locally ordered spin chains.

The maxima in C_{mag} and the $\Delta\mu_i$ are reminiscent of Schottky anomalies for two-level systems, though this is an oversimplification since the loss of spin entropy [79] from $120K$ to T_N is ~ 60% of $R\ ln\ 2$. In the simplest case (Gr*ü*neisen scaling), $\Delta\mu \propto C_{mag}$ [93]:

$$\Delta C_{mag} = k_B \left(\frac{\varepsilon}{T}\right)^2 \frac{e^{-\varepsilon/T}}{\left(1 + e^{-\varepsilon/T}\right)^2}, \tag{4.1}$$

$$\Delta\mu_i = \frac{1}{V_{fu}} \frac{\partial \ln \varepsilon}{\partial p_i} \Delta C_{mag}, \tag{4.2}$$

where ε is the energy splitting, V_{fu} is the formula unit volume, and p_i the uniaxial pressure. The $\Delta\mu_i$ and C_{mag} can have different T dependencies when the pressure derivative depends on T or when there are more than two levels each with independent pressure derivatives. Allowing for different effective values for ε, the dashed curves in Figure 4.15 give reasonable approximations to experiment and correspond to the above expressions (with the addition of small constant terms, 0.2 $J/mol\,K^2$ for C_{mag} and $3 \times 10^{-7}\ K^{-1}$ for the $\Delta\mu_i$) using $\varepsilon = 85\,K$ for C_{mag} and $\partial\, ln\, \varepsilon/\partial p_i = 4.35 \times 10^{-10}\ Pa^{-1}$ ($1.52 \times 10^{-10}\ Pa^{-1}$), $\varepsilon = 109\,K$ ($124\,K$) for the a-axis (c-axis) expansion coefficients. As we discuss in the next section, this energy scale $\varepsilon \sim 100\,K$ also describes the resonant scattering in κ.

A clear physical picture of the relevant lattice/spin excitations and their scattering of heat-carrying phonons remains to be established. Inelastic neutron scattering studies [88] of $CuSb_2O_6$ identified a strong resonance feature at energy $\sim 13\,meV$ in the magnetic excitation spectrum for momentum transfer $q = 3\pi/4a$ along the [100] direction. This is close to where the free spinon dispersion has a maximum [3], [30] at $(\pi/2)J$ as shown by small grey circle in Figure 4.16. This resonance is observed well above T_N and grows in intensity with decreasing T, and is thus likely related to the development of short-range magnetic order. Based on its unusual intensity distribution, the resonance was proposed [88] to couple with B_{1g} optical phonons which involve rotations of the CuO_6 octahedra about the [001] direction and thereby modulate the Cu–O–O–Cu bond angle and superexchange interaction along [110] as shown in the inset of Figure 4.16. However, the B_{1g} mode is strongly dispersing in the rutile structure [94] and is expected at energies $> 20\,meV$ at the momentum corresponding to the resonance (see Figure 4.16). This mode

involves only oxygen motions, and thus it is unlikely that in the trirutile structure of $CuSb_2O_6$ it would be found at a much lower energy compatible with that of the resonance.

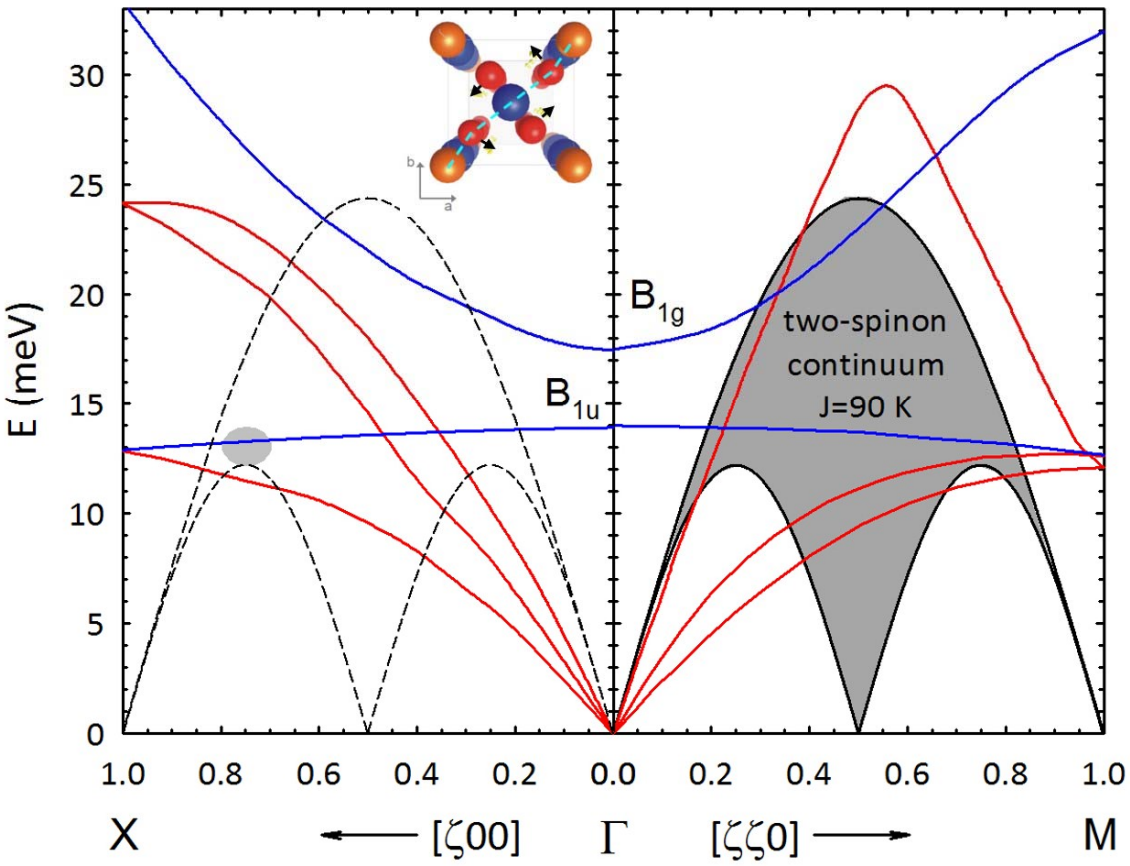

Figure 4.16 Selective lattice dispersion relation of rutile structure (reproduced from [94]) plotted with spinon dispersion. Dispersion of acoustic and optical modes are shown in red and blue solid lines respectively. Inset shows the rotation of CuO6 octahedra about [001] and thus, modulation of Cu-O-O-Cu bond angle (from [88]).

In ref. [79] it was proposed that the short-range magnetic order at $T \geq T_N$ reflects the formation of *local* spin-Peierls ordered domains (e.g., dimerized chain fragments). Such a scenario has the potential to reconcile the absence of typical spin-Peierls anomalies in the specific heat and thermal expansion at T_N and the appearance of a gap at $T \leq T_N$. This raises the possibility that the $\sim 100K$ energy scale evidenced in the thermodynamic properties and thermal transport, comparable to J, is connected with singlet-triplet

excitations. Further theoretical and experimental work is required to address this speculation.

4.6.2 MODELLING OF $\kappa(T)$ DATA

Calloway model [64] fitting to the data was employed to quantify the additional phonon scattering that operates in the magnetic Cu compound. $\kappa(T)$ was computed as given by Eq (2.25),

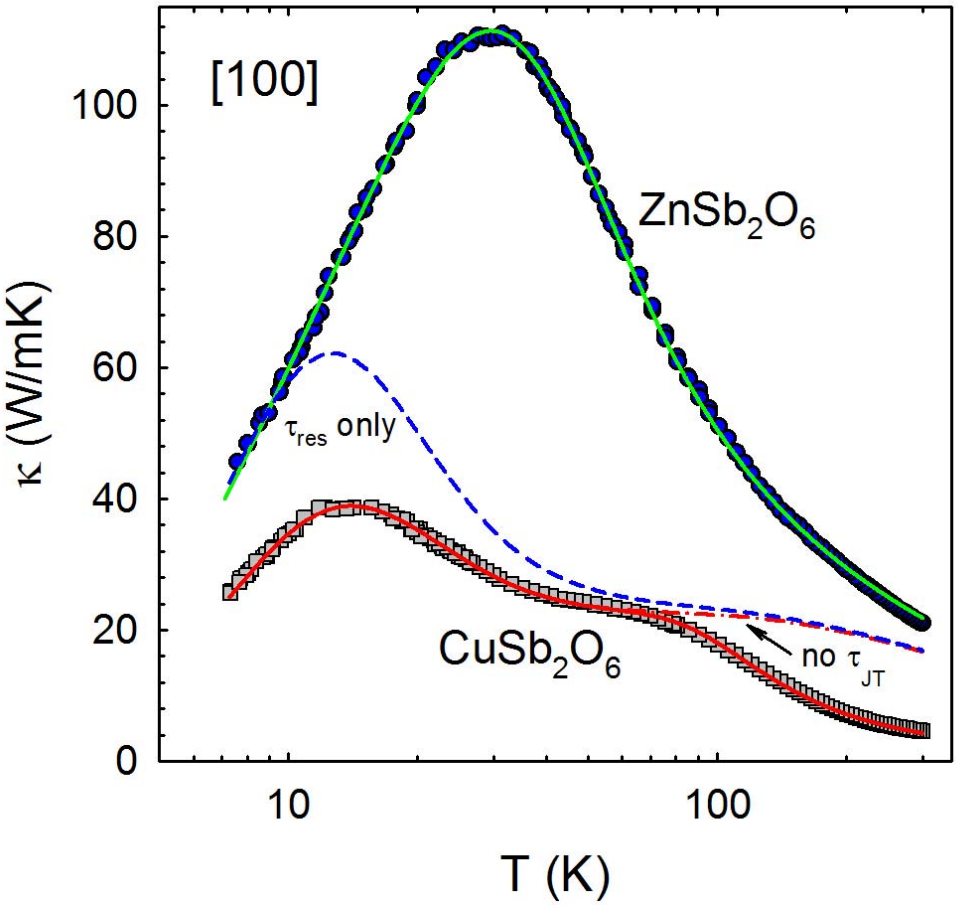

Figure 4.17 Model fitting to $\kappa_{[100]}$ data for $ZnSb_2O_6$ and $CuSb_2O_6$. Parameter values required for fitting are given in Table 4.1. Other curves shown in figure are curves for the Cu compound excluding all but the resonant scattering term (dashed curve) and with all terms except the Jahn-Teller term (dashed-dotted curve)

$$\kappa = \frac{k_B}{2\pi^2 v}\left(\frac{k_B}{\hbar}\right)^3 T^3 \int_0^{\theta_D/T} \tau(\omega, T)\frac{x^4 e^x}{[e^x - 1]^2} dx. \quad (4.3)$$

where $x = \hbar\omega/k_B T$, ω is the phonon angular frequency, and $\tau(\omega, T)$ is the phonon relaxation time. The Debye temperature is computed from the average phonon velocity (v) as $\theta_D = (\hbar v/k_B)(6\pi^2 n)^{1/3}$, where n is the atom density.

We first fitted the $\kappa(T)$ data for $ZnSb_2O_6$ by incorporating phonon scattering terms representing boundaries, point defects, and Umklapp processes, respectively:

$$\tau(\omega, T)^{-1} = \frac{v}{L_b} + A\omega^4 + BT\omega^2 e^{-\frac{\theta_D}{bT}} \quad (4.4)$$

where L_b is taken as the minimum sample dimension, and A, B, and b are fitting parameters. The phonon velocity was taken as $v = 4.8\ km/s$, an average of the rutile sound velocities [94]. The results of the fitting is shown in Figure 4.17 and its parameter values are included in Table 4.1.

Table 4.1 Parameter values for the fitting to $\kappa_{[100]}$ data for crystals shown in table.

Compound	$\boldsymbol{B \times 10^{-18}}$ $(\boldsymbol{sK^{-1}})$	$\boldsymbol{b}$	$\boldsymbol{v(kms^{-1})}$	$\boldsymbol{A}$ $\boldsymbol{(s^3)\times 10^{-43}}$	$\boldsymbol{C(s^2)\times 10^{-18}}$	$\boldsymbol{R(s^3)\times 10^{-34}}$	$\boldsymbol{D(s^3)\times 10^{-41}}$
$ZnSb_2O_6$	1.05	6.5	4.8	2.46	0	0	0
$CuSb_2O_6$	1.05	6.5	4.8	2.19	5.55	2.49	2.22

Fitting to the $CuSb_2O_6$ [100] (or [001]) data employed the same values for v, B, and b as for the $ZnSb_2O_6$ fitting and included three additional scattering terms. At the lowest temperatures a sheet like fault scattering term, $C\omega^2$,was introduced to account for the much lower magnitude of κ in the Cu compound—this term is attributed to scattering from twin

boundaries. Resonant scattering from the two-level magnetic system was represented as [61], [95], [96]

$$\tau_{res}(\omega,T)^{-1} = R\frac{\omega^4\,\omega_0^4}{(\omega_0^2-\omega^2)^2}F(T), \tag{4.5}$$

where R is the scattering strength, ω_0 is the resonance frequency, and $F(T)$ is a factor that accounts for thermal occupancies of the two states. Two-level systems that exist only at the interface between ordered and "not yet ordered" regions, i.e., domains of high strain, would suggest $F(T) = n_0(1-n_0)$, where $n_0 = [1+exp(-\hbar\omega_0/k_BT)]^{-1}$ is the fraction of two-level systems in the ground state. The best fit using this form for $F(T)$(see Figure 4.17) yields a resonance energy, $E_0 = \hbar\omega_0/k_B = 67\,K$, comparable to but somewhat smaller than the two-level energy splittings found from the specific heat and thermal expansion. If $F(T)$ defines a narrower range in T, then the fitted value for E_0 increases. For example, taking $F(T)$ to be the full Schottky function, $(E_0/T)^2 n_0\,(1-n_0)$, yields a best fit of comparable quality with $E_0 = 105\,K$. Thus the resonance energy inferred from the fitting is in reasonable accord with the two-level energy splitting. To distinguish the influence of these additional scattering terms, Figure 4.17 also shows the computed $\kappa(T)$ including only the resonant scattering term (dashed line) and both the resonant and sheetlike fault scattering terms (dash-dotted line).

A third term was introduced to account for additional scattering, evident above $100K$ in Figure 4.17, that we attribute to the dynamic Jahn-Teller effect, a feature of the tetragonal phase of the Cu compound at $T > 383\,K$ that freezes out gradually at temperatures below the tetragonal-monoclinic transition. It involves thermal excitation of different orientations of the elongated Cu–O bonds of the two inequivalent CuO_6 octahedra within the unit cell [78] and is reflected in the T dependence of the monoclinic β angle

which serves as an order parameter for the transition and becomes T independent at $T \leq 100\ K$ [84]. Such dynamic local distortions of the octahedra are anticipated to behave as point defect scatterers of heat-carrying phonons with a thermally activated scattering rate determined by the characteristic optical phonon energy scale. A term $\tau_{JT}^{-1} = D\omega^4\ exp(-490/T)$ described the additional scattering well (see Figure 4.17). The phonon energy, $490\ K \cong 42\ meV$, agrees with electron-spin-resonance studies [84] which indicate a phonon at $44\ meV$ responsible for spin-lattice relaxation in the tetragonal phase.

4.6.3 MAGNETIC HEAT TRANSPORT κ_{mag}

We now address the anisotropy in κ that develops in $CuSb_2O_6$ at $T \leq 150\ K$. Given that the spin-chain direction alternates (moving along the [001] direction) between [110] and [$\bar{1}$10], magnetic heat transport (κ_{mag}) is anticipated within the *a*-*b* planes but not along *c*. The surprising result is that $\kappa_{[100]}$ is much smaller than $\kappa_{[010]}$ and $\kappa_{[110]}$ in the range $10\ K \leq T \leq 150\ K$. The convergence of $\kappa_{[100]}$ and $\kappa_{[010]}$ at $T < 10\ K$ indicates isotropy of the *a*-*b* plane lattice thermal conductivity as would be expected based on the crystal structure. One possibility is that the resonant phonon scattering is anisotropic within the *a*-*b* plane, i.e., weaker for transport along the [010] and [110] directions, though this seems less plausible given that $\kappa_{[100]}(T)$ and $\kappa_{[001]}(T)$ are indistinguishable for $T \geq 30\ K$ as are the [100] and [010] thermal expansion coefficients [79]. An alternative hypothesis is that the enhanced κ along [010] and [110] is associated with a κ_{mag} and this contribution is preferentially suppressed along [100]. This might have its origin in the nature of the *local* 1D magnetic ordering (e.g., chain fragments) or its interplay with the

twinning Figure 4.9(a). Measurements of κ in detwinned crystals might offer a means of testing this hypothesis, but previous efforts at detwinning were not successful [28].

4.6.3.1 MAGNETIC MEAN FREE PATH l_{mag}

To examine the plausibility of our hypothesis about magnetic heat transport, we estimated κ_{mag} for the [110] and [010] directions by subtracting, from the corresponding $\kappa(T)$ curves, the data for $\kappa_{[100]}$ (using $\kappa_{[100]}$ for this subtraction would overestimate κ_{mag} at low T since our data implies a larger *a*-*b* plane lattice thermal conductivity). We then

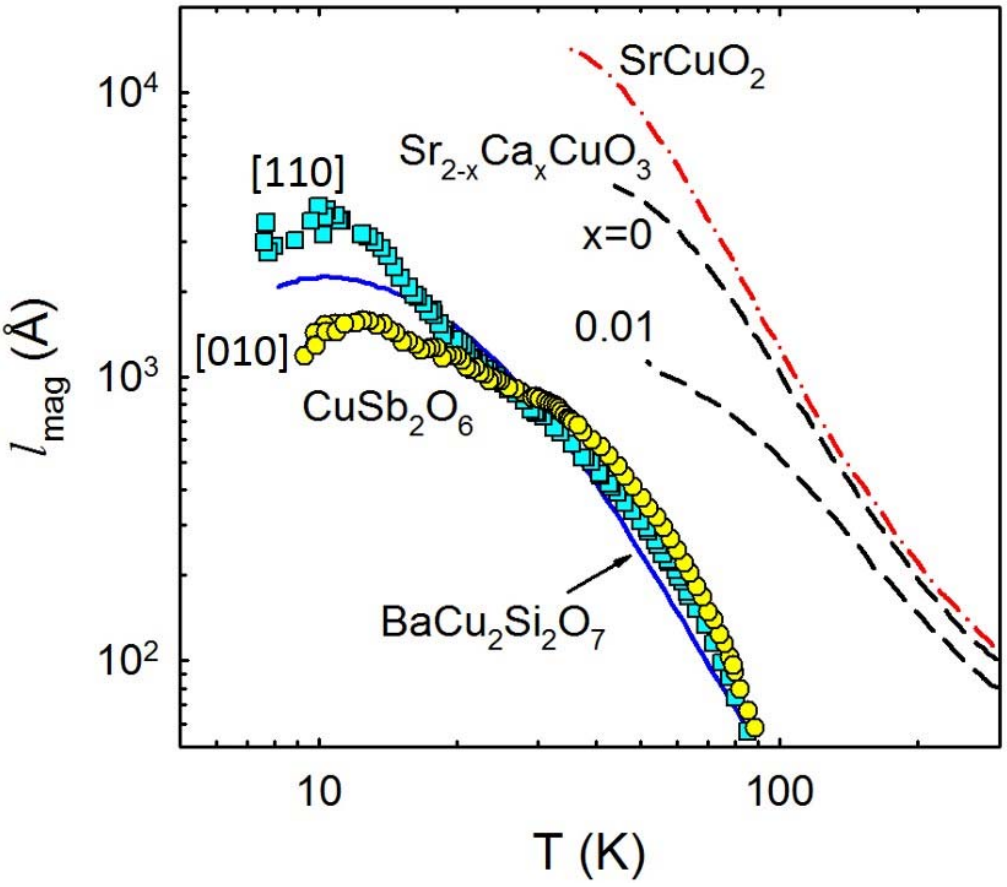

Figure 4.18 Magnetic mean-free path for [110] and [010] directions of $CuSb_2O_6$ (symbols). Also shown for comparison are results from other spin-½ chain compounds: $BaCu_2Si_2O_7$ (Ref.[13]), $SrCuO_2$ (Ref. [97]) $Sr_{2-x}Ca_xCuO_3$ (Ref. [98])

computed a mean free path, using [97], $l_{mag} = (3\hbar/\pi N_s k_B^2 T)$, where $N_s = 2/(\sqrt{2}ac)$ is the number of chains per unit area appropriate to $CuSb_2O_6$. Figure 4.18 shows the resulting $l_{mag}(T)$ for the present specimens and for comparison, those of other Q1D $s = 1/2$ chain compounds $BaCu_2Si_2O_7$ [13], $SrCuO_2$ [97], and $Sr_{2-x}Ca_xCuO_3$ [98], computed similarly. We see that l_{mag} for $CuSb_2O_6$ is similar in its T dependence and low-T magnitude ($\sim 0.1-0.3\ \mu m$) to that of $BaCu_2Si_2O_7$, suggesting a universal behavior (when suitably scaled by J) for $s = 1/2$ chain systems as noted previously [13].

4.7 CONCLUSION AND SUGGESTED FUTURE WORK

In this chapter thermal conductivity $\kappa(T)$ studies of $CuSb_2O_6$ and $ZnSb_2O_6$ were presented. Lattice parameter determination, study of bicrystallinity and twinning, and their effect on thermal conductivity were also included. Highly suppressed $\kappa(T)$ observed in the bicrystalline sample was as expected because of substantial scattering of phonon at domain boundaries. Effect of structural change and associated twinning on $\kappa(T)$ was not observed at room temperature and above. More important, this study reveals two main findings: first, strong phonon-spin resonant scattering in the $CuSb_2O_6$ which is associated with the onset of short range Q1D antiferromagnetic order at $T \leq 150\ K$, second a magnetic contribution to heat conduction consistent with that found in the other low dimensional spin systems. Regarding the magnetic contribution, the anisotropy in $\kappa(T)$ at $T \leq 150K$ can be argued to the anisotropy in resonance scattering but this scenario seems less plausible given that the linear thermal expansion shows no in-plane anisotropy. Also, the scattering resonance energy $\sim 100K$ is consistent with the energy splitting of a two level Schottky model that describes the magnetic contribution to the specific heat and linear thermal expansion coefficients.

Every research project has some limitations whether it be a time frame or availability of resources or something else, and cannot address the problem from all aspects. This thesis also did not cover all aspects of the research problem in these compounds for various reasons. Some of these are suggested for future work: 1) Low temperature measurements of thermal conductivity has not been done yet, and because of spin flop transition on $CuSb_2O_6$ with field of $1.25\ T$ along *b*- direction, it is interesting to see its effect on thermal conductivity, 2) the nature of excited state which more likely involve spin and lattice perturbations remains to be established, 3) measurements of $\kappa(T)$ in detwinned crystal might give further insight into the anisotropy in $\kappa(T)$ along $[100]$ and $[010]$ directions. These problems seems challenging as well as interesting for future work.

CHAPTER V

QUASSI-1D TWO-LEG LADDER COMPOUND $BiCu_2PO_6$

In similar manner to previous chapter, I will first discuss motivation behind the study of this compound. Next, crystal structure and magnetism in $BiCu_2PO_6$ (BCPO) will be described to understand the possible role of lattice and magnetic structure in heat transport. Then, I will present thermal conductivity measurements on the single crystals of BCPO in all principle crystallographic directions. Model fitting of $\kappa(T)$ data and analysis of results will be included.

5.1 MOTIVATION

$BiCu_2PO_6$ (BCPO) is another compound with exchange coupling energy less or comparable to Debye temperature, i.e., ($J \leq \theta_D$). This material is of special interest because being a spin-½ ladder it serves as the bridge between one dimensional spin chain and two dimensional magnetic systems. It is quite possible that improved understanding of spin ladders will help a better understanding of 2D magnetic systems. Moreover, the frustration introduced by the next-nearest neighbor interaction makes this material rich for possible exotic ground states and physical phenomenon, which may not be observed in a regular two leg ladders. Therefore, this compound serves in two ways: 1) provides opportunity to further explore $J \leq \theta_D$regime, and 2) adds an extra flavor because of its different spin structure and resulting physics.

We present the study of heat conduction in BCPO which has exchange energy, $J_1 \approx 80 - 130\,K$ along the leg of ladder. The study shows that BCPO exhibits resonant phonon-spin scattering as well as an additional contribution to κ along the leg of a spin ladder throughout the temperature range attributable to spin heat conduction.

5.2 GROWTH, STRUCTURE AND MAGNETISM

Single-crystals $BiCu_2PO_6$ used in this work are grown by our collaborator at Montana State University. I will outline the growth process in brief [99]. Single crystals of $BiCu_2PO_6$ were grown by the optical-floating-zone technique. First, a polycrystalline sample was prepared through the solid-state reaction method. Stoichiometric amounts of Bi_2O_3, CuO, and H_3PO_3 were mixed and ground together. The powder was calcined at 160, 300, 500, and 750℃ in air for 15 hours each, then, reground, and reacted at 820℃ for 24 hours. Second, the resultant materials were compacted with the hydrostatic pressure into rods of 4 mm diameter and 120 mm length. The polycrystalline rods were sintered six times at temperatures between 820 and 845℃ for 30 hours in air in order to increase their density. Finally, these rods were used to grow single crystal of $BiCu_2PO_6$ in an optical-floating-zone furnace, model SCI-MDH-20020 from NEC. Crystal growth was conducted in air, at 5.5 atm pressure, 3 mm/hour growth rate, 15 rpm counter-rotation, and lamp power of 115 W (using 1000W lamps). The crystal grew along [010] direction.

The crystal structure of BCPO is shown in Figure 5.1. It crystallizes in orthorhombic structure with space group *Pnma* and lattice parameters $a = 11.776$ Å, $b = 5.1776$ Å, $c = 7.7903$ Å [100]. The unit cell consists of four formula units. In *bc*-plane two copper cations occupy two crystallographic sites Cu1 and Cu2 and each copper is surrounded by four nearest oxygen thus forming a distorted planar CuO_4 plaquette (green

and brown in Figure 5.1). Two CuO_4 plaquettes are linked by sharing O2-O2 oxygen bond (see Figure 5.2 left panel) and thus forming the Cu-based dimer unit. The two neighboring dimers units [Cu_2O_8] share the corners via O1 while the next–nearest–neighbor dimers are further linked by diamagnetic PO_4 tetrahedra. Thus, with inclusion of Bi ions group it forms an entire crystal structure framework.

The arrangement of dimers produce the zig-zag ribbons of Cu^{2+} ions which runs along the crystallographic *b* direction. Interactions of two inequivalent copper ions Cu1 and Cu2 are mediated via nearest-neighbor (NN) antiferromagnetic exchange J_1 and next-

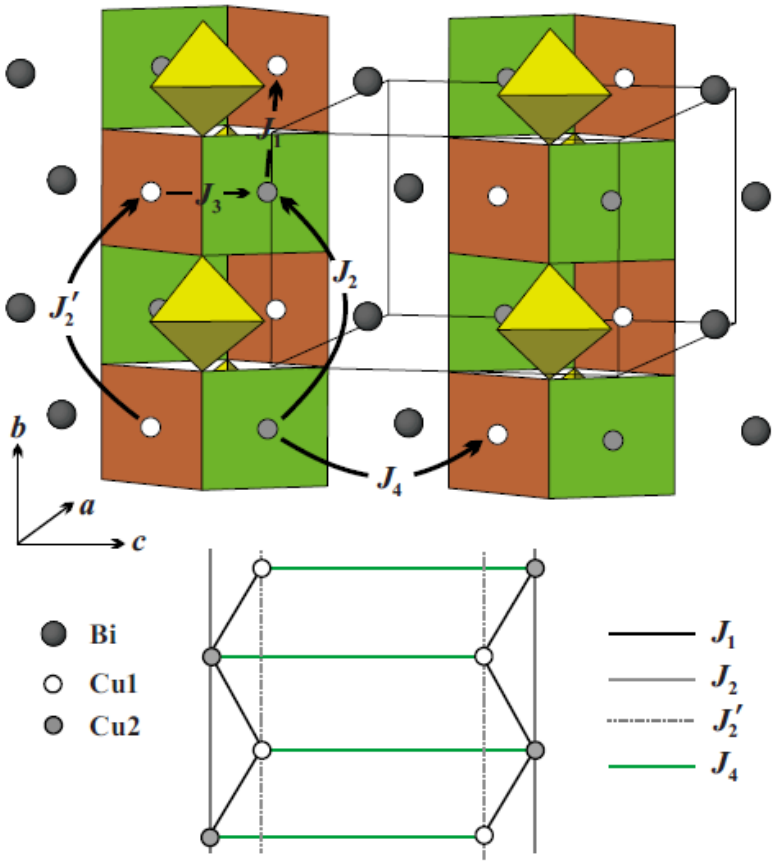

Figure 5.1 Crystal Structure of $BiCu_2PO_6$ consists of ribbons of CuO_4 plaquettes and PO_4 tetrahedra (yellow). Two crystallographically inequivalent Cu positions (Cu1 and Cu2) are shown in open and shaded circles whereas larger dark circle represent the Bi atoms. The lower panel shows the ladder scheme involving zig-zag chains on different structural ribbons[102].

nearest-neighbor (NNN) antiferromagnetic exchange J_2. The zig-zag nature of J_1 gives the frustration to a spin chain whereas inequivalent position of the Cu ions leads to an inequivalent NNN coupling J_2'. These chains are coupled along *c* axis by rung coupling J_3 and J_4 [101]. Figure 5.3 shows the schematic of exchange coupling in BCPO.

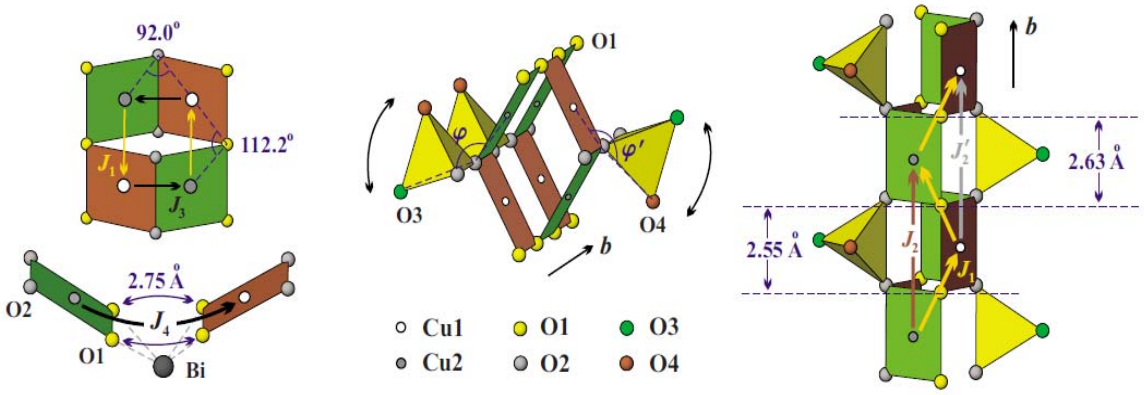

Figure 5.2 Different segments of BCPO crystal structure showing: [Left panel] the superexchange pathways, and linkage of dimers unit to nearest neighbor dimmer units, to form a zig-zag ribbon, [middle panel] different position of PO_4 tetrahedra for J_2 and J_2' couplings, and [right panel] spin frustration and difference in distance of O1-O1 for J_2 and J_2'. Figure from ref.[102].

The appropriate spin model of BCPO remains controversial because of its complex crystal structure. Koteswararao *et al*.[100] have considered spin model of BCPO as a $J_1 - J_3$ ladder with leg coupling J_1 and rung coupling J_3 and such ladders are further coupled by the inter-ribbon coupling J_4. This model predicts the value of exchange coupling as J_1/k_B= $J_3/k_B \sim 80K$ and $J_4/J_1 \sim 0.74$. Mentre *et al*.[101] have included the NNN coupling J_2 as a leg-coupling in addition to NN leg-coupling J_1, and then, J_4 is redefined as the rung coupling suggesting the BCPO as a frustrated spin ladder with J_3 as an inter-ladder coupling. This model has suggested the coupling parameters as $J_1/k_B = 137.8K, J_2/k_B = 73.3K$, and $J_4/k_B = 58.4K$ but, has neglected J_3 in the calculation which introduces some

discrepancies in the fitting of the magnetic susceptibility data. Tsirlin *et al*.[102] have made some improvement on previous model and also included J_2' in the calculation. Despite having similar superexchange pathways J_2 and J_2' differ significantly in magnitude due to difference in O1-O1 bond length and in the arrangement of diamagnetic PO_4 tetrahedra as shown in Figure 5.2 (right panel). Despite of the agreement on the relevance of inter-ladder coupling J_3 for the full picture of spin model, this model finds that it is challenging to include J_3 in the calculation. Recently, Plumb *et al*.[103] have measured spin excitation spectrum in BCPO via inelastic neutron-scattering (INS) and suggested the spin model of a $J_1 - J_2 - J_4$ two-leg ladder with inter-ladder exchange J_3. Plumb *et al.* have also suggested to include anisotropic interaction to mitigate the discrepancies in the model results and the data. In summary, it seems more plausible that J_1, J_2, J_2', J_3 and J_4 along

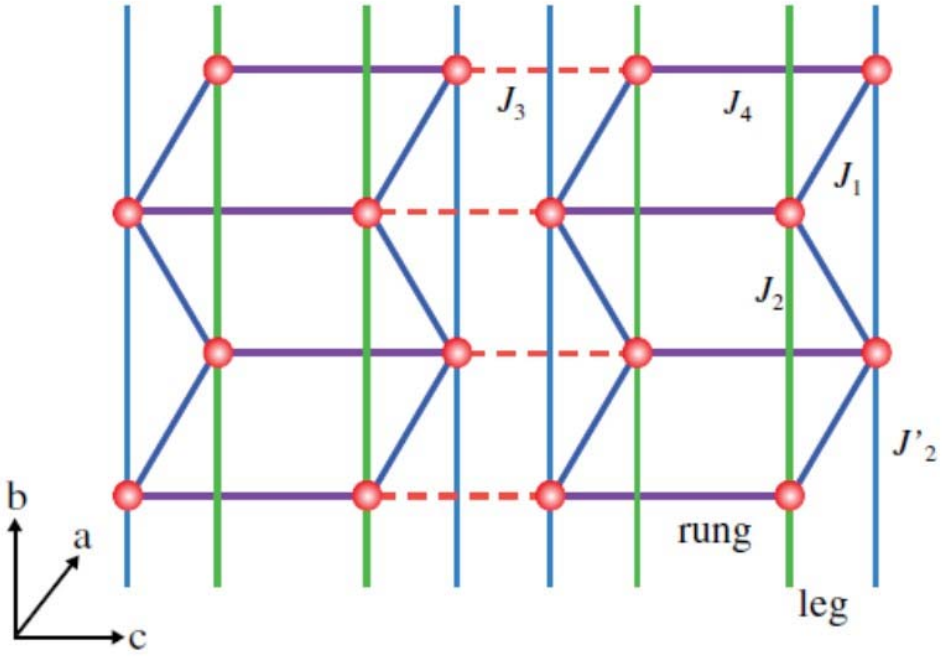

Figure 5.3 Schematic of exchange coupling in BCPO. It shows BCPO is frustrated $J_1 - J_2 - J_4$ ladder with weaker interladder coupling J_3. From [105] .

with strong anisotropic interaction is required to completely describe microscopic spin model of BCPO.

Susceptibility $\chi(T)$ measurement implies the spin gap of $\Delta{\sim}35K$ in BCPO which is consistent with the gap obtained from the fitting of magnetic heat capacity $C_m(T)$ [100]–[102]. Different from this, study of spin excitation spectra by inelastic neutron diffraction [103] shows two branches of excitation spectra along leg of ladder direction with two spin gap $\Delta_1{\sim}22.0\,K$ and $\Delta_2{\sim}45.8\,K$ but average of these two gap is consistent with the gap obtained from $\chi(T)$ and $C_m(T)$.

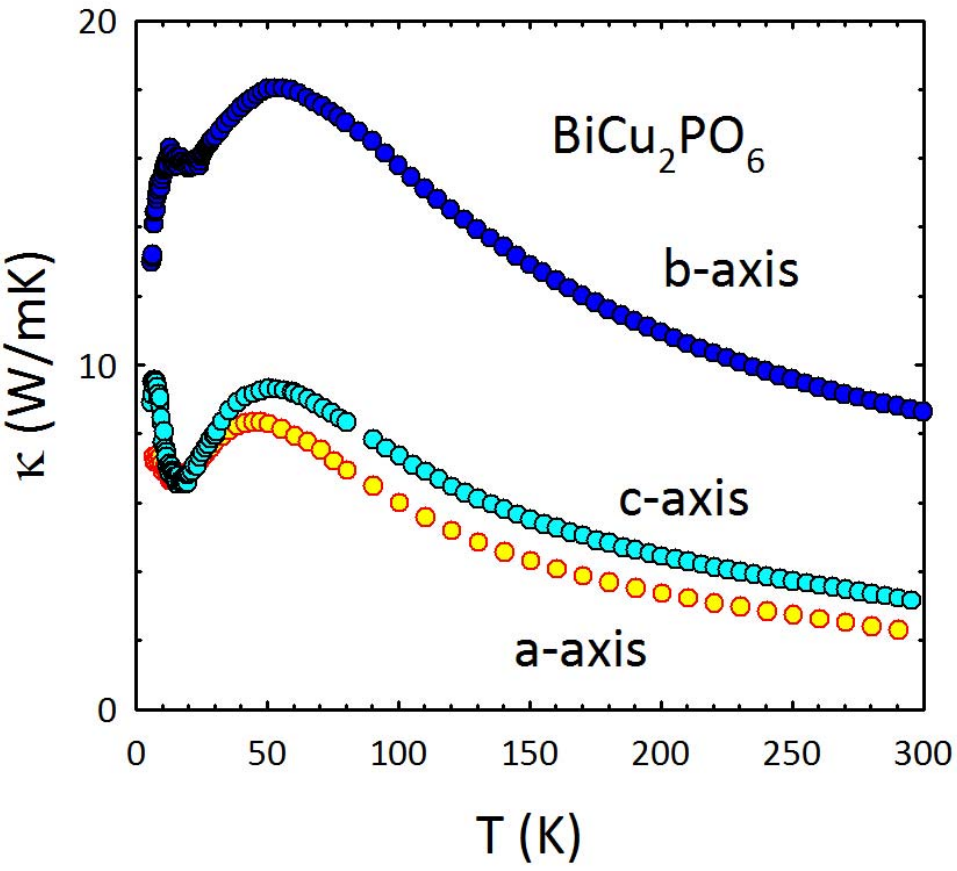

Figure 5.4 Thermal conductivity $\kappa(T)$ of single crystals of BCPO with heat flow along the directions indicated in figure.

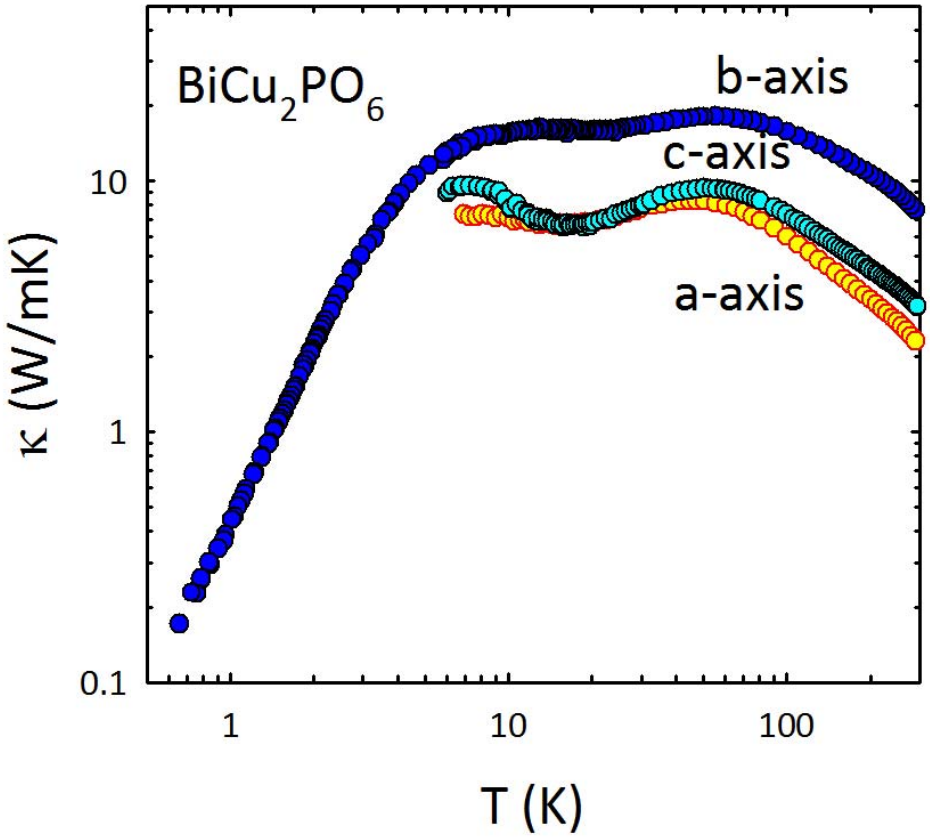

Figure 5.5 Thermal conductivity in log-log scale along leg of lader direction, $\kappa_b(T)$, measured down to 0.5 K. The line shows the nearly T^3 dependence of $\kappa(T)$ at very low temperature.

5.3 RESULTS FROM $\kappa(T)$ MEASUREMENTS

5.3.1 THERMAL CONDUCTIVITY OF $BiCu_2PO_6$

For BCPO thermal conductivity (κ) was measured with heat flow along all three principal crystallographic directions. Figure 5.4 shows the thermal conductivity of BCPO for various crystallographic directions for $5\ K \leq T \leq 300\ K$. Thermal conductivity $\kappa(T)$ shows three important features: (1) κ is much larger throughout the T range along leg of the ladder (b-axis) direction as compared to, rung of the ladder (c-axis) and perpendicular to plane of the ladder (a-axis), (2) along all three directions $\kappa(T)$ exhibits a dip like feature

at ~20 K but the magnitude of dip along a- and c-directions is significantly bigger, (3) the broad peak in $\kappa(T)$ along all three directions is consistent with the peak in susceptibility, $\chi(T)$, at T~$55-60\ K$ [100], [102]. Because of much higher magnitude of $\kappa(T)$ along b axis and availability of longer crystals in that directions, we extended $\kappa(T)$ measurements down to 0.5 K in separate ^{3}He probe. The Figure 5.5 in log-log scale includes $\kappa_b(T)$ all the way down to $0.5K$. At very low T, $\kappa_b(T)$ follows $T^{2.6}$. Phonon mean free path calculated using simple kinetic expression $\kappa\sim\frac{1}{3}Cvl$ with C from non-magnetic analog $BiZn_2PO_6$ and $\kappa(T)$ from experimental data shows maximum phonon mean free path l_{ph}~$0.58\ \mu m$. Presence of dip like feature in all three directions is more obvious with log-log scale as shown in Figure 5.5.

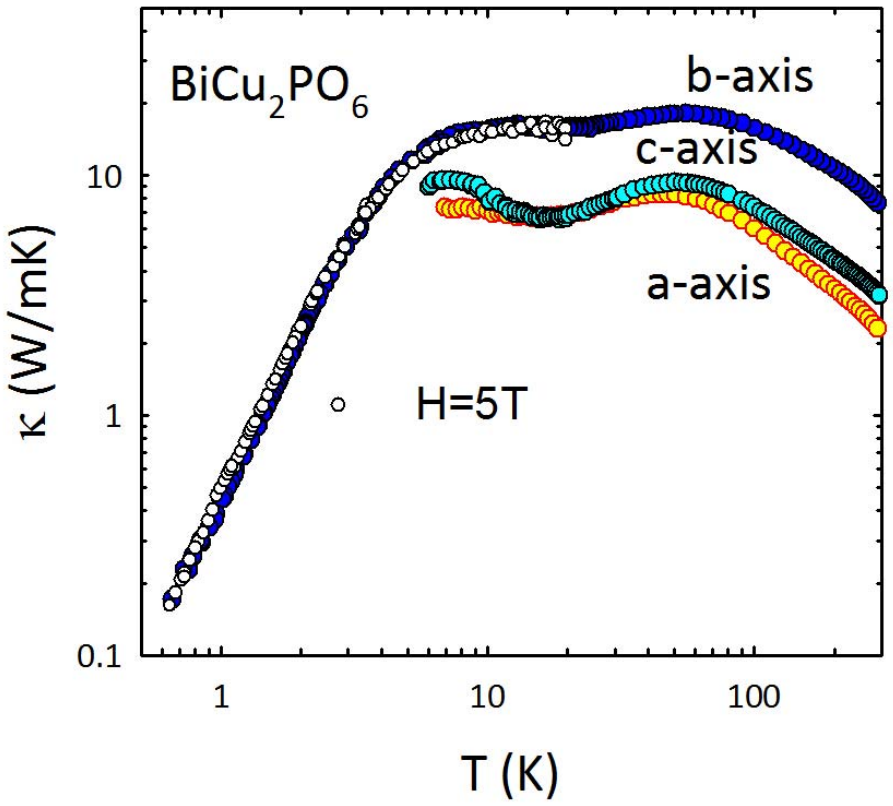

Figure 5.6 Thermal conductivity at $5\,T$ along leg of the ladder direction $\kappa_{mag,b}(T)$ (unfilled circle) matches with zero field data (filled blue circle) $\kappa_b(T)$. Also included are a- and c-axis data for reference.

5.3.2 MAGNETIC FIELD DEPENDENCE OF $\kappa(T)$

We have measured $\kappa(T)$ in a 5 T magnetic field with field orientation and direction of heat flow both along the spin chain direction (b- axis). There was no magnetic field dependence of κ up to 5 T as shown in Figure 5.6. As discussed in section 4.5.2, magnetic field can have effects of both suppression and enhancement of κ in the magnetic systems depending on the mechanism involved in the scattering processes. No magnetic field dependence implies that either magnetic system does not involve in the scattering process in that temperature range or the field is not enough to change the gap in the system, i.e., to change the number of excited quasi-particles. In our case, we believe later one makes sense as $C_m(T)$ indicates the significant magnetic contribution at least in the range of $5\ K \leq T \leq 55\ K$. Recently, we also came to know the suppression of low-T peak in $\kappa(T)$ of BCPO with the field higher than 10 T [104].

5.4 ANALYSIS OF RESULTS FROM $\kappa(T)$ MEASUREMENTS

5.4.1 PHONON-SPIN RESONANT SCATTERING

We first consider the source of scattering which is responsible for the obvious suppression of $\kappa(T)$ at $T \sim 10\ K - 30\ K$ region. Such dip like features are the signature of resonant scattering in which heat-carrying phonons are strongly damped over a restricted frequency range as seen previously on $CuSb_2O_6$. Given the suppression of κ is evident in all three directions, we believe it should be relatively isotropic but it is less pronounced along leg of ladder direction because of higher magnitude of κ in that direction relative to a- and c- directions. Therefore, analogous to mechanism introduced in [91], interaction should be between phonons and localized spin states rather than dispersive states. Presence of resonancelike singlet bound mode at $E = 24\ cm^{-1}$ has been suggested by Raman

scattering study (inelastic light scattering) of BCPO [105]. Energy of these bound singlet states in Kelvin scale ~36 K is almost equal to singlet triplet gap (Δ~35 K) inferred from thermodynamic measurements [106]. Therefore, these bound singlets should act as the scattering centers for resonant scattering of phonons.

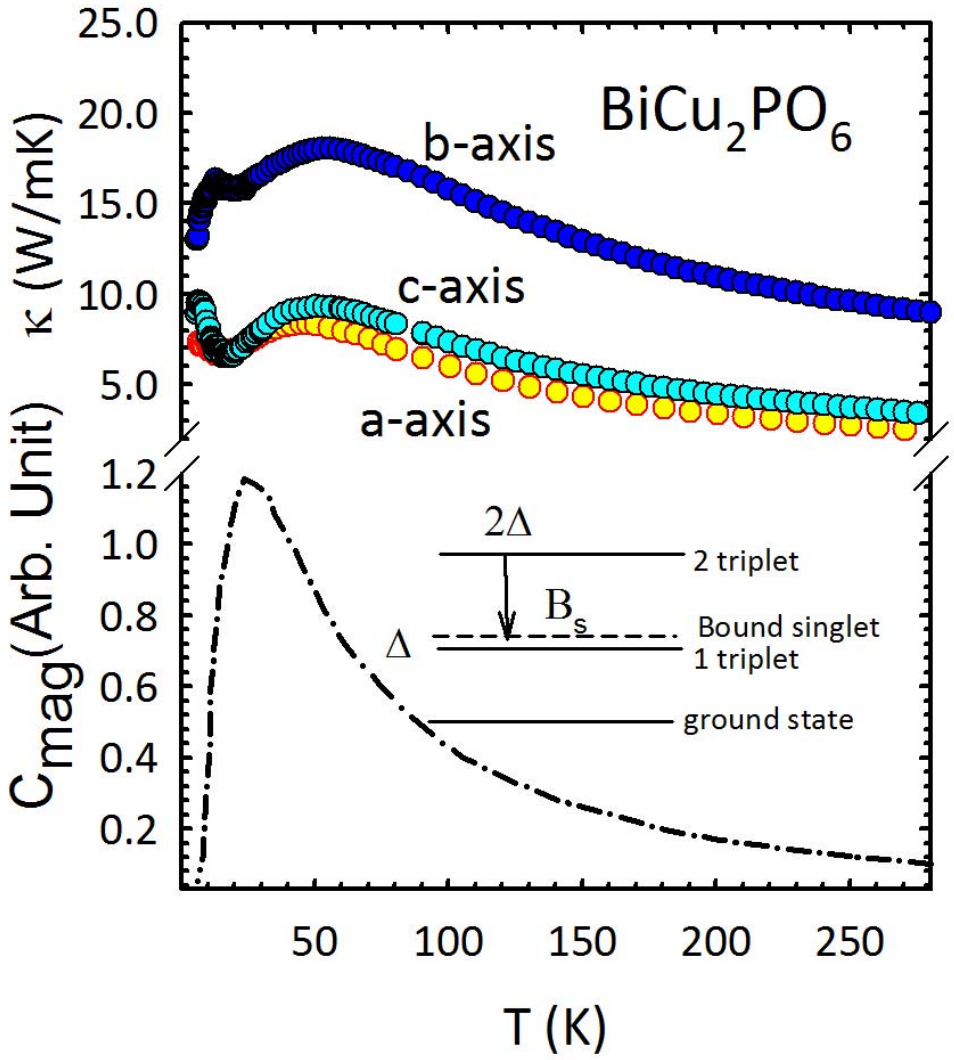

Figure 5.7 Comparison of temperature dependence of thermal conductivity $\kappa(T)$ (upper panel) and magnetic specific heat $C_{mag}(T)$ (lower panel). Dip in $\kappa(T)$ coincides with peak of $C_{mag}(T)$[105] . Inset shows the energy level scheme relevant to this compound.

Further understanding of resonant phonon-spin scattering can be obtained by looking into the magnetic heat capacity $C_m(T)$ which is obtained by fitting magnetic

scattering to intensity of quasielastic scattering and using $C_m(T) \propto I_{QE}(T)/T^2$ as shown in Ref. [105]. Figure 5.7 shows magnetic specific heat (lower panel) and thermal conductivity (upper panel). Two features are evident in Figure 5.7. The rise in C_{mag} at higher-T is analogous with the anisotropy in $\kappa(T)$. The maximum in the magnitudes of C_{mag} at $T \approx 20\,K$ coincide with the "dip" in $\kappa(T)$ noted above for all three directions. The maximum in C_{mag} is analogous to Schottky anomalies for two level system and fitting to C_{mag} by $C_{mag} \propto T^{-3/2}e^{-\Delta/T}$ throughout the temperature range gives the characteristic gap, $\Delta \sim 36\,K$ [105]. Therefore, the resonance like phonon scattering evidenced in $\kappa(T)$ involves phonon-induced excitations of singlets and triplets states with energy scale of $\sim 35\,K$ resulting into bound singlet states (see inset of Figure 5.7).

5.4.2 MODELING OF $\kappa(T)$

To quantify the resonant phonon spin scattering and magnetic anisotropy, we utilized Callaway model [64] as described in section (4.6.2). For the sake of easiness to the reader, I will rewrite that equation again as,

$$\kappa = \frac{k_B}{2\pi^2 v}\left(\frac{k_B}{\hbar}\right)^3 T^3 \int_0^{\theta_D/T} \tau(\omega, T)\frac{x^4 e^x}{[e^x - 1]^2}\,dx, \tag{5.1}$$

with

$$\tau(\omega, T)^{-1} = \frac{v}{L_b} + A\omega^4 + BT\omega^2 e^{-\frac{\theta_D}{bT}} + C\omega^2 \tag{5.2}$$

and

$$\tau_{res}(\omega, T)^{-1} = R\frac{\omega^4\,\Delta^4}{(\Delta^2 - \omega^2)^2}F(T). \tag{5.3}$$

Eq. (5.2) contains phonon scattering terms representing boundaries, point defects, and Umklapp processes, respectively. Additional term $C\omega^2$, which represents the scattering by sheet like fault, was introduced to account for height of low T peaks of $\kappa(T)$. Presence of such defects in this compound remains to be established. In the resonance scattering term

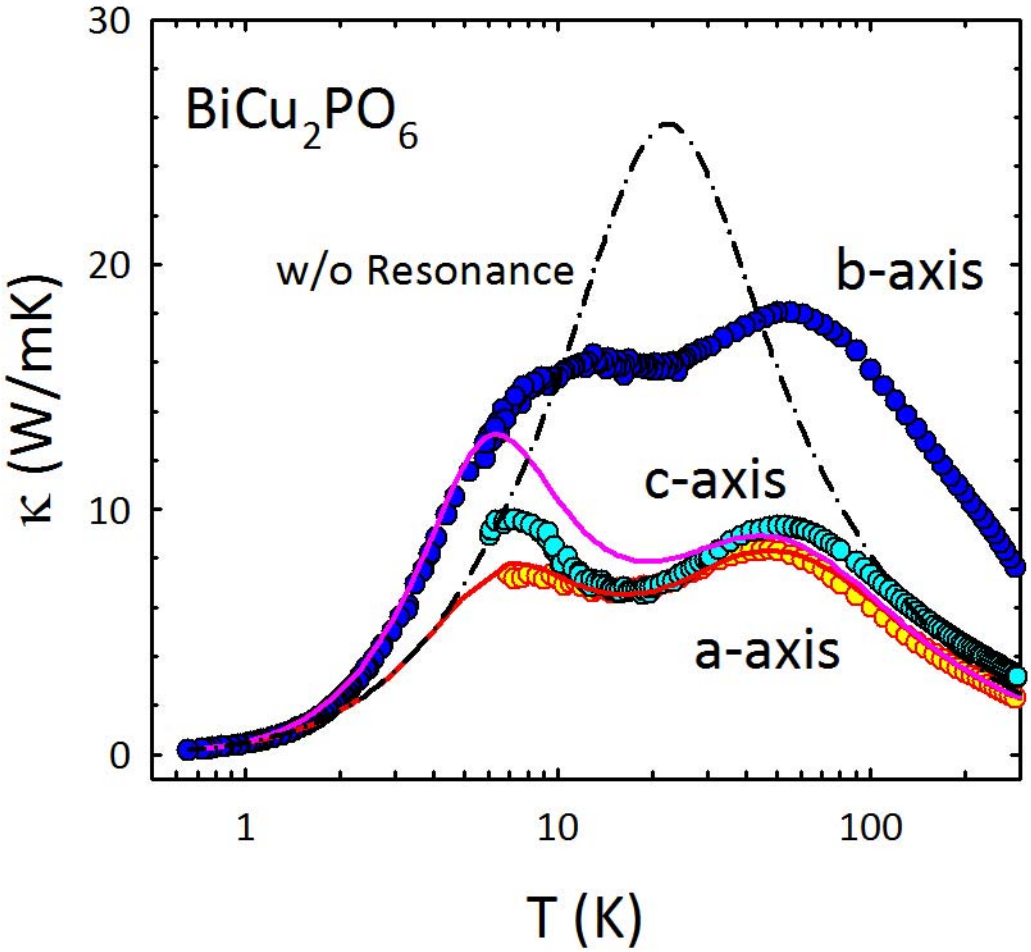

Figure 5.8 Model fitting to κ_a of BCPO. Parameters of the fitting are given in Table 5.1. Dash dot curve shows magnitude of κ_a in absence of resonance scattering. Pink (higher in magnitude) solid curve is a fit to $\kappa_b(phonon\ only)$ with same parameters of κ_a (red curve) fit except C to match up with low T peak (which is a phonon peak).

Eq. (5.3), conventional gap symbol in unit of frequency is used such that in unit of kelvin, $\Delta = \hbar\omega_0/k_B$. We used the same population $F(T)$ of two level system as described in section (4.6.2). First, we fitted κ_a to Eq. (5.1) in combination with Eq. (5.2) and (5.3). During the fit, Debye temperature ($\theta_D \sim 330\ K$) [106] and hence phonon velocity (v), energy difference in the two level system ($\Delta \sim 35\ K$), and L_b minimum dimension of the sample were kept constant. Thus, we were able to produce reasonable fit to κ_a by varying the fit parameter A, B, C, F and b. Figure 5.8 shows the result of fitting and parameters are

shown in Table 5.1. To see the effect of resonance scattering, we turned it off ($R = 0$), and the resulting dash dot curve shows the magnitude of $\kappa_a(T)$ without resonant scattering. Although, it suppressed κ_a nearly throughout T range, it's effect was very significant at $T \sim 10 - 30K$.

In absence of magnetic contribution to heat transport, κ_{ph} should be isotropic at least at higher temperature where impurity or disorder does not play significant role. Different peak heights at low-T correspond to sheet like defects. Therefore, we kept all parameter from the fit of κ_a same except C to match low-T peak of κ_b. Result of this fit is the pink solid line (higher magnitude) in Figure 5.8. We believe this is the genuine phonon thermal conductivity κ_{ph} along the b-direction. We name it as $\kappa_{b(ph)}$, to make it easier to use later.

Table 5.1 Parameter values for fitting to κ_a and $\kappa_b(ph)$(see text) of BCPO

Fitting to	$B(sK^{-1}) \times 10^{-17}$	b	$v(kms^{-1})$	$A\ (s^3) \times 10^{-43}$	$C(s^2) \times 10^{-17}$	$R(s^3) \times 10^{-40}$
κ_a	1.80	4.7	2.53	4.08	5.89	2.17
$\kappa_{b(ph)}$	1.80	4.7	2.53	4.08	2.15	2.17

5.4.3 MAGNETIC HEAT TRANSPORT κ_{mag}

Anisotropy in $\kappa(T)$ is another important feature of BCPO which is consistent with the anisotropy of spin excitation spectra from inelastic neutron scattering (INS) study [103]. Highly dispersive excitation spectra along the *b*-direction, (i.e., leg of the ladder) small dispersion along *c*-direction, (i.e., rung of the ladder) and no dispersion along *a*-direction, (i.e., perpendicular to plane of the ladder direction) is consistent with the

magnitude of κ_b , κ_c ,and κ_a respectively. Even if we dismiss the smaller anisotropy in between κ_a and κ_c attributing it to the uncertainty in the measurements, much bigger anisotropy with κ_b deserves some explanations. We believe, it is because of the magnetic contributions to heat transport. A counter argument to it could be the anisotropy in the phononic part in the crystal but it is less plausible given the crystal structure of BCPO. Having *bc* as the plane of ladder and *a* perpendicular to the plane of ladder (*bc* planes are separated by PO_4 tetrahedra along *a*-direction), obvious anisotropy seems to be in between in plane (κ_b , κ_c) and out of plane (κ_a) directions. It should not be within the plane of ladder (κ_b and κ_c). On the other hand, κ_c (in plane) and κ_a (out of plane) have almost similar magnitude. Based on this observation in combination with the magnetic anisotropy from INS study, the scenario of significant phonon anisotropy in BCPO is unlikely. Similar double peak structure with small anisotropy in the case of two-dimensional spin-dimer system $SrCu_2(BO_3)_2$ is explained based on the only phonon contribution to heat transport. However, in contrast to BCPO, SCBO has very flat dispersion of magnetic excitation spectra indicating almost null magnetic contribution to heat current in that system.

To get the estimate of the upper limit (would be smaller in case of small anisotropy in genuine phonon conductivity) of magnetic contribution to heat transport, we subtracted phonon contribution, i.e., $\kappa_{ph} \approx \kappa_{b(ph)}$ (calculated from fit) from total heat transport along the leg of ladder such that $\kappa_{mag} \approx \kappa_{Tot}(\kappa_b) - \kappa_{b(ph)}$. Figure 5.9 shows κ_{mag} as a function of temperature. The κ_{mag} has maximum magnitude of $\sim 9.5\ W/mK$ at $T \sim 80\ K$ and interestingly this temperature coincides with the leg coupling energy ($J \sim 80\ K$) as suggested by Orignac *et al.* [107] for one dimensional spin gap system. Orignac *et al.* [107] have suggested that for spin half ladder without impurity, $\kappa_{mag} \sim \frac{e^{-\Delta/T}}{\sqrt{T}}$ for $T \ll \Delta$, $\kappa_{mag} \sim T$

for $\Delta < T < T_{peak}$, where T_{peak} is temperature of maximum κ_{mag}, and $\kappa_{mag} \sim T^{-2}$ for high T. But for spin half ladder with multiple impurity, $\kappa_{mag} \sim e^{-\Delta/T}$ for $T \ll \Delta$, $\kappa_{mag} \sim T^{-2}$ at high T and no prediction for intermediate temperature. All the real crystals have some level of impurity. Prediction of $\kappa_{mag} \sim e^{-\Delta/T}$ below spin gap temperature from this study [107] is another interesting behavior followed by κ_{mag},and the value of the gap estimated from fitting (see Figure 5.9 inset), $\Delta \approx 30\ K$ is in ballpark to the spin gap suggested by other

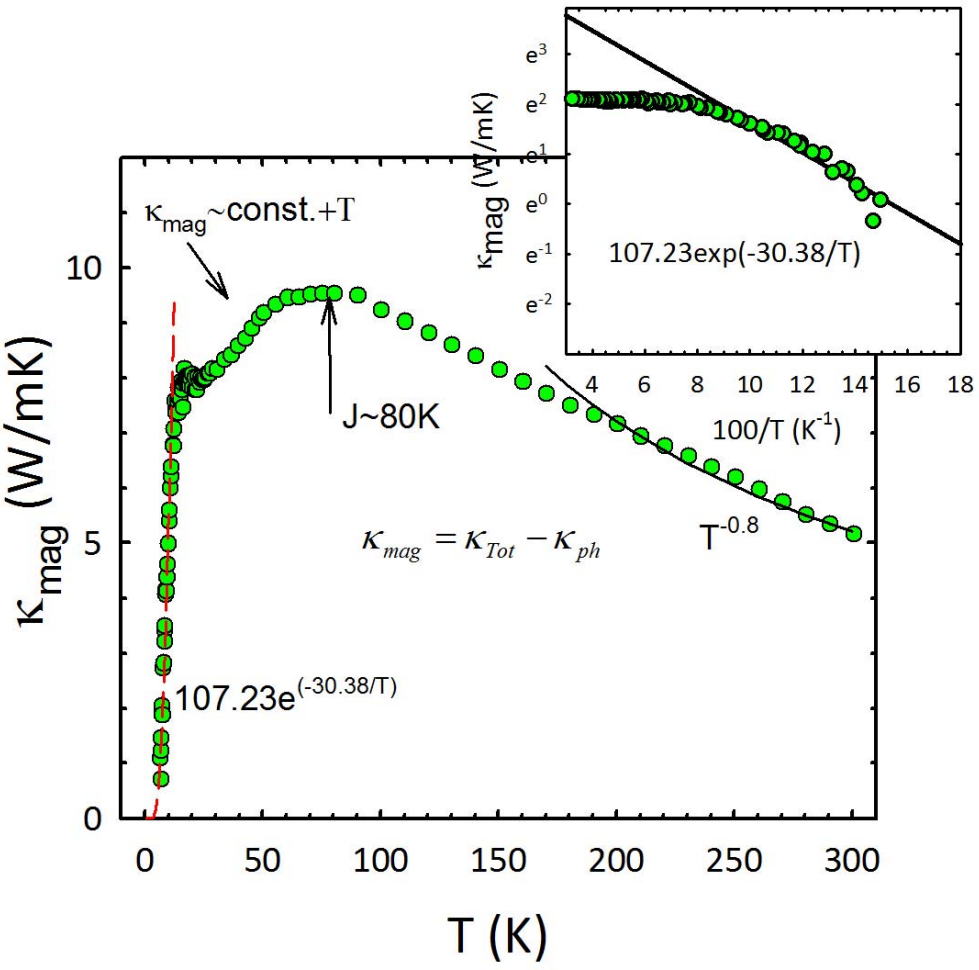

Figure 5.9 Inferred magnetic contribution to heat transport $\kappa_{mag}(T)$ in BCPO which has a peak at $\approx 80\ K \sim J_{leg}$. Dashed line at low T is fit to data such that $\kappa_{mag} \sim e^{-\Delta/T}$,with $\Delta \approx 30\ K$ in ballpark to spin gap of the system. Inset gives a close look to fitting. Below peak and above Δ, $\kappa_{mag} \sim constant + T$ and at high temperature $\kappa_{mag} \sim T^{-0.8}$.

studies [102], [106]. Although, it is suggested to be generic behavior of one dimensional spin gap systems, we should remember that those predictions were made keeping $J \gg \theta_D$ in mind. Our data shows that at intermediate temperature, i.e., above spin gap and below peak, $\kappa_{mag} \sim constant + T$ and at much higher temperature, $\kappa_{mag} \sim T^{0.8}$ as shown in Figure 5.9. At high T, our data do not obey the exact prediction of Orignac et al.[107], $\kappa_{mag} \sim T^{-2}$. Obvious reason could be the different energy scale $J \leq \theta_D$ in this sample from that considered in the theoretical work, $J \gg \theta_D$. Also, scattering from phonon, which is very important at intermediate and higher temperature, has not been included in the theoretical work [107].

5.4.3.1 MAGNETIC MEAN FREE PATH (l_{mag})

To explore the magnetic heat transport in BCPO, we calculated magnetic mean free path using the resulted magnetic thermal conductivity (κ_{mag}) from previous section and the relation [10] given by,

$$\kappa_{mag} = \frac{N_s {k_B}^2}{\pi\hbar} l_{mag} T \int_{\frac{\Delta}{k_B T}}^{\frac{\varepsilon_{max}}{k_B T}} \frac{x^2 e^x}{[e^x - 1]^2} dx, \tag{5.4}$$

where, N_s is the number of spin ladders per unit area, ε_{max} is the band maximum of magnon energy, and Δ is the spin gap. For BCPO, $N_s = 2/ab$ gives the number of spin ladders per unit area. Then, we used previously determined κ_{mag}, Δ, and $\varepsilon_{max} = 16meV$ from inelastic neutron scattering [103] to calculate $l_{mag}(T)$as shown in Figure 5.10. At room temperature, $l_{mag} \sim 200$Å and at low T $(\sim 10K)$, $l_{mag} \sim 4000$Å. From room temperature to intermediate temperature, T-dependence of l_{mag} becomes weak and then all the way down to lowest T, it is strongly temperature dependent. At RT, its magnitude is comparable to other spin half ladder compound with, $J \gg \theta_D$ [10], [108] and at low-T it is comparable to

spin half chain compound with, $J \leq \theta_D$ [13], [76]. Possible reasons for this crossover between two regimes could be:1) ineffectiveness of the temperature independent l_{mag} model at higher temperature of this low-J compound and 2) magnetic mean free path is independent of types of system, (i.e., whether the chain or the ladder) but dependent on value of J.

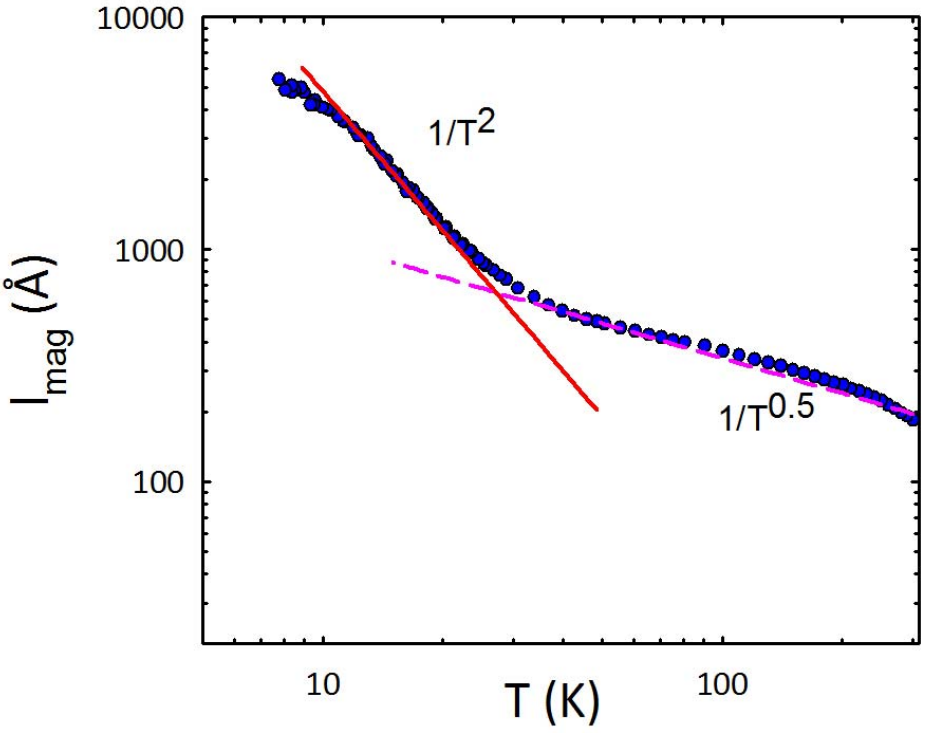

Figure 5.10 Magnetic mean free path $l_{mag}(T)$ calculated using κ_{mag} and Eq. (5.4). Solid (red) and dashed (pink) line show the temperature dependence of l_{mag} at low and higher temperature respectively.

5.4.4 CONCLUSION AND SUGGESTED FUTURE WORK

In this chapter, I presented thermal conductivity $\kappa(T)$ study of $BiCu_2PO_6$, another quasi-one-dimensional magnetic compound with $J \leq \theta_D$ but with spin-½ ladders instead of spin ½ chain. This study reveals two important features. First, strong phonon-spin resonant scattering centered on $\sim 20\ K$ was evident in double peak structure of $\kappa(T)$ along

all three crystallographic directions. Modelling of $\kappa(T)$ with the resonance scattering from two level (singlet triplet splitting) system with energy difference of $\sim 35\ K$ (consistent with gap found from other study) produced good agreement with the experimental data. Second, anisotropy in $\kappa(T)$ due to magnetic contribution to heat conduction is consistent with the results of other low dimensional spin systems. Calculated magnetic thermal conductivity by subtracting phonon contribution shows an activation behavior at low-T and the fitting to data with $\sim e^{-\Delta/T}$ gives the value of Δ comparable to that obtained from thermodynamic studies [102], [106].

Again, similar to previous project of $CuSb_2O_6$, we did not cover all aspects of this research problem for various reasons. Some of these are suggested for future work: 1) comparison of thermal conductivity with non-magnetic analog $BiZn_2PO_6$ could shed more light on anisotropy in $\kappa(T)$, 2) measurement of thermal conductivity on the doped BCPO would give further insight into the role various scattering mechanism, and 3) magnetic field dependence of $\kappa(T)$ in a field up to 5T was insufficient to see any effect, so measurement of $\kappa(T)$ in higher field could differentiate contribution of phonon and magnon as heat carriers.

REFERENCES

[1] H.-J. Mikeska and A. K. Kolezhuk, "One-dimensional magnetism," *Quantum Magn. Lect. Notes Phys.*, 2005.

[2] T. Giamarchi, "Theoretical framework for quasi-one dimensional systems.," *Chem. Rev.*, vol. 104, no. 11, pp. 5037–56, Nov. 2004.

[3] L. D. Faddeev and L. Takhtajan, "What is the spin of a spin wave?," *Phys. Lett. A*, vol. 85A, no. 6,7, pp. 375–377, 1981.

[4] F. D. M. Haldane, "Continuum dynamics of the 1-D Heisenberg antiferromagnet: identification with the O(3) nonlinear sigma model," *Phys. Lett. A*, vol. 93, no. 9, pp. 464–468, Feb. 1983.

[5] C. Hess, "Heat conduction in low-dimensional quantum magnets," *Eur. Phys. J. Spec. Top.*, vol. 151, no. 1, pp. 73–83, Dec. 2007.

[6] H. Miike and K. Hirakawa, "Evidence of the diffusive thermal conduction in a one-dimensional antiferromagnet $KCuF_3$ above T_N," *J. Phys. Soc. Japan*, vol. 38, pp. 1279–1285, 1975.

[7] X. Zotos, F. Naef, and P. Prelovsek, "Transport and conservation laws," *Phys. Rev. B*, vol. 55, no. 17, p. 6, 1996.

[8] X. Zotos, "Finite temperature Drude weight of the one-dimensional spin-1/2 Heisenberg model," *Phys. Rev. Lett.*, vol. 82, pp. 1764–1767, 1999.

[9] K. Kudo, Y. Koike, S. Kurogi, T. Noji, T. Nishizaki, and N. Kobayashi, "Magnon thermal conductivity in the spin-gap state and the antiferromagnetically ordered state of low-dimensional copper oxides," *J. Magn. Magn. Mater.*, vol. 272–276, pp. 94–95, May 2004.

[10] A. V. Sologubenko, K. Giannó, H. R. Ott, U. Ammerahl, and A. Revcolevschi, "Thermal conductivity of the hole-doped spin ladder system $Sr_{14-x}Ca_x Cu_{24}O_{41}$," *Phys. Rev. Lett.*, vol. 84, no. 12, pp. 1–4, 2000.

[11] C. Hess, C. Baumann, U. Ammerahl, B. Büchner, F. Heidrich-Meisner, W. Brenig, and A. Revcolevschi, "Magnon heat transport in $(Sr,Ca,La)_{14}Cu_{24}O_{41}$," *Phys. Rev. B*, vol. 64, no. 18, p. 184305, Oct. 2001.

[12] A. V. Sologubenko, T. Lorenz, H. R. Ott, and A. Freimuth, "Thermal conductivity via magnetic excitations in spin-chain materials," *J. Low Temp. Phys.*, vol. 147, no. 3–4, pp. 387–403, Feb. 2007.

[13] A. V. Sologubenko, H. R. Ott, G. Dhalenne, and A. Revcolevschi, “Universal behavior of spin-mediated energy transport in S=1/2 chain cuprates: $BaCu_2Si_2O_7$ as an example,” *Europhys. Lett.*, no. 1, p. 7, Feb. 2003.

[14] J. Stöhr and H. Siegmann, *Magnetism: from fundamentals to nanoscale dynamics*. Springer, 2007.

[15] D. J. Griffith, *Introduction to quantum mechanics*, 2nd ed. Pearson Education, 2007.

[16] R. I. Nepomechie, “A spin chain primer,” *arXiv:hep-th/9810032v1*, p. 15, Oct. 1998.

[17] A. A. Zvyagin, *Quantum theory of one-dimensional spin systems*. Cambridge Scientific Publishers Ltd, 2010.

[18] H. A. Kramers, “The interaction between the magnetic atoms in a paramagnetic crystal,” *Physica*, vol. 1, p. 182, 1934.

[19] P. W. Anderson, “Antiferromagnetism. Theory of superexchange interaction,” *Phys. Rev.*, vol. 79, no. 1934, p. 350, 1950.

[20] J. B. Goodenough, *Magnetism and the chemical bond*. Interscience,New yoyk, 1963.

[21] C. K. Majumdar, “On next-nearest-neighbor interaction in linear chain. I,” *J. Math. Phys.*, vol. 10, no. 8, p. 1388, 1969.

[22] R. Skomski, *Simple models of magnetism*. Oxford University Press, 2008.

[23] T. Giamarchi, *Quantum physics in one dimension*, no. January 2015. Oxford University Press, 2003.

[24] I. Bose, “Quantum magnets: a brief overview,” *arXiv:cond-mat/0107399v1*, p. 30, Jul. 2001.

[25] U. Schollwöck, J. Richter, D. J. J. Farnell, and R. Bishop, “Quantum magnetism,” *Lect. Notes Phys.*, vol. 645, pp. 4–493, 2004.

[26] A. Nakua, H. Yun, J. N. Reimers, J. E. Greedan, and C. V. Stagers, “Crystal structure, short range and long range magnetic ordering in $CuSb_2O_6$,” *J. Solid State Chem.*, vol. 112, pp. 105–112, 1991.

[27] M. Kato, A. Hatazaki, K. Yoshimura, and K. Kosuge, “One-dimensional magnetic behavior of $CuSb_2O_6$,” *Phys. B*, vol. 282, pp. 663–664, 2000.

[28] A. V. Prokofiev, F. Ritter, W. Assmus, B. J. Gibson, and R. K. Kremer, "Crystal growth and characterization of the magnetic properties of $CuSb_2O_6$," *J. Cryst. Growth*, vol. 247, pp. 457–466, 2003.

[29] E. Lieb and D. Mattis, "Ordering energy levels of interacting spin systems," *J. Math. Phys.*, vol. 3, no. 1962, pp. 749–751, 1962.

[30] J. des Cloizeaux and J. Pearson, "Spin-wave spectrum of the antiferromagnetic linear chain," *Phys. Rev.*, vol. 128, no. 5, 1962.

[31] F. Haldane, "Spinon gas"description of the S= 1/2 Heisenberg chain with inverse-square exchange: Exact spectrum and thermodynamics," *Phys. Rev. Lett.*, vol. 66, no. 11, pp. 1529–1532, Mar. 1991.

[32] F. Haldane, "Fractional statistics"in arbitrary dimensions: A generalization of the Pauli principle," *Phys. Rev. Lett.*, vol. 67, no. 8, pp. 937–940, Aug. 1991.

[33] K. P. Schmidt and G. S. Uhrig, "Excitations in one-dimensional S=1/2 quantum antiferromagnets," *Phys. Rev. Lett.*, vol. 90, no. 22, p. 227204, Jun. 2003.

[34] J. Renard, L. Regnault, and M. Verdaguer, "Haldane quantum spin chains," in *Magnetism: molecules to materials I: models and experiments*, vol. 3, 2002, pp. 49–93.

[35] F. Haldane, "Nonlinear field theory of large-spin Heisenberg antiferromagnets: Semiclassically quantized solitons of the one-dimensional easy-axis Néel state," *Phys. Rev. Lett.*, vol. 50, no. 15, pp. 1153–1156, Apr. 1983.

[36] L. A. Takhtajan, "The picture of low-lying excitations in the isotropic Heisenberg chain of arbitrary spins," *Physics Letters A*, vol. 87. pp. 479–482, 1982.

[37] H. M. Babujian, "Exact solution of the one-dimensional isotropic Heisenberg chain with arbitrary spins S," *Physics Letters A*, vol. 90. pp. 479–482, 1982.

[38] M. N. Barber and M. T. Batchelor, "Spectrum of the biquadratic spin-1 antiferromagnetic chain," *Phys. Rev. B*, vol. 40, pp. 4621–4626, 1989.

[39] I. Affleck, T. Kennedy, E. Lieb, and H. Tasaki, "Rigorous results on valence-bond ground states in antiferromagnets," *Phys. Rev. Lett.*, vol. 59, no. 7, pp. 799–802, Aug. 1987.

[40] B. Sutherland, "Model for a multicomponent quantum system," *Phys. Rev. B*, vol. 12, pp. 3795–3805, 1975.

[41] J. W. Bray, L. V. Interrante, I. S. Jacobs, and J. C. Bonner, *Extended linear chain compounds*, Plenum, New York, 1983.

[42] S. Blundell, *Magnetism in condensed matter*, Oxford University Press, 2001.

[43] M. Hase, I. Terasaki, and K. Uchinokura, "Observation of the spin-Peierls transition in linear Cu^{2+} (spin-1/2) chains in an inorganic compound $CuGeO_3$," *Phys. Rev. Lett.*, vol. 70, no. 23. pp. 3651–3654, 1993.

[44] J. L. Musfeldt, "Spin-Peierls materials," in *Magnetism: molecules to materials I: models and experiments*, 2002, pp. 95–130.

[45] G. Castilla, S. Chakravarty, and V. Emery, "Quantum magnetism of $CuGeO_3$," *Phys. Rev. Lett.*, vol. 75, no. 9, pp. 1823–1826, 1995.

[46] R. Chitra, S. Pati, H. R. Krishnamurthy, D. Sen, and S. Ramasesha, "Density-matrix renormalization-group studies of the spin-1/2 Heisenberg system with dimerization and frustration," *Phys. Rev. B*, vol. 52, no. 9, pp. 6581–6587, 1995.

[47] B. S. Shastry and B. Sutherland, "Excitation spectrum of a dimerized next-neighbor antiferromagnetic chain," *Phys. Rev. Lett.*, vol. 47, no. 1, pp. 964–967, 1981.

[48] D. G. Shelton, A. A. Nersesyan, and A. M. Tsvelik, "Antiferromagnetic spin ladders: Crossover between spin S=1/2 and S=1 chains," *Phys. Rev. B*, vol. 53, no. 13, pp. 8521–8532, 1996.

[49] E. Dagotto and T. M. Rice, "Surprises on the way from 1D to 2D quantum magnets: The novel ladder materials," *arXiv:cond-mat/9509181v1*, p. 18, 1995.

[50] P. W. Anderson, "The resonating valence bond state in La_2CuO_4 and superconductivity," *Science*, vol. 235, pp. 1196–1198, 1987.

[51] E. Dagotto, "Experiments on ladders reveal a complex interplay between a spin-gapped normal state and superconductivity," *Rep. Prog. Phys.*, vol. 62, pp. 1525–1571, 1999.

[52] C. Kittel, *Introduction to solid state physics*, 8th ed. Wiley, 2004.

[53] N. W. Ashcroft and N. D. Mermin, *Solid state physics*, 1st ed. Cengage Learning, 1976.

[54] J. Ziman, *Electrons and phonons - the theory of transport phenomena in solids*, Oxford University Press, 1960.

[55] R. Berman, *Thermal conduction in solids*, Clarendon Press, Oxford, 1976.

[56] T. M. Tritt, Ed., *Thermal conductivity:theory, properties and application*, Kluwer Academic, 2004.

[57] P. G. Klemens., "Thermal conductivity and lattice vibrational modes," in *Solid State Physics*, F. Seitz and D. Turnbul, Eds. Academic, NewYork, 1958.

[58] T. M. Tritt, "Thermoelectric phenomena, materials, and applications," *Annu. Rev. Mater. Res.*, vol. 41, no. 1, pp. 433–448, Aug. 2011.

[59] G. P. Srivastava, *The physics of phonons*, IOP Publishing Ltd, 1990.

[60] P. Carruthers, "Theory of thermal conductivity of solids at low temperatures," *Rev. Mod. Phys.*, vol. 33, no. 1, pp. 92–138, 1961.

[61] Neelmani and G. S. Verma, "Phonon conductivity of trivalent rare-earth-doped gallium and aluminium garnets," *Phys. Rev. B*, vol. 6, pp. 3509–3515, 1972.

[62] B. H. Armstrong, "Two-fluid theory of thermal conductivity of dielectric crystals," *Phys. Rev. B*, vol. 23, no. 2. pp. 883–899, 1981.

[63] P. G. Klemens, "Thermal resistance due to point defects at high temperatures," *Phys. Rev.*, vol. 119, no. 2, pp. 507–509, 1960.

[64] J. Callaway, "Model for lattice thermal conductivity at low temperatures," *Phys. Rev.*, vol. 113, no. 4, pp. 1046–1051, 1959.

[65] R. Berman and I. C. F. Brock, "The effect of isotopes on lattice heat conduction.I: Lithium fluoride," *Proc. R. Soc.*, vol. A289, pp. 46–65, 1965.

[66] R. Peierls, "Kinetic theory of thermal conduction in dielectric crystals," *Ann. Phys.*, vol. Leipzig 3, p. 1055, 1929.

[67] R. O. Pohl, "Thermal conductivity and phonon resonance scattering," *Phys. Rev. Lett.*, vol. 8, no. 12, pp. 481–483, 1962.

[68] H. M. Rosenberg and B. Sujak, "On the scattering of phonons by spins at low temperatures experimental," *Philos. Mag.*, vol. 5, no. 60, p. 1299, 1960.

[69] K. Neupane, "Ph.D. Thesis," University of Miami, 2009.

[70] B. D. Cullity, *Elements of x-ray diffraction*, 3rd ed. Addison- Wesley, Reading, MA, 2001.

[71] O. V. Lounasmaa, *Experimental principles and methods below 1 K*, Academic Press, 1974.

[72] J. Ekin, *Experimental techniques for low-temperature measurements*. Oxford University Press, 2006.

[73] E. T. Swartz, “Charcoal-pumped ^{3}He cryostats for storage Dewars,” *Rev. Sci. Instrum.*, vol. 58, no. 5, p. 881, 1987.

[74] C. F. Mate, R. Harris-Lowe, W. L. Davis, and J. G. Daunt, “^{3}He cryostat with adsorption pumping,” *Rev. Sci. Instrum.*, vol. 36, no. 1965, pp. 369–373, 1965.

[75] X. Zotos and P. Prelov´sek, *Strong interactions in low dimensions*. Kluwer, Dordrecht, 2004.

[76] N. Prasai, A. Rebello, A. B. Christian, J. J. Neumeier, and J. L. Cohn, “Phonon–spin scattering and magnetic heat transport in the quasi-one-dimensional spin−1/2 antiferromagnetic chain compound $CuSb_2O_6$,” *Phys. Rev. B*, vol. 91, no. 054403, pp. 1–6, 2015.

[77] “Private communication with J. J. Neumeier.” .

[78] E. Giere, A. Brahimi, H. J. Deiseroth, and D. Reinen, “The geometry and electronic structure of the Cu2+polyhedra in trirutile-type compounds $Zn(Mg)_{1-x}Cu_xSb_2O_6$ and the dimorphism of $CuSb_2O_6$: A solid state and EPR study,” *J. Solid State Chem.*, vol. 131, pp. 263–274, 1997.

[79] A. Rebello, M. G. Smith, J. J. Neumeier, B. D. White, and Y.-K. Yu, “Transition from one-dimensional antiferromagnetism to three-dimensional antiferromagnetic order in single-crystalline $CuSb_2O_6$,” *Phys. Rev. B*, vol. 87, no. 22, p. 224427, Jun. 2013.

[80] S. Matsushima, T. Tanizaki, H. Nakamura, M. Nonaka, and M. Arai, “First-principles energy band calculation for $ZnSb_2O_6$ with trirutile-type structure.,” *Chemistry Letters*. pp. 1010–1011, 2001.

[81] A. M. Nakua and J. E. Greedan, “Single crystal growth of transition metal antimonates AB_2O_6 from V_2O_5-B_2O_3,” *J. Cryst. Growth*, vol. 154, pp. 334–338, 1995.

[82] M. Yamaguchi, T. Furuta, and M. Ishikawa, “Calorimetric study of several cuprates with restricted dimensionality,” *J. Phys. Soc. Japan*, vol. 65, no. 9, pp. 2998–3006, Sep. 1996.

[83] M. Kato, T. Ishii, K. Kajimoto, and K. Yoshimura, “Magnetic properties of $CuSb_{2-x}Ta_x O_6$ with tri-rutile structure,” *J. Phys. Chem. Solids*, vol. 63, pp. 1129–1132, 2002.

[84] M. Heinrich, H. A. Krug von Nidda, A. Krimmel, A. Loidl, R. M. Eremina, A. D. Ineev, B. I. Kochelaev, A. V. Prokofiev, and W. Assmus, “Structural and magnetic properties of $CuSb_2O_6$ probed by ESR,” *Phys. Rev. B*, vol. 67, no. 22, p. 224418, Jun. 2003.

[85] B. J. Gibson, R. K. Kremer, A. V. Prokofiev, W. Assmus, and B. Ouladdiaf, "Elastic neutron diffraction study of long-range antiferro-magnetic order in the quantum chain system $CuSb_2O_6$," *J. Magn. Magn. Mater.*, vol. 272–276, pp. 927–928, May 2004.

[86] D. Kasinathan, K. Koepernik, and H. Rosner, "Quasi-one-dimensional magnetism driven by unusual orbital ordering in $CuSb_2O_6$," *Phys. Rev. Lett.*, vol. 100, no. 23, p. 237202, Jun. 2008.

[87] M. Kato, K. Kajimoto, K. Yoshimura, K. Kosuge, M. Nishi, and K. Kakurai, "Magnetic structure of $CuSb_2O_6$," *Journal of the Physical Society of Japan*, vol. 71, no. Suppl. pp. 187–189, 2002.

[88] E. Wheeler, "Ph.D. thesis," Somerville College,University of Oxford, 2007.

[89] A. B. Christian, S. H. Masunaga, A. T. Schye, A. Rebello, J. J. Neumeier, and Y.-K. Yu, "Magnetic field influence on the Néel, dimer, and spin-liquid states of the low-dimensional antiferromagnets $NiTa_2O_6$ and $CoSb_2O_6$," *Phys. Rev. B*, vol. 90, no. 22, pp. 1–10, 2014.

[90] E. Boulat, P. Mehta, N. Andrei, E. Shimshoni, and a. Rosch, "Heat transport properties of clean spin ladders coupled to phonons: Umklapp scattering and drag," *Phys. Rev. B - Condens. Matter Mater. Phys.*, vol. 76, pp. 1–7, 2007.

[91] M. Hofmann, T. Lorenz, G. Uhrig, H. Kierspel, O. Zabara, A. Freimuth, H. Kageyama, and Y. Ueda, "Strong damping of phononic heat current by magnetic excitations in $SrCu_2(BO_3)_2$," *Phys. Rev. Lett.*, vol. 87, no. 4, p. 047202, Jul. 2001.

[92] H. Winkelmann, E. Gamper, B. Büchner, M. Braden, A. Revcolevschi, and G. Dhalenne, "Giant anomalies of the thermal expansion at the spin-Peierls transition in $CuGeO_3$," *Phys. Rev. B*, vol. 51, pp. 12884–12887, 1995.

[93] K. Berggold, J. Baier, D. Meier, J. Mydosh, T. Lorenz, J. Hemberger, A. Balbashov, N. Aliouane, and D. Argyriou, "Anomalous thermal expansion and strong damping of the thermal conductivity of $NdMnO_3$ and $TbMnO_3$ due to 4f crystal-field excitations," *Phys. Rev. B*, vol. 76, no. 9, p. 094418, Sep. 2007.

[94] J. Traylor, H. Smith, R. Nicklow, and M. Wilkinson, "Lattice dynamics of rutile," *Phys. Rev. B*, vol. 3, no. 10, pp. 3457–3472, May 1971.

[95] F. W. Sheard and G. A. Toombs, "Resonant phonon scattering in a coupled spin-phonon system," *Solid State Communications*, vol. 12. pp. 713–716, 1973.

[96] M. N. Wybourne and B. J. Kiff, "Acoustic-optical phonon scattering observed in the thermal conductivity of polydiacetylene single crystals," *J. Phys. C Solid State Phys.*, vol. 18, pp. 309–318, 2000.

[97] N. Hlubek, P. Ribeiro, R. Saint-Martin, A. Revcolevschi, G. Roth, G. Behr, B. Büchner, and C. Hess, "Ballistic heat transport of quantum spin excitations as seen in $SrCuO_2$," *Phys. Rev. B*, vol. 81, pp. 1–4, 2010.

[98] A. Mohan, N. S. Beesetty, N. Hlubek, R. Saint-Martin, A. Revcolevschi, B. Büchner, and C. Hess, "Bond disorder and spinon heat transport in the S=1/2 Heisenberg spin chain compound Sr_2CuO_3: From clean to dirty limits," *Phys. Rev. B*, vol. 89, no. 10, p. 104302, Mar. 2014.

[99] "Private communication with S. H. Masunaga."

[100] B. Koteswararao, S. Salunke, a. Mahajan, I. Dasgupta, and J. Bobroff, "Spin-gap behavior in the two-leg spin-ladder $BiCu_2PO_6$," *Phys. Rev. B*, vol. 76, no. 5, p. 052402, Aug. 2007.

[101] O. Mentré, E. Janod, P. Rabu, M. Hennion, F. Leclercq-Hugeux, J. Kang, C. Lee, M.-H. Whangbo, and S. Petit, "Incommensurate spin correlation driven by frustration in $BiCu_2PO_6$," *Phys. Rev. B*, vol. 80, no. 18, p. 180413, Nov. 2009.

[102] A. A. Tsirlin, I. Rousochatzakis, D. Kasinathan, O. Janson, R. Nath, F. Weickert, C. Geibel, A. M. Läuchli, and H. Rosner, "Bridging frustrated-spin-chain and spin-ladder physics: Quasi-one-dimensional magnetism of $BiCu_2PO_6$," *Phys. Rev. B*, vol. 82, no. 14, p. 144426, Oct. 2010.

[103] K. W. Plumb, Z. Yamani, M. Matsuda, G. J. Shu, B. Koteswararao, F. C. Chou, and Y.-J. Kim, "Incommensurate dynamic correlations in the quasi-two-dimensional spin liquid $BiCu_2PO_6$," *Phys. Rev. B*, vol. 88, no. 2, p. 024402, Jul. 2013.

[104] Byung-Gu Jeon, B. Koteswararao, C. B. Park, K. H. Kim, G. J. Shu, F. C. Chou, S. C. Riggs, and S. B. Chung, "Evolution of magnetic excitations in $BiCu_2PO_6$ observed via magnetic suppression of phono heat conduction," in *Bulletin of the American Physical Society APS March Meeting*, 2015.

[105] K. Y. Choi, J. W. Hwang, P. Lemmens, D. Wulferding, G. J. Shu, and F. C. Chou, "Evidence for dimer crystal melting in the frustrated spin-ladder system $BiCu_2PO_6$," *Phys. Rev. Lett.*, vol. 110, no. 11, p. 117204, Mar. 2013.

[106] B. Koteswararao, S. Salunke, A. Mahajan, I. Dasgupta, and J. Bobroff, "Spin-gap behavior in the two-leg spin-ladder $BiCu_2PO_6$," *Phys. Rev. B*, vol. 76, no. 5, p. 052402, Aug. 2007.

[107] E. Orignac, R. Chitra, and R. Citro, "Thermal transport in one-dimensional spin gap systems," *Phys. Rev. B*, vol. 67, no. 134426, p. 13, 2002.

[108] C. Hess, P. Ribeiro, B. Büchner, H. Elhaes, G. Roth, U. Ammerahl, and A. Revcolevschi, “Magnon heat conductivity and mean free paths in two-leg spin ladders: A model-independent determination,” *Phys. Rev. B*, vol. 73, pp. 1–5, 2006.